Title

Numerical Study of the Effects of Nucleation Cavity Spacing, Substrate Thermal Properties and Substrate Thickness on Bubble Dynamics and Heat Transfer During Nucleate Pool Boiling Under Constant Imposed Heat Flux

ISBN

9798265453952

Author

Krishnan, Atindra

Publication Date

2025-12-03

Peer reviewed|Thesis/dissertation

UNIVERSITY OF CALIFORNIA

Los Angeles

Numerical Study of the Effects of Nucleation Cavity Spacing, Substrate Thermal Properties and Substrate Thickness on Bubble Dynamics and Heat Transfer During Nucleate Pool Boiling Under Constant Imposed Heat Flux

A dissertation submitted in partial satisfaction of the
requirements for the degree Doctor of Philosophy
in Mechanical Engineering

by

Atindra Krishnan

2025

`

`

ABSTRACT OF THE DISSERTATION

Numerical Study of the Effects of Nucleation Cavity Spacing, Substrate Thermal Properties and Substrate Thickness on Bubble Dynamics and Heat Transfer During Nucleate Pool Boiling Under Constant Imposed Heat Flux

by

Atindra Krishnan
Doctor of Philosophy in Mechanical Engineering
University of California, Los Angeles, 2025
Professor Vijay K. Dhir, Chair

Three-dimensional numerical simulations are performed for nucleate pool boiling of saturated water at atmospheric pressure, on a 7 mm × 7 mm portion of a horizontal solid substrate with two adjacent active cavity sites, during boiling inception. A constant heat flux of 1.1 W/cm^2 is imposed at the bottom face of the substrate. A static contact angle of 35° and a cavity nucleation superheat of 6°C are considered. Level-set method is used to track the liquid-vapor interface, and finite-difference schemes are used to discretize the governing equations.

Two parametric simulation studies are done. In the first study, the influence of cavity spacing and lateral bubble merger on bubble dynamics and heat transfer during pool boiling on a 1 mm thick horizontal stainless-steel substrate having two adjacent active cavity sites with parametrically varied cavity spacing ranging from 1 mm to 3 mm, is investigated. The results show that cavity spacing, and lateral bubble merger have a strong influence on the waiting time and bubble departure frequency. The influence on the bubble departure diameter and growth period is

relatively less pronounced. The average heat transfer coefficient, based on the wall superheat averaged over the boiling surface area in the computational domain and over one bubble cycle, is found to increase with increase in cavity spacing. The average heat transfer coefficient for two non-merging bubbles with cavity spacing 3 mm is 15 % higher than that for two laterally merging bubbles with a spacing of 1 mm.

In the second parametric study, the effects of substrate material thermal properties and substrate thickness on bubble dynamics and heat transfer during pool boiling on copper, stainless-steel and glass substrates, each with thicknesses ranging from 0.25 mm to 2.5 mm, are analyzed. Two different cavity spacings, 1.4 mm and 3 mm, which represent cases with and without lateral bubble merger respectively, are considered for each substrate. The study results clearly indicate that substrate thermal properties have a stronger influence on bubble dynamics and heat transfer than that of substrate thickness. As the substrate thermal diffusivity increases, the waiting time and the bubble departure diameter decrease while the bubble departure frequency increases. The bubble growth period decreases with increasing substrate thermal diffusivity when lateral bubble merger occurs, but the trend is reversed in cases with no bubble merger. The average heat transfer coefficient increases with increasing substrate thermal diffusivity, going up by about 50 % from glass to copper, and it increases by less than 8 % as the substrate thickness increases from 0.25 mm to 2.5 mm for the materials considered.

The dissertation of Atindra Krishnan is approved.

Adrienne G. Lavine

Kunihiko Taira

Timothy S. Fisher

Vijay K. Dhir, Committee Chair

University of California, Los Angeles

2025

Contents

List of Figures

Chapter 4

List of Tables

Nomenclature

A	area of the boiling surface or Hamaker constant
c	specific heat capacity
D_d	equivalent bubble departure diameter
f	bubble departure frequency
g	acceleration due to gravity
h	heat transfer coefficient or grid spacing
Ja	Jakob number
k	thermal conductivity
L	substrate thickness
$q_{w,in}$	imposed heat flux
S	cavity spacing
t	time
t_{cycle}	bubble cycle duration
T	temperature
$\dot{V}_{micro}$	evaporation rate in microlayer

Greek Symbols

ϕ	level-set function
φ	contact angle

ρ	density
σ	surface tension
ν	kinematic viscosity
α	thermal diffusivity
δ_t	thermal boundary layer thickness

Subscripts

f	fluid
g	growth
nuc	nucleation
s	solid
w	waiting or wall

Acknowledgements

I extend my sincere gratitude to Professor Vijay Dhir for his valuable guidance and relentless support throughout my graduate program at UCLA. His remarkable patience and encouraging mentorship have been instrumental in the successful completion of this research work.

I am very grateful to my labmates for their help and support during my time in the lab.

I am indebted to my parents and my sister for their constant encouragement and for remaining at my side through thick and thin.

Vita

University of California, Los Angeles, United States

M.S. in Mechanical Engineering, 2018

Amrita Vishwa Vidyapeetham, Coimbatore, India

B. Tech. in Mechanical Engineering, 2016

Publications

Krishnan, A., & Dhir, V. K. “Numerical Study of the Effect of Substrate Thermal Properties and Thickness on Bubble Dynamics and Heat Transfer During Nucleate Pool Boiling under Constant Imposed Heat Flux on a Horizontal Substrate with Two Adjacent Nucleation Sites Active”. (In preparation)

Krishnan, A., & Dhir, V. K. “Numerical study of influence of lateral bubble merger on bubble dynamics and heat transfer during nucleate pool boiling on a horizontal substrate under a constant imposed heat flux”. International Journal of Heat and Mass Transfer, 247. 2025

Chapter 1

Introduction

Nucleate pool boiling is recognized as one of the most effective mechanisms of heat transfer, enabling rapid removal of thermal energy from heated surfaces immersed in a stationary liquid. The high efficiency of this process is predominantly due to the latent heat of vaporization associated with liquid-to-vapor phase change, and the liquid motion caused by the growing and departing vapor bubbles. The superior heat transfer capability of nucleate boiling is harnessed in numerous engineering applications including power generation systems, nuclear reactors, thermal management of spacecraft, and electronics cooling. Despite its widespread utilization, the complex interactions between the various subprocesses involved during nucleate pool boiling makes it challenging to fully understand the underlying physics governing the process.

Numerous empirical and semi-empirical correlations have been proposed in the literature to predict aspects of bubble dynamics and nucleate boiling heat transfer. While these models offer valuable insights, they are invariably tailored to the specific conditions under which experimental data were obtained and hence cannot be reliably used for prediction of bubble dynamics and heat transfer for any general condition. For a fully mechanistic model capable of reliably forecasting boiling performance, a thorough understanding of the individual and combined effects of the governing subprocesses is indispensable.

In the subsequent sections of this chapter, a discussion of the relevant background is first provided, including key aspects of nucleate pool boiling such as bubble nucleation, bubble departure diameter, growth period and waiting time. This is followed by a brief review of existing literature on important subprocesses such as interaction of bubbles at adjacent cavity sites and the thermal response of the solid substrate. The chapter ends with a discussion of the objectives of the present study.

1.1 Regimes in Pool Boiling

A typical boiling curve for pool boiling of saturated water at atmospheric pressure is shown in Fig. 1.1. The x-axis is the wall superheat, which is defined as the wall temperature minus the saturation temperature corresponding to the system pressure, and the y-axis is the wall heat flux. At very low values of heat flux (or wall superheat), represented by Region I in the figure, heat transfer from the wall to the liquid is entirely by natural convection, whereby a circulating liquid flow is created near the wall by virtue of density gradients in the liquid which in turn are caused by temperature gradients in the thermal boundary layer close to the wall. As the wall heat flux is increased, the wall superheat also increases gradually, and the heat transfer continues to occur by natural convection. This continues till the heat flux reaches the value corresponding to point A in the figure, where the wall superheat is high enough to initiate bubble nucleation at certain cavity sites on the boiling surface. This point A is commonly referred to as the onset of nucleate boiling (ONB) or as boiling inception. This marks the beginning of the nucleate boiling regime (Region II).

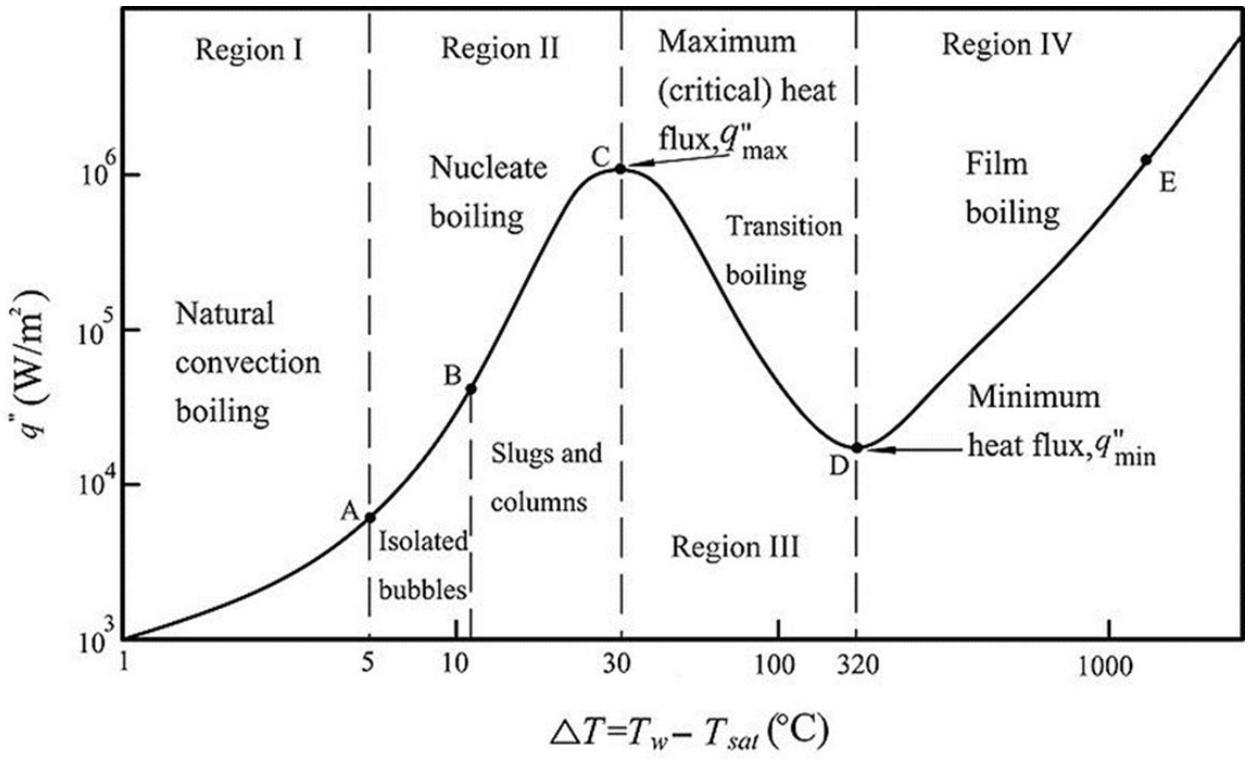

Fig. 1.1: A typical boiling curve for saturated pool boiling of water at atmospheric pressure.

The nucleate boiling regime itself can be further partitioned into the partial nucleate boiling regime and the fully developed nucleate boiling regime. In the partial nucleate boiling regime, the region between points A and B in the figure, bubbles predominantly grow and depart from discrete cavity sites on the boiling surface without merging. Lateral merger of bubbles in this regime, though less common, can still occur if there are cavity sites that are close enough to each other such that the spacing between the sites is comparable to or smaller than the diameter of an isolated bubble under the same conditions. As the wall heat flux is further increased in the partial nucleate boiling regime, an increasingly larger number of cavity sites on the boiling surface become active, and the

frequency of bubble departure from a given cavity site also increases. This results in a significantly greater occurrence of lateral merger of bubbles from adjacent cavity sites, in addition to vertical merger of bubbles departing from a given cavity site. This corresponds to the fully developed nucleate boiling regime, between points B and C in the figure, characterized by the presence of mushroom shaped bubbles and vapor columns attached to the wall, resulting from lateral and vertical merger of bubbles respectively.

Point C in the figure represents the critical heat flux, which is the maximum heat flux at which nucleate boiling can be sustained on the boiling surface. If the wall heat flux is increased beyond this point, the process transitions to the film boiling regime (Region IV) where a vapor film separates the entire boiling surface from the liquid, and the wall superheat rapidly increases to a value corresponding to the point E in the figure. This is because the heat transfer coefficient in the film boiling regime is lower than that in the nucleate boiling regime resulting from the low thermal conductivity vapor covering the entire boiling surface. If the heat flux is further increased, film boiling continues and the wall superheat increases at a faster rate than in the nucleate boiling regime. In film boiling, vapor bubbles grow and depart periodically from the liquid-vapor interface.

In most practical applications, the heat flux to the heated substrate is controlled. For cases where the wall temperature is controlled, as the wall superheat is increased gradually from its value at the critical heat flux (point C), the heat flux decreases, and the boiling process goes into the transition boiling regime (Region III). The transition boiling regime is a highly unstable regime where a given location of the boiling surface will be in intermittent contact with liquid and vapor. The heat flux continues to decrease with increasing wall superheat in this regime, until point D is reached. This point corresponds to the minimum heat flux at which film boiling can be sustained.

Beyond this point, the heat flux again starts to increase with increasing wall superheat, albeit at a slower rate than in the nucleate boiling regime.

Of all the regimes of pool boiling, the nucleate boiling regime is of the highest practical significance due to its ability to dissipate higher heat fluxes at a relatively lower wall superheat. As such, nucleate pool boiling has been a subject of extensive research for several decades in an effort to obtain a clear understanding of the various subprocesses, and to develop mechanistic models that have universal predictive capabilities of nucleate boiling heat transfer.

1.2 Criteria for Bubble Nucleation

Heterogeneous bubble nucleation is the process in which bubbles form at microscopic imperfections such as cavities, scratches and grooves on the solid surface rather than in the bulk of the liquid. It is how bubbles form during nucleate pool boiling. Not all imperfections or cavities on the boiling surface can support bubble nucleation. The formation of bubbles requires the presence of gas-trapping cavities on the boiling surface. The trapped gas acts as a nucleus that supports evaporation of the surrounding superheated liquid, and the resulting bubble embryo continues to grow due to liquid-to-vapor phase change at the bubble interface. It is thus essential to understand the different parameters that affect the capability of a cavity site to trap gas.

Several mechanistic models have been reported in the literature related to gas entrapment in cavities, and other conditions required to initiate bubble nucleation at a cavity site, some of which are discussed in this section. For a cavity site to be able to trap some gas, the liquid front advancing towards the cavity site should not flood the site. The size and shape of a cavity site, along with the solid surface wettability for a given solid-liquid combination are important factors in determining

the capability of the cavity site to trap gas when the solid surface is immersed in the liquid. Wang and Dhir [1] proposed the following criterion for gas entrapment in an arbitrarily shaped cavity site in a uniform temperature field

$$\varphi > \psi_{min} \tag{1.1}$$

where φ is the contact angle, and ψ_{min} is the minimum cavity side angle defined as the mouth angle for spherical and conical cavities. The minimum cavity side angle for sinusoidal cavities lies inside the cavity site. The above criterion is based on an analysis of Helmholtz free energy.

Another important parameter is the minimum wall superheat required to sustain bubble growth at the site. Even if a cavity site is found to be capable of trapping gas, an embryo cannot grow into a bubble unless the surrounding liquid has sufficient superheat to sustain the evaporation at the liquid-vapor interface. The earliest criterion for minimum wall superheat for boiling inception, and the range of cavities that can support bubble nucleation for a given wall superheat was proposed by Hsu [2]. He postulated that for a bubble embryo to grow, it must be surrounded entirely by liquid that is at least at the saturation temperature corresponding to the pressure inside the vapor bubble. Hsu [2] considered a truncated spherical bubble sitting on the cavity mouth opening. The bubble height (y_b) and the bubble radius (R_b) are related to the cavity mouth opening radius (R_c) as

$$y_b = C_1 R_c \tag{1.2}$$

$$R_b = C_2 R_c \tag{1.3}$$

where the terms C_1 and C_2 are functions of the contact angle, and are defined as

$$C_1 = (1 + cos\varphi)/sin\varphi \tag{1.4}$$

$$C_2 = 1/sin\varphi \tag{1.5}$$

Hsu's criterion can be mathematically expressed as

$$T_l|_{y=y_b} \geq T_b \tag{1.6}$$

where T_b is the saturation temperature corresponding to the pressure inside the bubble. The saturation temperature inside the bubble is approximated using the Clausius-Clapeyron equation as

$$T_b = T_{sat} + \frac{2\sigma T_{sat}}{R_b \rho_v h_{fg}} \tag{1.7}$$

where the term $2\sigma/R_b$ is the pressure difference between the vapor bubble and the surrounding liquid due to surface tension. The liquid temperature T_l can be assumed to vary linearly in the thermal boundary layer close to the wall, and the corresponding variation can be expressed as

$$T_l = T_\infty + (T_w - T_\infty)\left(1 - \frac{y}{\delta_t}\right) \tag{1.8}$$

where T_∞ is the temperature of the bulk liquid, and δ_t is the thermal boundary layer thickness

For a given wall temperature, the range of cavity sizes that can support bubble growth according to the Hsu's criterion, can be determined by combining Eq. (1.6) with Eqs. (1.7) and (1.8), which yields

$$R_{c,min}, R_{c,max} = \frac{\delta_t (T_w - T_{sat})}{2C_1 (T_w - T_l)} \left[1 \mp \sqrt{1 - \left(\frac{8C_1}{C_2}\right)\frac{(T_w - T_l)T_{sat}\sigma}{(T_w - T_{sat})^2 \delta_t \rho_v h_{fg}}}\right. \tag{1.9}$$

A graphical depiction of the above criterion is shown in Figure 1.2, for a contact angle of 90°.

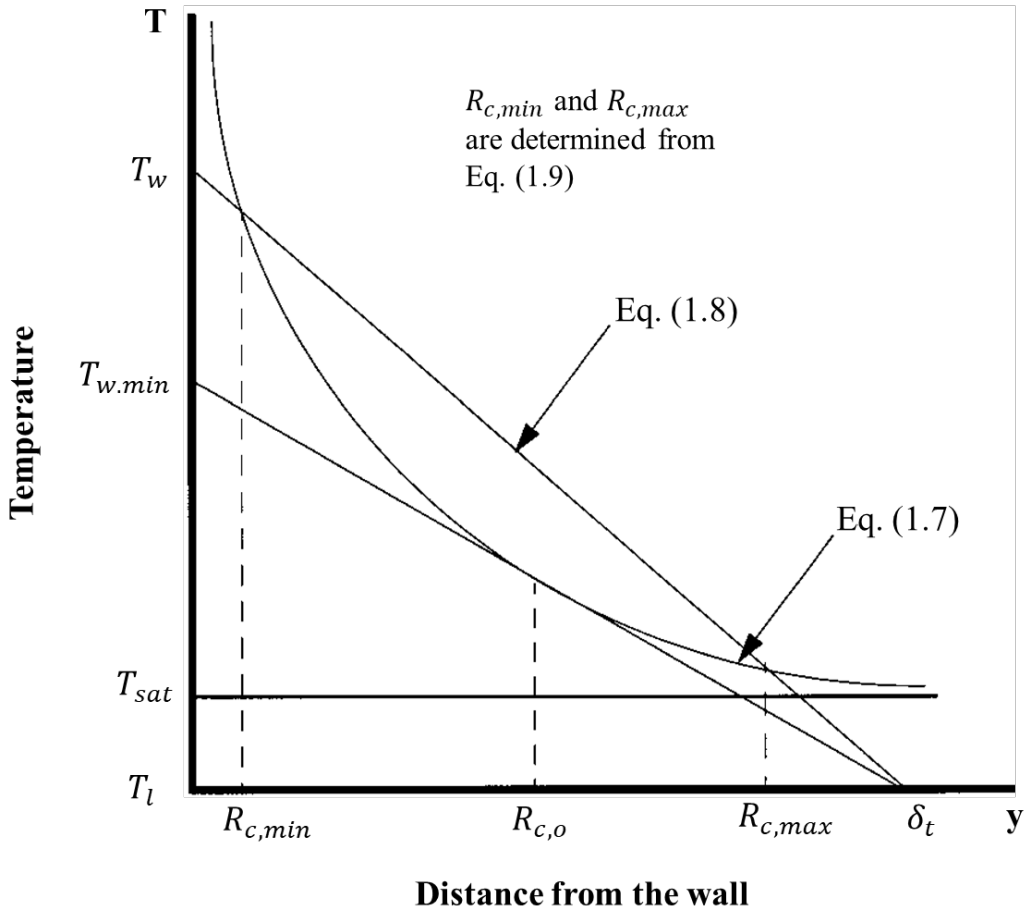

Fig. 1.2: Range of nucleating cavities according to Hsu's criterion. (φ = 90°).

Wang and Dhir [1] proposed the following relation for the minimum wall superheat necessary for bubble nucleation in a spherical cavity of diameter D_c by studying the stability of the liquid-vapor interface of preexisting vapor nuclei

$$\Delta T_w = \frac{4\sigma T_{sat}}{\rho_v h_{fg} D_c} K_{max} \tag{1.10}$$

where K_{max} is the maximum value of a nondimensional modified curvature defined by the authors, and its value depends on the contact angle as

$$K_{max} = 1 \text{ if } \varphi \leq 90°$$
$$K_{max} = sin\varphi \text{ if } \varphi > 90° \tag{1.11}$$

Basu et al. [3] conducted experiments for subcooled flow boiling of water on a flat plate copper surface and a nine-rod zircalloy bundle. They determined the minimum wall superheat corresponding to onset of nucleate boiling (ONB) on the surface through visual observations and temperature measurements. They proposed that for a general boiling surface, the probability that an unflooded cavity of the size corresponding to the minimum wall superheat according to Hsu's criterion exists on the surface decreases as the surface wettability increases. They proposed the following equation for the minimum wall superheat for onset of nucleate boiling on the surface

$$\Delta T_w = \frac{4\sigma T_{sat}}{\rho_v h_{fg} D_{c,o} F} \tag{1.12}$$

where $D_{c,o}$ is the cavity diameter corresponding to the minimum wall superheat for boiling inception, determined from the tangency condition of Hsu's criterion (Fig. 1.2), and the factor F accounts for the probability of finding the cavity of size $D_{c,o}$. The expressions for $D_{c,o}$ and F are as follows:

$$D_{c,o} = \left[\frac{8\sigma T_{sat} k_l}{\rho_v h_{fg} q_w}\right]^{\frac{1}{2}} \tag{1.13}$$

$$F = 1 - exp\left[-\left(\frac{\pi\varphi}{180}\right)^3 - 0.5\left(\frac{\pi\varphi}{180}\right)\right] \tag{1.14}$$

It can be seen in Eq. (1.14) that for a very small contact angle (~ 0), the factor F becomes very small. This in turn will result in a much higher inception wall superheat, according to Eq. (1.12).

1.3 Bubble Growth Rate and Departure Diameter

Several mechanistic models have been proposed in the literature to describe the growth of bubbles attached to the wall during nucleate pool boiling. Mikic et al. [4] developed an analytical model capable of predicting the growth rate for a vapor bubble while attached to the wall with liquid of non-uniform temperature surrounding the bubble. They assumed that all the evaporation occurs through the liquid-vapor interface which is surrounded by superheated liquid. Their model does not account for the existence of a microlayer, which is a thin layer (few microns in thickness) of liquid between the heated surface and the bubble. The presence of a microlayer, and the evaporation of liquid in the microlayer were initially proposed by Moore and Mesler [5] and Cooper and Lloyd [6], based on their observations of rapid fluctuations in the local wall temperature close to the bubble base during high heat flux pool boiling and pool boiling with isolated vapor bubbles respectively. Similar observations were reported in more recent experimental studies [7-10], further confirming the existence of a microlayer. Cooper [11] developed an analytical model to predict the growth rate of a vapor bubble attached to a heated wall, including the effect of microlayer evaporation. Their analysis assumed conditions in which individual bubbles grow in isolation in an otherwise stagnant liquid layer to sizes significantly larger than the thermal boundary layer thickness. For these conditions, they assumed that the microlayer heat transfer predominates. The formation of the microlayer and its thickness in their analysis were considered in accordance with the hydrodynamic theory proposed by Cooper and Lloyd [6].

Various correlations have been proposed for bubble growth rate as a function of the Jakob number, which represents a non-dimensional wall superheat. One such empirical correlation proposed by

Cole and Shulman [12] for predicting the evolution of bubble diameter with time for bubbles growing on a heated wall at high Jakob numbers

$$D = 5\,Ja^{\frac{3}{4}}\sqrt{\pi\alpha_l t} \tag{1.15}$$

where the Jakob number (Ja) is defined as

$$Ja = \frac{\rho_l c_l (T_w - T_{sat})}{\rho_v h_{fg}} \tag{1.16}$$

The above correlation given by Cole and Shulman [12] was developed based on experimental data in the range of Jakob numbers from 24 to 792. In general, the bubble growth rate for a given fluid increases with increase in wall superheat.

A bubble growing on a heated surface is subjected to various forces. The bubble departure is determined by variation in the relative magnitudes of these forces, some of which tend to detach the bubble from the boiling surface while the other forces tend to keep the bubble attached to the boiling surface. Surface tension, drag force and inertia are some of the primary forces resisting bubble detachment, while buoyancy is a key force that assists bubble detachment from the boiling surface. Fritz [13] proposed the following correlation for the bubble departure diameter, based on a static force balance on a bubble attached to the wall considering only the buoyancy and surface tension forces

$$D_d = 0.0208\varphi\sqrt{\frac{\sigma}{g(\rho_l - \rho_v)}} \tag{1.17}$$

where φ is the contact angle in degrees. Other correlations have been proposed for the prediction of bubble departure diameter, taking into account the wall superheat. Cole [14] proposed the following modified form of the Fritz [13] correlation, including the Jakob number

$$D_d = 0.04\, Ja \sqrt{\frac{\sigma}{g(\rho_l - \rho_v)}} \tag{1.18}$$

From Eq. (1.18), it is seen that as the wall superheat increases, the bubble departure diameter increases, and this is attributed to an increase in bubble growth rate with increase in the Jakob number (or wall superheat). Some of the existing correlations involve the thermal diffusivity of the liquid, in addition to the Jakob number. Van Stralen and Zijl [15] proposed the correlation shown below

$$D_d = 2.63 \left(\frac{Ja^2 \alpha_l^2}{g}\right)^{\frac{1}{3}} \left[1 + \left(\frac{2\pi}{3Ja}\right)^{0.5}\right]^{\frac{1}{4}} \tag{1.19}$$

Kocamustafaogullari [16] considered the effect of system pressure on the bubble departure diameter by introducing the density ratio of liquid and vapor in the correlation, as shown below for water

$$D_d = 2.64 \times 10^{-5} \left[\frac{\sigma}{g(\rho_l - \rho_v)}\right]^{\frac{1}{2}} \left(1 - \frac{\rho_v}{\rho_l}\right)^{0.9} \tag{1.20}$$

Though several correlations exist for the bubble departure diameter, they are semi-empirical in nature, and there is still a lack of a universal correlation that can reliably predict the bubble departure diameter for nucleate pool boiling in any general condition. This is because of the complex dependence of the bubble departure diameter on various parameters such as the surface wettability, thermo-physical properties of the fluid, system pressure and bubble growth rate. Other important factors such as the thermal response of the solid substrate, and the presence of lateral and vertical merger of bubbles also influence the bubble departure diameter.

1.4 Bubble Growth Period

The bubble growth period is the time interval between bubble nucleation at a cavity site to the time the bubble departs from the boiling surface. Semi-empirical correlations have been reported in the literature to predict the bubble growth rate, most of which express the bubble growth period in terms of the bubble departure diameter and the wall superheat — which in turn influences the bubble growth rate. Zuber [17] proposed the following correlation to predict the bubble growth period, expressed in terms of the bubble departure diameter, Jakob number and thermal diffusivity of the liquid

$$t_g = \frac{D_d^2}{16b^2(Ja)^2\alpha_l} \tag{1.21}$$

where b is a constant, whose magnitude typically ranges from 1 to $\sqrt{3}$.

Accurate prediction of the bubble growth period is challenging due to its complex dependence on parameters such as the bubble departure diameter and bubble growth rate, which in turn depend on the various factors including evaporation at the liquid-vapor interface, microlayer evaporation, the temperature field in the liquid and solid.

1.5 Waiting Time

The waiting time is another important bubble dynamics parameter during nucleate pool boiling. It is defined as the time elapsed between the departure of a bubble growing at a cavity site to the nucleation of the next bubble at the same site.

Han and Griffith [18] solved the transient thickness of the thermal boundary layer by considering transient conduction from the heated surface into a semi-infinite liquid that is initially entirely at the bulk liquid temperature. They obtained an expression for the waiting time by combining the transient evolution of thermal layer thickness with the criterion for bubble initiation that the mean temperature of the liquid surrounding the bubble must be equal to or above the saturation temperature corresponding to the pressure inside the bubble. The resulting equation for the waiting time is shown below

$$t_w = \frac{9}{4\pi\alpha_l}\left[\frac{(T_w - T_\infty)R_c}{T_w - T_{sat}\left(1 + \frac{2\sigma}{R_c\rho_v h_{fg}}\right)}\right]^2 \tag{1.22}$$

where R_c is the radius of the cavity mouth opening and T_∞ is the bulk liquid temperature far away from the surface. According to this equation, the waiting time depends on the thermophysical properties of liquid and vapor, the wall temperature, the bulk liquid temperature and the cavity size.

The above model for waiting time is based on transient conduction into the liquid while assuming a constant wall temperature (T_w). This assumption is not reasonable for most practical applications, where the power to the solid substrate is controlled. As described earlier in Section 1.3, rapid fluctuations in the boiling surface temperature have been observed in several experiments in the past. These temperature variations in the solid substrate influence the bubble dynamics and heat transfer on the fluid side. Comprehensive models for the waiting time should include the effect of the thermal response of the solid substrate during nucleate boiling. In such models, the transient temperature variation in the solid substrate post bubble departure can be used in conjunction with a suitable bubble nucleation criterion, such as the one specified in Eq. (1.10), to predict the

occurrence of a new bubble nucleation event at a cavity site, and in turn determine the waiting time.

1.6 Bubble Departure Frequency

The bubble departure frequency during nucleate boiling is defined as the inverse of the sum of the growth and waiting periods, as shown below

$$f = \frac{1}{t_g + t_w} \tag{1.23}$$

The bubble departure frequency is a key parameter in determining the boiling heat transfer coefficient. Several correlations for predicting the bubble departure diameter have been proposed in literature, most of which consider the bubble departure frequency in combination with the bubble departure diameter. Jakob [19] proposed the following correlation for bubble departure frequency in terms of the bubble departure diameter and fluid properties

$$fD_d = \left[\frac{\sigma g(\rho_l - \rho_v)}{\rho_l^2}\right]^{\frac{1}{4}} \tag{1.24}$$

Zuber [20] proposed a modified version of the above correlation, by modeling the heat transfer during partial nucleate boiling as an equivalent single phase turbulent natural convection process, incorporating the void fraction in the mean density of the fluid. The correlation is shown below

$$fD_d = \left(\frac{1.18}{2}\right)\left[\frac{\sigma g(\rho_l - \rho_v)}{\rho_l^2}\right]^{\frac{1}{4}} \tag{1.25}$$

Peebles [21] proposed the following correlation for predicting the bubble departure diameter, which requires information about the growth and waiting periods

$$fD_d = 1.18\left[\frac{t_g}{t_g + t_w}\right]\left[\frac{\sigma g(\rho_l - \rho_v)}{\rho_l^2}\right]^{\frac{1}{4}} \tag{1.26}$$

The correlations discussed above, and most correlations that have been proposed for bubble departure frequency do not account for the cooling of the substrate during nucleate boiling and assume a constant wall temperature. As discussed in Section 1.5, it is essential to consider conjugate heat transfer in the solid substrate for a more realistic modeling of bubble growth, bubble departure and the waiting period during nucleate boiling process. As such, coupling the transient conduction in the substrate with the fluid-side heat transfer is an important aspect of the present work.

1.7 Active Nucleation Site Density

The number density of active nucleation sites (N_a) on a conventional boiling surface increases with increase in wall superheat. The active nucleation site density, together with the bubble departure frequency and bubble departure diameter, is important in determining the average heat transfer coefficient for a boiling surface. Several authors have proposed correlations for the determination of the active nucleation site density for nucleate boiling spanning a wide range of experimental conditions.

Gaertner and Westwater [22] conducted pool boiling experiments of aqueous solution of nickel salts on a horizontal flat copper surface and estimated the number of active nucleation sites by counting the number of holes in the nickel layer that was deposited on the heated surface during

the boiling process. They found that the active nucleation site density varies with the wall heat flux as

$$N_a \sim q_w^{2.1} \tag{1.27}$$

Wang and Dhir [1] performed saturated pool boiling of water at atmospheric pressure on vertical copper surfaces with different degrees of oxidation to obtain different contact angles. They proposed the following correlation for the active nucleation site density as a function of the contact angle

$$N_a = 5.0 \times 10^5 (1 - cos\varphi) D_c^{-6.0} \tag{1.28}$$

where D_c is the cavity size after multiplying a correction factor to the measured cavity size to account for irregular shape of the cavities.

Basu et al. [3] performed subcooled flow boiling experiments for water on a vertical flat copper plate and a nine-rod zircalloy bundle. They observed that the experimentally determined active nucleation density was in good agreement with the correlation of Wang and Dhir [1] at wall superheat above 15 °C but not for lower wall superheats. Basu et al. [3] proposed the following set of correlations for the active nucleation site density for two ranges of wall superheats

$$\begin{aligned} N_a &= 3.4 \times 10^{-1} (1 - cos\varphi) \Delta T_w^{2.0} \quad \text{if } \Delta T_{w,ONB} < \Delta T_w < 15° \\ N_a &= 3.4 \times 10^{-5} (1 - cos\varphi) \Delta T_w^{5.3} \quad \text{if } \Delta T_w \geq 15° \end{aligned} \tag{1.29}$$

The correlations for predicting active nucleation site density proposed in the literature are semi-empirical in nature and are unable to predict experimental data accurately for conditions that differ from those under which the correlations were obtained. A fully mechanistic prediction of active nucleation site density is challenging since it requires information about several parameters such as the sizes of cavities on the surface, wall superheat, wall heat flux and surface wettability. Even

if information about the size distribution of cavity sites on the boiling surface is known, the number of cavity sites that are active cannot be accurately determined without considering the thermal interaction between neighboring cavity sites.

1.8 Cavity-Cavity Interaction and Lateral Bubble Merger

Thermal interaction between neighboring cavity sites, and lateral merger of bubbles from adjacent active sites influence the dynamics of bubble nucleation, growth and departure during the nucleate boiling process. Thermal interaction between cavity sites occurs through the substrate when the bubble growth at one cavity site causes cooling of the substrate over an area that is large enough to affect the growth of bubbles at adjacent cavity sites.

Zhang and Shoji [23] performed experiments to study the effect of cavity spacing on bubble departure frequency during pool boiling of saturated water on 0.2 mm thick polished silicon plates of diameter 15 mm having two cylindrical cavities fabricated on the top face, with inter-cavity spacings ranging from 1 mm to 8 mm. The heat flux imposed on the heating surface in their experiments was in the range of 2.2 W/cm^2 to 3.7 W/cm^2. They found that the bubble departure frequency varies non-linearly with the non-dimensional cavity spacing $S/\overline{D_b}$, where $\overline{D_b}$ is the mean departure diameter of bubbles without merger. They considered three mechanisms of interactions between the two adjacent active cavity sites, namely the thermal interaction between the cavities due to conduction in the substrate, hydrodynamic interaction between the bubbles through the liquid motion induced by the growth and departure of bubbles, and coalescence (merger) of bubbles from the two cavity sites. They explained that the thermal interaction between the cavity sites tends to decrease the bubble departure frequency, while the hydrodynamic and bubble merger

interactions tend to increase the bubble departure frequency. They proposed that the dependence of the bubble departure frequency with the non-dimensional cavity spacing is governed by the variation in the relative magnitudes of three interaction mechanisms and identified four regions of nucleation site interaction, as shown in Fig. 1.3. The bubble departure frequencies shown in this figure are the average values over all the heat fluxes considered in their study.

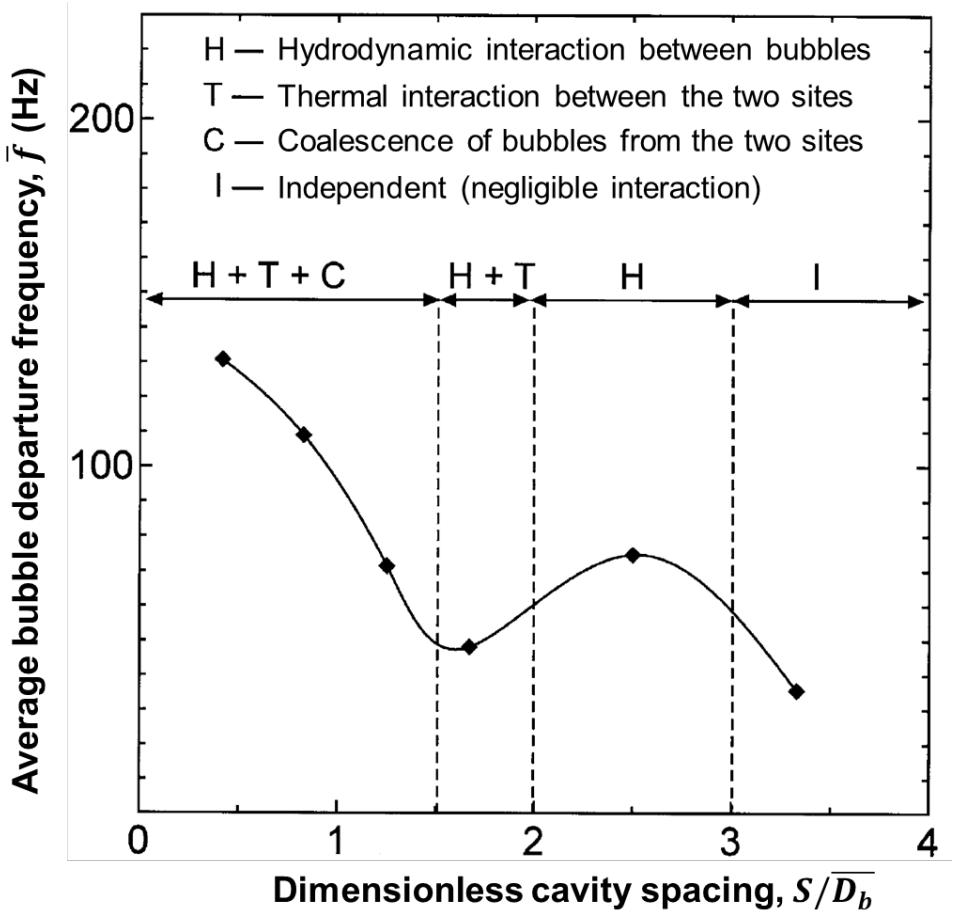

Fig. 1.3: Regions of nucleation site interactions (Zhang and Shoji [23]).

For $S/\overline{D_b}$ > 3 (the 'I' region), there is negligible interaction between the two cavity sites, and the bubble departure frequency is similar to that for a single isolated cavity site. In the range 2 < $S/\overline{D_b}$ ≤ 3 (the 'H' region), there is negligible thermal interaction and horizontal bubble merger, and the hydrodynamic interaction between the bubbles leads to a higher bubble departure frequency than in the 'I' region. In the range 1.5 < $S/\overline{D_b}$ ≤ 2 (the 'H' + 'T' region), the thermal interaction between the cavity sites and the hydrodynamic interaction between the bubbles compete and the result is a decrease in bubble departure frequency from the 'H' region. For $S/\overline{D_b}$ ≤ 1.5 (the 'H' + 'T' + 'C' region), the three interaction mechanisms co-exist and compete. The net result is a promotive effect due to which the bubble departure frequency increases again.

Chatpun et al. [24] performed a similar study to that of Zhang and Shoji [23] but for 0.2 mm thick silicon surfaces with three artificial cylindrical cavity sites fabricated in in-line and equilateral triangle patterns, and with cavity spacings in the range 1 mm to 4 mm. The surface was heated using an Nd-YAG laser in a range of heat flux from 3.4 to 5.6 W/cm^2. They observed a similar non-linear dependence of bubble departure frequency on the cavity spacing. They found that for a given cavity spacing, the bubble departure frequency for the inline pattern is higher than that for the triangular pattern, and the bubble departure frequency for three artificial cavity sites is higher than that for two artificial cavity sites with the same spacing reported by Zhang and Shoji [23].

Jiang et al. [25] performed an experimental study to investigate the effect of cavity spacing on the bubble dynamics during saturated pool boiling of water on the surfaces of 6 mm thick, 25 mm diameter copper and stainless-steel cylinders, with two artificial cavity sites fabricated on the surface. Cavity spacings ranging from 1 mm to 6 mm were studied, and the heating power was in the range of about 3 W/cm^2 to 7 W/cm^2. They observed that the intensity of thermal interactions

between the two cavity sites, and its impact on the bubble departure frequency and average vapor removal rate, depends not only on the cavity spacing but also on the thermal conductivity of the substrate. Using a numerical analysis of the thermal conduction in the wall, supplemented by the heat flux obtained from the experiments, they observed a significantly greater degree of fluctuations in the radial wall temperature distribution in the stainless-steel substrate as compared to that in the copper substrate, indicating that there is a stronger thermal interaction between the cavity sites through the substrate for the lower thermal conductivity stainless-steel. A discussion of studies related to the role of thermal properties of the heated substrate during nucleate boiling is provided in the next subsection.

When the spacing between adjacent active cavity sites is equal to or less than the departure diameter for a bubble growing at an isolated cavity site under the same conditions, the bubbles from the adjacent cavity sites merge laterally during the growth period, before departing from the boiling surface. Several research efforts have been made to understand the effect of lateral bubble merger on important aspects of nucleate boiling such as bubble growth period, bubble departure diameter and bubble departure frequency.

Mukherjee and Dhir [26] performed numerical simulations and experiments to study the lateral merger of vapor bubbles formed during saturated nucleate pool boiling of water on a horizontal surface under constant wall superheat. They considered three cases of lateral bubble merger, namely two cavities, three cavities inline, and three cavities at the corners of an equilateral triangle, with a cavity spacing of 1.25 mm in all the cases. They assumed a constant wall superheat of 10°C in their simulations, with additional simulations performed for two-bubble merger at 5°C and three-bubble merger at 6°C to facilitate comparison with their experimental data. For their experiments, they used 10 cm diameter silicon wafer on which cavities 10 μm in diameter and

20 μm deep were microfabricated in the same three configurations considered in their simulations. They measured the static contact angle of 54° and used the same value in their numerical model. In their simulations, they modeled the microlayer following the formulation implemented by Son et al. [27], which is based on application of lubrication theory by Lay and Dhir [28] to model the liquid flow in an evaporating microlayer. From their numerical simulations, Mukherjee and Dhir [26] found that the equivalent bubble departure diameter based on the total vapor volume of the merged bubble at departure and the bubble growth period for the three-bubble merger cases are clearly smaller than the corresponding values for two merging bubbles. For the cavity spacing and contact angle that they considered, the bubble departure diameter and growth period for the two-bubble merger case were observed to be only slightly smaller than those for a single isolated bubble. The bubble shapes and bubble dynamics predicted from their simulations showed a good agreement with their experimental observations.

Aparajith et al. [29] numerically investigated the dynamics of lateral merger of three adjacent bubbles during nucleate pool boiling of PF5060 on a horizontal flat surface under reduced gravity conditions, for a constant wall superheat. They also considered the same model for the microlayer as that used by Mukherjee and Dhir [26]. They considered three different orientations — three cavities inline, three cavities arranged in a right-angled triangle and three cavities arranged in an equilateral triangle. A constant wall superheat of 10°C was considered for all the cases. Reduced gravity levels of $10^{-2}g_e$ and $10^{-5}g_e$ were studied. For each cavity orientation and gravity level, cavity spacing was varied from $0.25D_s$ to $1D_s$, where D_s is the bubble departure diameter of a single bubble at the corresponding gravity level, for a wall superheat of 10°C. At both gravity levels, the bubble departure diameter, bubble growth period and the average wall Nusselt number all decrease as the cavity spacing decreases from $1D_s$ to $0.25D_s$. For a given non-dimensional

spacing (S/D_s), the bubble departure diameter, bubble growth period, and average wall Nusselt number all show a decrease with change in the cavity arrangement from the equilateral triangle to the right triangle and then to the inline cavity configuration, at both gravity levels. The average wall Nusselt number is calculated as $Nu_w = \bar{q}_w l_o/(k_l \Delta T_w)$, where l_o is the characteristic length scale for boiling at the given gravity level and $\bar{q}_w$is the wall heat flux averaged over the heater surface area included in the computational domain and over the bubble growth period.

Mukherjee and Dhir [26] and Aparajith et al. [29] assumed constant wall superheat conditions in their numerical simulations. The waiting time for these simulations is specified as an input, either arbitrarily or based on experimental data. As such, simulations that assume a constant wall temperature cannot be used to predict the waiting time during nucleate boiling under new conditions. The simulation results of Mukherjee and Dhir [26] agree with their experimental data despite assuming constant wall temperature in the simulations. This may be attributed to the high thermal diffusivity of the silicon substrate, for which a constant wall temperature assumption may not be very unrealistic. Generally, to be able to accurately predict the waiting time and in turn the bubble departure frequency, the transient conduction in the substrate needs to be coupled with the fluid-side heat transfer. Some of the numerical investigations of nucleate pool boiling that include the conjugate heat transfer in the substrate are discussed in the next subsection.

1.9 Thermal Response of the Solid Substrate

The thermal response of the solid substrate is an important factor in determining the bubble dynamics on the fluid side, and the associated heat transfer during nucleate pool boiling. The local cooling of the substrate in the regions close to the active cavity sites during the bubble growth and

departure has an influence on the bubble growth rate, bubble departure diameter, bubble growth period, waiting time and bubble departure frequency. These parameters have a strong influence on the average heat transfer coefficient during nucleate pool boiling. The thermal response of the solid substrate, which is essentially determined by the transient conduction in the substrate, depends on the thermal properties and thickness of the substrate. Some existing experimental and numerical investigations on the role of substrate thermal properties and thickness during nucleate pool boiling are presented below.

Magrini and Nannei [30] performed experiments for saturated pool boiling of water on horizontal, cylindrical walls that were obtained by plating copper, silver, zinc, nickel and tin on non-metallic rods. For each wall material, different wall thicknesses, ranging from 5 to 250 μm were tested. The average wall heat flux over the wall surface in the experiments were in the range of 50 to 800 kW/m^2. They found that the smaller the thermal conductivity of the wall material, the more pronounced is the effect of wall thickness on the boiling heat transfer coefficient. They observed that for the nickel, tin and zinc surfaces, the heat transfer coefficient was observed to increase with decreasing wall thickness, with up to 600 % increase for nickel and tin. Even in the cases of nickel, tin and zinc heating walls, beyond a certain wall thickness, defined by the authors as the "limiting value", the heat transfer coefficient did not show any further changes with increasing thickness. This limiting value is about 70 μm for zinc, and about 15 μm for nickel and tin. In the range of thicknesses beyond the limiting value, the heat transfer coefficient was found to decrease with decreasing thermal effusivity ($\sqrt{\rho c k}$) of the wall materials.

Jabardo et al. [31] experimentally studied the pool boiling of R-134a and R-123 on horizontal cylindrical surfaces made of brass, copper and stainless steel, at different values of reduced pressures. The range of heat fluxes tested was from about 1.5 kW/m^2 at the lower end to about

120 kW/m^2 for copper samples, 80 kW/m^2 for brass samples, and 60 kW/m^2 for stainless-steel samples. For each surface material, samples of average surface roughness ranging from 0.07 μm to 3.00 μm were tested. For a given average surface roughness and reduced pressure, they observed that the heat transfer coefficient for the brass samples was slightly better than that for copper sample, while the heat transfer coefficient for stainless steel was clearly lower than those for the other two materials, especially at higher wall heat fluxes. For a given surface material, very rough surfaces were found to have higher heat transfer coefficients at low heat fluxes while the trend is reversed at the higher end of the heat flux range. Seo et al. [32] performed pool boiling experiments of deionized water at atmospheric pressure on horizontal cylindrical claddings made of silicon carbide and zircaloy. They found that the boiling heat transfer coefficient for the silicon carbide cladding was consistently higher than that for the zircaloy cladding, over the entire range of wall heat fluxes studied.

Hosseini et al. [33] experimentally investigated the pool boiling of R-113 on horizontal heated circular plates made of copper, brass and aluminum, with the heat flux provided to the plate ranging from 8 to 200 kW/m^2. They observed that the heat transfer coefficient for the copper plate was clearly the highest, while the heat transfer coefficient for brass was found to be slightly higher than that for aluminum. For example, the heat transfer coefficient for the copper plate was found to be about 23 % higher than that for aluminum plate and about 18 % higher than that for the brass plate, at a heat flux of 168 kW/m^2. Bombardieri et al. [34] experimentally obtained nucleate pool boiling curves for saturated liquid nitrogen at atmospheric pressure on horizontal plates made of copper, aluminum and stainless steel. For the entire range of heat fluxes studied, they observed that the heat transfer coefficient for copper was clearly higher than those for aluminum and stainless steel. The authors, however, could not make a clear distinction in the relative magnitudes of heat transfer

coefficients for aluminum and stainless steel since the observed differences were small compared to the experimental uncertainty in the estimation of heat flux for stainless-steel.

Voglar et al. [35] performed saturated pool boiling experiments for water at atmospheric pressure on a bare stainless-steel foil, a bare titanium foil, and a copper foil coated with a nanostructured layer of copper oxide. They found that the heat transfer coefficient was highest for the nanostructure coated copper foil. The heat transfer coefficient for the titanium foil was slightly smaller than that for copper. The heat transfer coefficient for the stainless-steel foil was clearly smaller than that for the other two materials, with the gap widening as the heat flux increases. At a heat flux of about 200 kW/m^2, they observed that the heat transfer coefficient for the nanostructure coated copper foil was about 7 % higher than that for the titanium foil and about 70 % higher than that for the stainless-steel foil. Godinez et al. [36] conducted saturated pool boiling experiments for distilled water on horizontal flat upwards facing aluminum, stainless-steel and copper heating surfaces. The thickness of the aluminum and copper substrates was 1.5 mm while the stainless-steel substrate was 0.2 mm thick. They found that in general the boiling heat transfer coefficient did not show an appreciable dependence on the substrate material. At high heat fluxes, the heat transfer coefficient was the highest for copper and the smallest for stainless-steel, while the differences were still small to be of physical significance. The authors noted that the contact angle showed significant variability among the three materials, ranging from 12° for aluminum to 65° for copper.

Kapitz et al. [37] performed experiments for saturated pool boiling of water on synthetic diamond and silicon carbide heating surfaces. The measured static, advancing and receding contact angles for the two surface materials were nearly identical (less than 10 % difference). They observed that the boiling curves for the two surface materials were very similar despite the thermal diffusivity

of the diamond being 8 times larger than that for silicon carbide. They in fact noted that the heat transfer coefficient for the silicon carbide heating surface was slightly higher than that for the diamond surface at higher heat fluxes. They attributed these observations to possibly different numbers of active nucleation sites on the two surfaces, especially at higher heat fluxes.

Mann et al. [38] numerically modeled the heat transfer to a single bubble during its growth on a heated substrate for saturated pool boiling of different fluids. They considered growth of a vapor bubble on copper, steel and ceramic substrates, and they included the heat conduction in the substrate. However, they assumed a quasi-stationary heat transfer whereby the transient terms in the energy balance equations were neglected. Such an assumption would neglect the thermal energy stored in the substrate, which may not be justifiable for materials with relatively low thermal diffusivity such as steel and ceramic. They imposed a constant temperature at the bottom face of the substrate, and its value for each substrate material was chosen such that the superheat on the boiling surface averaged over the wall area of computation and over the growth period, remains the same for all the materials. They assumed a wedge-shaped micro region, based on the model introduced by Stephan and Hammer [39]. They found that the heat transfer coefficient increases with increasing wall thermal conductivity. For R-114, they obtained a 25 % higher heat transfer coefficient for copper as compared to that for ceramic, at a wall superheat of 4.48 K.

Aktinol and Dhir [40] performed axisymmetric numerical simulations to study the transient thermal response of the solid substrate during single bubble saturated pool boiling of water on copper, steel and borosilicate glass substrates, each of different thicknesses, with a constant heat flux imposed at the base of the substrate. They modeled the shape of the microlayer and calculated the microlayer evaporation heat transfer using lubrication theory, as done in some earlier studies [26,27,29]. They included the conjugate transient conduction in the heated substrate, and their

numerical simulations were able to predict the waiting time based on a cavity nucleation superheat of 6°C used as the nucleation criterion. They found that the waiting time decreases with increase in the substrate thermal diffusivity and with increase in the substrate thickness. They noted that substrate thermal properties have a greater influence on bubble dynamics than the substrate thickness.

Zhang et al. [41] performed axisymmetric numerical simulations of single bubble pool boiling for water on nickel, stainless steel and fused silica surfaces, including the transient heat conduction in the substrate. They imposed a constant temperature at the bottom face of the substrate. They assumed a constant slope of $tan\varphi$ for the microlayer interface, where φ is the contact angle. Consistent with the findings of Aktinol and Dhir [40], they observed that the waiting time clearly decreases with increasing thermal diffusivity. For the fused silica substrate, they found that the waiting time increased significantly when the substrate thickness was increased from 0.5 mm to 1.5 mm. They attributed this to the increase in thermal conduction resistance of the solid substrate with increase in substrate thickness.

1.10 Motivation and Objectives of the Present Work

The discussions provided thus far in this chapter reveal some gaps in published studies on the interactions between adjacent cavity sites, and the influence of substrate thermal properties and thickness on bubble dynamics and heat transfer during nucleate pool boiling. The experimental studies that considered the interactions between two or more adjacent active cavity sites were carried out over a range of heat fluxes that were high enough that there was a negligible waiting

time compared to the growth period. As such, the effects of lateral bubble merger and thermal interactions between the adjacent cavity sites on the waiting time are not found in these studies. Additionally, existing numerical investigations of lateral merger of multiple bubbles were performed for constant wall superheat conditions. The bubble merger process in these studies is decoupled from the thermal response of the solid substrate. As such, some important thermal performance parameters such as the average vapor production rate and average heat transfer coefficient in these numerical investigations were obtained considering only the growth period.

In experimental studies published on the effect of substrate thermal properties on nucleate pool boiling heat transfer, there are almost always additional physical parameters — such as surface wettability, surface roughness, number density of nucleation sites — that also vary from one test sample to another. Inferences related to variations in bubble dynamics and heat transfer during nucleate pool boiling on substrates of different materials, drawn from such experimental studies, implicitly include the effect of the additional physical parameters mentioned above, rendering it challenging to pin the observed effects on the substrate thermal properties alone. Certain published numerical studies have succeeded in isolating the effects of substrate thermal properties and thickness by maintaining the same values of all other parameters across all the substrate materials and thicknesses. These numerical studies, however, mostly focus on single bubbles growing at an isolated cavity site.

The present work aims to provide insights into how the cavity spacing and lateral bubble merger influence the bubble dynamics — including the influence on waiting time — and heat transfer during nucleate pool boiling on a horizontal substrate under constant imposed heat flux conditions representing boiling inception.

The present work further aims to study the dependence of bubble dynamics and heat transfer on the substrate thermal properties and thickness, during nucleate pool boiling on a horizontal surface with two adjacent active cavity sites. The focus is also on determining whether this dependence is the same for cases with and without the occurrence of lateral bubble merger. Complete three-dimensional numerical simulations are performed to model the process of saturated nucleate pool boiling of water at atmospheric pressure on a portion of a flat horizontal substrate with two adjacent active nucleation sites, under constant imposed heat flux conditions representing boiling inception.

Thus, the objectives of the present work are as follows:

1. Perform a parametric study to quantify the dependence of waiting time, growth period, bubble departure diameter, bubble departure frequency, and heat transfer coefficient on the cavity spacing, for a fixed substrate material, substrate thickness, contact angle, imposed wall heat flux, and cavity nucleation temperature.
2. Parametrically quantify the dependence of waiting time, growth period, bubble departure diameter, bubble departure frequency, and heat transfer coefficient on the substrate thermal properties and substrate thickness, for two different cavity spacings representing cases with and without lateral bubble merger, using the same contact angle, imposed wall heat flux, and cavity nucleation temperature in all the cases.

Chapter 2

Numerical Model

A reliable numerical model for simulations of nucleate boiling should be capable of capturing the various subprocesses involved, in order to obtain an accurate and realistic representation of the boiling process. The model should be able to account for phase change at the liquid-vapor interface as well as evaporation from the microlayer. The bubbles must be able to grow without restrictions in shape, their detachment should be determined by the appropriate force balance, and they should be able to rise freely in the liquid. The liquid motion induced by the growth and departure of bubbles from the surface should be included in the simulations. Since the heat flux to the substrate is controlled in most practical applications of nucleate boiling, the temperature and heat flux on the boiling surface vary in both space and time. As such, the numerical model should be able to capture these variations in the boiling surface temperature and heat flux through the solution of the coupled transient conduction in the solid substrate. Through the prediction of the spatial and temporal distribution of the boiling surface temperature, the numerical simulations must be able to determine the occurrence of bubble nucleation, thereby facilitating the determination of the waiting time, which is the time elapsed between bubble departure from a cavity site to the subsequent bubble nucleation at that site.

The numerical model implemented in the present work uses a staggered-grid finite difference method, based on the model initially developed by Son et al. [27], wherein the evolution of the liquid-vapor interface is captured using a level-set function. The details of the numerical model,

including a discussion of the different regions in the computational domain, the governing equations and boundary conditions in these regions, the solution methodology, and an experimental validation of the model are presented in the subsequent sections of this chapter.

2.1 Computational Domain

In the present numerical model, the computational domain in the fluid-side is divided into two regions — micro region and macro region — as initially proposed by Son et al. [27]. These regions of the fluid-side domain are shown in Fig. 2.1. The micro region is a thin evaporating liquid film that forms between the boiling surface and the liquid-vapor interface of a bubble attached to it. The inner edge of the microlayer ($r = R_0$) has a thickness on the order of molecular size (~ 1 nm). Further radially inward of the inner edge of the microlayer is an ultra-thin adsorbed film of liquid molecules held to the boiling surface by strong intermolecular forces. This adsorbed liquid film does not evaporate and hence it is modeled as a dry region. The outer edge of the microlayer ($r = R_1$) has a thickness equal to half the grid size ($h/2$), which corresponds to the vertical distance from the boiling surface to the first computational node on the fluid side. The existence of a microlayer underneath a vapor bubble growing on a heated wall, and the corresponding wall temperature fluctuations due to microlayer evaporation have been reported in various experimental studies [5-10].

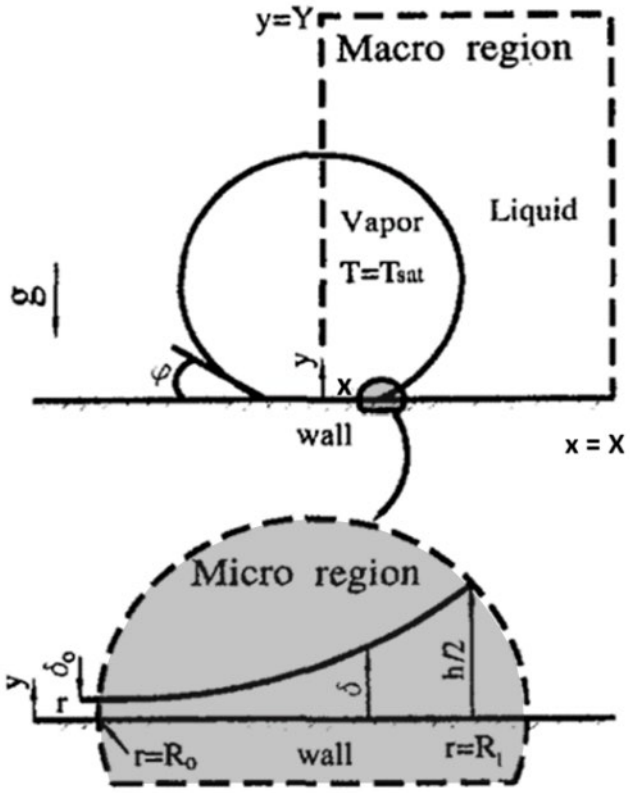

Fig. 2.1: Micro and macro regions in the fluid-side computational domain.

The macro region comprises the vapor bubble(s) and the bulk liquid. A sharp interface level-set method is used to capture the evolution of the liquid-vapor interface in the macro region. The solid substrate is treated as a separate region, in which the transient conduction equation is solved to obtain the spatial and temporal variation of the substrate temperature. The solid-side and fluid-side temperature and heat flux solutions are coupled iteratively at the boiling surface for each time step, as discussed in detail later in this chapter.

The region of interest in the present work is a 7 mm × 7 mm portion of a horizontal substrate of thickness L, having two adjacent active cavity sites with a spacing S. Figure 2.2 shows the front and top views of the region of interest. The cavity sites are assumed to be point cavities. Also, the two cavity sites are assumed to be identical, and bubble nucleation and growth at the two sites are assumed to be synchronous. Taking advantage of the resulting symmetry, computations are performed for one-quarter of the region of interest, as indicated by the shaded region in Fig. 2.2. The dimensions of the computational domain for which the simulations are performed are X = 3.5 mm, Y = 14 mm and Z = 3.5 mm. The cavity spacing S and substrate thickness L are varied across the different cases studied in the present work. However, the region of interest and in turn the computational domain are the same for all the cases simulated in the present work, unless specified otherwise.

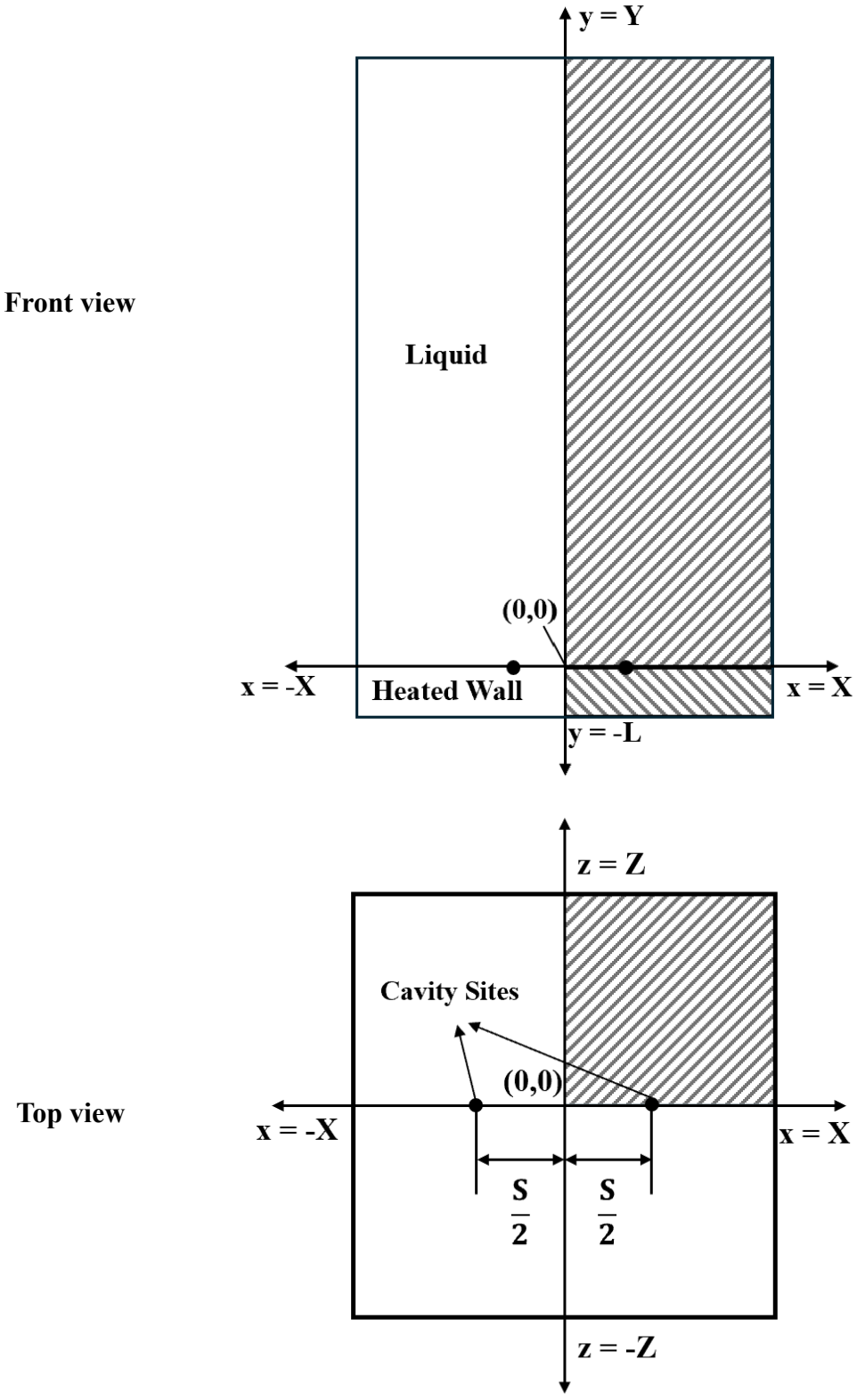

Fig. 2.2: Front and top views of the region of interest and the computational domain (shaded region). X = 3.5 mm, Y = 14 mm, Z = 3.5 mm.

2.2 Assumptions

The following assumptions are made in the development of the numerical model implemented in the present study:

- The fluid flow is assumed to be laminar
- The density, specific heat capacity, thermal conductivity and viscosity of the fluid are assumed to be constant in each phase.
- The vapor phase and the liquid-vapor interface in macro region are assumed to remain at saturation temperature corresponding to the pressure in the liquid.
- The variation of surface tension with interface temperature is considered only in the micro region.
- A static contact angle is used in the model. The dynamic variation of contact angle during bubble growth is not considered in the present study.
- The density, specific heat capacity and thermal conductivity of the solid substrate are assumed to be constant, for a given substrate material.
- It is assumed that there are no other active cavity sites in the region of interest (7 mm $\times$ 7 mm) on the boiling surface, except the two identical cavity sites with spacing S.

2.3 Micro Region

The radial variation of the liquid film thickness in the microlayer is obtained by solving the conservation equations in the micro region. Though the numerical simulations in the present study are three-dimensional, a two-dimensional quasi-static model is used for the micro region. It is assumed that there are no variations in the azimuthal direction. Lubrication theory, as used in earlier works by Wayner et al. [42] and Lay and Dhir [28], is used in the mathematical formulation of the micro region. The mass, momentum and energy conservation equations in the microlayer are as follows:

$$\frac{q}{\rho_l h_{fg}} = -\frac{1}{r}\frac{\partial}{\partial r}\int_0^{\delta} r u_l dy \tag{2.1}$$

$$\frac{\partial p_l}{\partial r} = \mu_l \frac{\partial^2 u_l}{\partial y^2} \tag{2.2}$$

$$q = \frac{k_l(T_w - T_{int})}{\delta} \tag{2.3}$$

where δ is the local thickness of the microlayer. Based on a modified Clausius-Clapeyron equation [42], the evaporative heat flux can be expressed as

$$q = h_{ev}\left[T_{int} - T_v + \frac{(p_l - p_v)T_v}{\rho_l h_{fg}}\right] \tag{2.4}$$

where $T_v = T_{sat}(p_v)$. The evaporative heat transfer coefficient, h_{ev} is obtained from kinetic theory as

$$h_{ev} = \frac{(2M/\pi\bar{R}T_v)^{0.5}\rho_v h_{fg}^2}{T_v} \tag{2.5}$$

The pressures in the liquid and vapor phases are related to each other using the relation given by Lay and Dhir [28] as

$$p_l = p_v - \sigma\kappa - \frac{A}{\delta^3} + \frac{q^2}{\rho_v h_{fg}^2} \tag{2.6}$$

where the surface tension σ is a function of the temperature of the liquid-vapor interface. The second, third and fourth terms on the right-hand side of Eq. (2.6) correspond to the capillary pressure, disjoining pressure, and recoil pressure due to phase change at the interface, respectively. The curvature of the liquid-vapor interface is calculated as

$$\kappa = \frac{1}{r}\frac{d}{dr}\left[r\frac{d\delta}{dr} \Big/ \sqrt{1 + \left(\frac{d\delta}{dr}\right)^2} \right] \tag{2.7}$$

Combining the mass, momentum, and energy conservation equations in the microlayer results in a fourth order differential equation as shown below

$$\delta'''' = f(\delta, \delta', \delta'', \delta''') \tag{2.8}$$

where $\delta' = d\delta/dr$. The boundary conditions at the inner radius of the microlayer ($r = R_0$) are

$$\delta = \delta_0, \ \delta' = \delta''' = 0 \tag{2.9}$$

where δ_0 is the equilibrium thickness of the microlayer (order of molecular size). At the outer radius of the microlayer ($r = R_1$), the following boundary conditions are imposed

$$\delta = h/2, \qquad \delta'' = 0 \tag{2.10}$$

where $h/2$ is the vertical distance from the wall to the first computational node in the fluid. The inner and outer radii of the microlayer are related to each other through the contact angle as

$$tan\,\phi = \frac{0.5\,h}{R_1 - R_0} \tag{2.11}$$

The procedure for matching the micro region and macro region solutions is outlined below:

1) Obtain the value of R_1 from the macro region solution.

2) Guess an initial value of the Hamaker constant (A)

3) Solve the fourth order partial differential equation, Eq. (2.8), with the boundary conditions, Eqs. (2.9) and (2.10), and obtain the value of R_0.

4) Calculate the apparent contact angle using Eq. (2.11).

5) Repeat steps 3 and 4 for different values of the Hamaker constant (A) until the apparent contact angle calculated in step 4 matches the specified static contact angle.

2.4 Macro Region

In the macro region, a level-set formulation similar to the model implemented by Son et al. [27], which includes the effect of phase change at the interface. The level-set function (ϕ) is defined as the signed distance from the liquid-vapor interface. The level-set function is negative in the vapor phase and positive in the liquid phase. The interface is captured by the set of points for which the level-set function equals zero. The continuity, momentum and energy equations for the liquid and vapor phases in the macro region are as follows:

$$\frac{\partial \rho}{\partial t} + \nabla.(\rho \vec{u}) = 0 \tag{2.12}$$

$$\rho\left(\frac{\partial \vec{u}}{\partial t} + \vec{u} \cdot \nabla \vec{u}\right) = -\nabla p + \rho \vec{g} - \rho\beta(T - T_{sat})\vec{g} - \sigma\kappa\nabla H + \nabla \cdot \mu\nabla\vec{u} + \nabla \cdot \mu\nabla\vec{u}^T \tag{2.13}$$

$$\rho c_p \left(\frac{\partial T}{\partial t} + \vec{u} \cdot \nabla T\right) = \nabla \cdot k \nabla T \quad \text{for} \quad H = 1 \tag{2.14}$$

$$T = T_{sat} \quad \text{for} \quad H = 0 \tag{2.15}$$

The fluid density, viscosity and thermal conductivity are defined as

$$\begin{aligned} \rho &= \rho_v + (\rho_l - \rho_v)H \\ \mu &= \mu_v + (\mu_l - \mu_v)H \\ k &= k_l H \end{aligned} \tag{2.16}$$

where the Heaviside function (H) in the sharp interface model of the present study is defined as a step-function as follows:

$$\begin{aligned} H &= 1 \quad \text{if } \phi > 0 \\ H &= 0 \quad \text{if } \phi \leq 0 \end{aligned} \tag{2.17}$$

The evaporative mass flux $\vec{m}$ at the liquid-vapor interface is expressed as

$$\vec{m} = \rho(\vec{u}_{int} - \vec{u}) = k \nabla T / h_{fg} \tag{2.18}$$

where $\vec{u}_{int}$ is the interface velocity. The continuity equation, Eq. (2.12), can be rewritten for grid cells adjacent to the liquid-vapor interface as

$$\begin{aligned} \nabla . \vec{u} &= -\frac{1}{\rho}\left(\frac{\partial \rho}{\partial t} + \vec{u} . \nabla \rho\right) + \dot{V}_{micro} \\ &= \frac{\vec{m}}{\rho^2} \nabla \rho + \dot{V}_{micro} \end{aligned} \tag{2.19}$$

The first term in Eq. (2.19) is the rate of volume change per unit volume, due to phase change at the liquid-vapor interface. The term $\dot{V}_{micro}$ is the rate of vapor production per unit volume due to microlayer evaporation, and it is obtained from the micro region solution as

$$\dot{V}_{micro} = \int_{R_0}^{R_1} \frac{(T_w - T_{int})k_l}{\rho_v h_{fg} \delta \Delta V_{micro}} r dr \tag{2.20}$$

where ΔV_{micro} is a vapor-side control volume near the micro region. For grid cells in the vicinity of the liquid-vapor interface but not close to the boiling surface, the $\dot{V}_{micro}$ term in Eq. (2.19) is zero.

The evolution of the liquid-vapor interface during the boiling process is captured by solving the level-set advection equation given below

$$\frac{\partial \phi}{\partial t} + \vec{u}_{int} \cdot \nabla \phi = 0 \tag{2.21}$$

The interface velocity ($\vec{u}_{int}$) is obtained from the mass balance at the interface (Eq. (2.18)). To ensure that the level-set function maintains its core property of a signed distance function (i.e., to ensure $|\nabla \phi| = 1$), the following level-set reinitialization equation is solved in pseudo time steps till steady state is obtained

$$\frac{\partial \phi}{\partial t} = \frac{\phi_0}{\sqrt{\phi_0^2 + h^2}} (1 - |\nabla \phi|) \tag{2.22}$$

where ϕ_0 is the solution of Eq. (2.21), and h is the grid spacing.

The boundary conditions for the equations in the macro region are as follows:

- At $x = 0$ and $x = X$

$$u = \frac{\partial v}{\partial x} = \frac{\partial w}{\partial x} = \frac{\partial T}{\partial x} = \frac{\partial \phi}{\partial x} = 0 \tag{2.23}$$

- At $z = 0$ and $z = Z$

$$w = \frac{\partial u}{\partial z} = \frac{\partial v}{\partial z} = \frac{\partial T}{\partial z} = \frac{\partial \phi}{\partial z} = 0 \tag{2.24}$$

- At $y = 0$

$$u = v = w = 0; \;\; \frac{\partial \phi}{\partial y} = -cos\varphi; \;\; \left(T|_{y=0}\right)_f = \left(T|_{y=0}\right)_s \tag{2.25}$$

- At $y = Y$

$$\frac{\partial u}{\partial y} = \frac{\partial v}{\partial y} = \frac{\partial w}{\partial y} = \frac{\partial \phi}{\partial y} = 0; \;\; T = T_{sat} \tag{2.26}$$

2.5 Solid Substrate Region

In the solid substrate, the spatial and temporal variation of the substrate temperature (T_s) is obtained by solving the three-dimensional transient conduction equation shown below

$$\rho_s c_s \frac{\partial T_s}{\partial t} = k_s \left(\frac{\partial^2 T_s}{\partial x^2} + \frac{\partial^2 T_s}{\partial y^2} + \frac{\partial^2 T_s}{\partial z^2} \right) \tag{2.27}$$

The boundary conditions for the transient conduction equation in a substrate of thickness *L* are as follows:

- At the lateral faces

$$\frac{\partial T_s}{\partial x} = 0 \;\; at \;\; x = 0, X; \quad \frac{\partial T_s}{\partial z} = 0 \;\; at \;\; z = 0, Z \tag{2.28}$$

- At the bottom face ($y = -L$)

$$-k_s \frac{\partial T_s}{\partial y} = q_{w,in} \tag{2.29}$$

- At the top face ($y = 0$)

$$\left(-k \frac{\partial T}{\partial y}|_{y=0}\right)_s = \left(-k \frac{\partial T}{\partial y}|_{y=0}\right)_f \tag{2.30}$$

The procedure for coupling the temperature and heat flux at the solid-fluid interface ($y = 0$), obtained from solutions of the solid-side and fluid-side energy equations is described in the next section.

2.6 Computational Framework

The characteristic length, velocity and time scales used to obtain the non-dimensional forms of the governing equations on the fluid side in the present numerical model are as follows:

$$l_0 = \sqrt{\frac{\sigma}{g(\rho_l - \rho_v)}}, \qquad u_0 = \sqrt{g l_0}, \qquad t_0 = \frac{l_0}{u_0} \tag{2.31}$$

To maintain consistency with the fluid-side non-dimensional equations, the same length and time scales as in Eq. (2.31) are used to normalize the transient conduction equation in the solid substrate. Using the properties of saturated water at atmospheric pressure, the characteristic length, velocity and time scales in the present study are l_0 = 2.5 mm, u_0 = 0.157 m/s and t_0 = 15.9 ms.

The non-dimensional temperatures on the fluid side and solid side are defined as

$$\theta = \frac{T - T_{sat}}{T_{nuc} - T_{sat}} \tag{2.32}$$

where T_{nuc} is the nucleation temperature, which is the temperature of the cavity site that is necessary for bubble nucleation to occur at the site. The quantity $T_{nuc} - T_{sat}$ is referred to as the nucleation superheat, denoted by ΔT_{nuc}. The cavity nucleation superheat generally depends on the cavity geometry and the surface wettability [1,2]. A cavity nucleation superheat of 6 °C is chosen for all the simulations in the present study, and it is assumed that there are no other active cavity sites with lower or higher nucleation superheats in the region of interest in this study.

At the start of the simulations, the entire boiling surface ($y = 0$) is assumed to be at a uniform temperature of T_{nuc}, the nucleation temperature. The liquid is initially assumed to be stationary and is at saturation temperature everywhere except for the thermal boundary layer close to the boiling surface. The initial liquid thermal boundary layer thickness is determined by assuming that there are no active nucleation sites prior to the start of the simulations, and that turbulent natural convection prevails over the boiling surface initially. The following correlation from Kays and Crawford [43] for turbulent natural convection is used to calculate the initial thermal boundary layer thickness

$$\delta_t = 7.14 \left(\frac{\nu_l \alpha_l}{g \beta \Delta T_{nuc}} \right)^{\frac{1}{3}} \tag{2.33}$$

The temperature of liquid in the thermal boundary layer, in the initial condition, varies linearly from T_{nuc} on the boiling surface to the saturation temperature T_{sat} at the outer edge of the thermal layer. An initial linear temperature distribution is obtained in the solid with the uniform temperature (T_{nuc}) on its top surface and a uniform heat flux at the bottom face of the substrate, corresponding to turbulent natural convection at the nucleation superheat. For t > 0, the heat flux imposed at the bottom face of the solid substrate is increased to $q_{w,in}$ = 1.1 W/cm^2 and is held constant at that value throughout the simulation. For the nucleation superheat of 6 °C considered

for the cavity sites in the present study, the above specified value of imposed heat flux at the bottom face of the substrate is sufficient to facilitate sustained nucleate boiling while being small enough to prevent vertical merger of bubbles from a given cavity site.

A small bubble of radius 0.25 mm is initially placed over the cavity site. When a vapor bubble departs from the cavity site, the subsequent bubble is placed at the site when the boiling surface temperature at the cavity site recovers back to the nucleation temperature (106 °C). The time corresponding to this recovery of the cavity site temperature is the waiting time. The simulation is run for multiple bubble cycles until a quasi-steady condition is reached wherein the wall heat flux averaged over the entire boiling surface and over the entire bubble cycle ($t_g + t_w$) is equal to the imposed heat flux, and there are no significant changes from one cycle to the next.

On the fluid side, a staggered grid is employed such that the temperature, pressure and level set function values are stored at the cell centers, and the three velocity components are stored at the centers of the cell faces in the corresponding directions. Such a staggered grid eliminates the issue of spurious checkerboard oscillations in pressure, likely to occur in a collocated grid where the pressure and velocity values are stored at the same location. Since there is no separate equation of state for incompressible flows, a pressure-projection method is used to decouple the pressure and the velocity components in the momentum conservation equations. In this method the mass conservation and momentum conservation equations are combined and later refactored into a new set of momentum equations without the pressure gradient terms and a separate pressure Poisson equation. A multigrid method with six levels is used to increase the rate of convergence of the solution to the Poisson equation. In the mass, momentum and energy conservation equations, convection terms are discretized explicitly using a second-order essentially non-oscillatory (ENO) scheme and diffusion terms are discretized implicitly using a central difference scheme. For the

level set advection and re-initialization equations, a fifth-order weighted essentially non-oscillatory (WENO) scheme is used for spatial derivatives, and a third-order total variation diminishing Runge-Kutta (TVD-RK) scheme is used for the time derivatives.

On the solid-side, a three-dimensional alternating-direction implicit (ADI) method is used to solve the transient conduction equation. The conduction equation is first discretized using the Crank-Nicolson scheme to obtain second order accuracy in both space and time. This discretized equation is then factorized and rewritten as three separate equations in three fractional time steps, as demonstrated by Douglas and Gunn [44].

The solution procedure followed in the numerical model is outlined below

1. The level-set advection equation (Eq. (2.21)) and level-set reinitialization equation (Eq. (2.22)) are solved to determine the updated position of the liquid-vapor interface.
2. Next, the fluid-side and solid-side energy equations are solved to determine the temperature distribution. The temperature and heat flux from the two regions are coupled at the solid-fluid interface for a given time step as follows:
    a. The fluid-side energy equation is first solved, using the most recent temperature distribution at the solid-fluid interface as a boundary condition.
    b. From the newly obtained temperature distribution in the fluid, the heat flux at the solid-fluid interface is calculated. Using this updated heat flux as the boundary condition at the top boundary of the solid side, the transient conduction equation is solved in the solid substrate. An updated temperature of the solid-fluid interface is now available as the boundary condition for the fluid-side energy equation.

c. The above steps are repeated until the temperature and heat flux at the solid-fluid interface undergo insignificant changes between successive iterations, and the solid-side and fluid-side temperature and heat flux solutions match at the interface, at which point the simulation proceeds to the next step.

3. The momentum equations, which are part of the projection method, are solved to obtain the initial estimate of the velocity components (u, v, w) in the three directions. This velocity field does not necessarily satisfy the continuity equation (Eq. 2.12).
4. The pressure Poisson equation is solved to obtain the updated pressure gradient in the fluid.
5. Using the newly obtained pressure gradient, the velocity correction equations are solved to obtain the velocity field that satisfies the continuity equation.
6. The simulation proceeds to the next time step.
7. The above steps are repeated for all subsequent time steps until the end of the simulation.

2.7 Grid independence study

Figure 2.3 shows the variation of the equivalent bubble diameter during one bubble cycle (growth period and waiting time) obtained for numerical simulations of nucleate pool boiling on a 7 mm × 7 mm portion of a horizontal stainless-steel substrate having two active cavity sites with spacing S = 3 mm, for three different grid resolutions. As described in Section 2.1, the computations are carried out for one quarter (3.5 mm × 3.5 mm with symmetry conditions) of the region of interest. The equivalent diameter shown in the figure is based on the total volume of the vapor bubbles attached to the boiling surface at the two cavity sites. A constant heat flux of 1.1 W/cm^2 is imposed at the bottom face of the substrate, and the cavity nucleation superheat is 6 ℃, for the three cases.

The three grid resolutions considered on the fluid side for the grid independence study are 64 × 256 × 64, 96 × 384 × 96, and 128 × 512 × 128 grids. The corresponding grid resolutions on the solid side are 64 × 10 × 64, 96 × 28 × 96, and 128 × 36 × 128 grids.

It is seen in Fig. 2.3 that the bubble departure diameter, growth period and waiting time between the cases with 96 x 384 x 96 grids and 128 x 512 x 128 grids on the fluid side differ by less than 3 %. Based on this, the 96 x 384 x 96 grid resolution is selected for the present study to reduce computational cost while preserving a reasonable accuracy of the results.

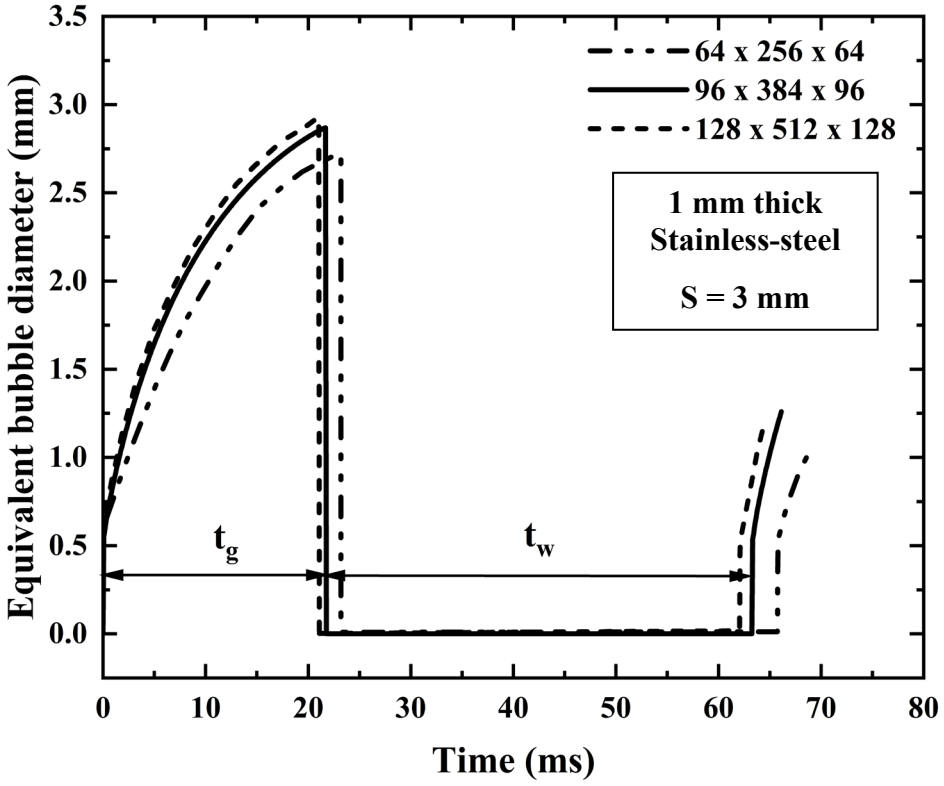

Fig. 2.3: Variation of equivalent bubble diameter during one bubble cycle for pool boiling on a 1 mm thick stainless-steel substrate, for three different computational grid resolutions. $q_{w,in}$ = 1.1 W/cm^2, ΔT_{nuc} = 6 °C, φ = 35°.

2.8 Model Validation

Zhang and Shoji [23] performed experiments for pool boiling of saturated water at atmospheric pressure on 0.2 mm thick polished silicon wafers having two adjacent fabricated active nucleation sites with different cavity spacings to study the interaction between the adjacent nucleation sites during saturated pool boiling of water. To validate the numerical model used in the present study, simulations are performed under conditions similar to those in the experiments, and the bubble departure frequencies obtained for different cavity spacings are compared to those in the experiments, as shown in Fig. 2.4.

For validating the present numerical model, simulations are carried out for saturated pool boiling of water on a 12 mm x 12 mm portion of a 0.2 mm thick horizontal silicon substrate with two adjacent nucleation sites under an imposed heat flux of 2.7 W/cm^2, which is the wall heat flux in the reference experiments of Zhang and Shoji [23]. The values of cavity spacings considered in these simulations are 1 mm, 2 mm, 3 mm, 4 mm, 6 mm and 8 mm, which are the same spacings studied in the reference experiments. In the simulations, the two cavity sites are assumed to be identical and only a 6 mm x 6 mm portion of the substrate is considered for the computations, taking advantage of the symmetry. A waiting time of less than 1 ms is observed in the simulations, and this is consistent with the images obtained from the experiments [23], wherein a bubble is seen to nucleate at a cavity site immediately after the previous bubble departs from the site. The average departure diameter for a single bubble without any merger was observed to be about 2.4 mm. Lateral bubble merger is observed mainly for cavity spacings of 1 mm and 2 mm. Vertical bubble mergers occur for all the cavity spacings. The predicted dependence of bubble departure frequency

on cavity spacing, as shown in Fig. 2.4, was explained by Zhang and Shoji [23] to be the result of relative intensities of the thermal interaction between the cavities, hydrodynamic interaction of bubbles with the bulk liquid, and bubble merger.

The bubble departure frequencies for the two smallest cavity spacings are significantly higher than that for the largest cavity spacing since lateral bubble merger causes the bubbles to depart earlier, as explained in detail in Chapter 3. In the experiments, there may be some heat loss in the radial direction whereas in the simulations the substrate ends are assumed to be adiabatic. The contact angle in the experiments was not specified and a static contact angle of 35° was assumed in the simulations based on bubble images provided for the experiments. A cavity nucleation superheat of 10 °C was chosen for the simulations based on the requirement that the bubble departure frequency closely matches that from the experiments for the largest cavity spacing. Based on Fig. 2.4, the numerically predicted results are found to be in good agreement with those reported in the experiments of Zhang and Shoji [23], with the present simulations predicting bubble departure frequencies that are within 15 % of the corresponding values reported in the experiments, for cavity spacings varying from 1 mm to 8 mm.

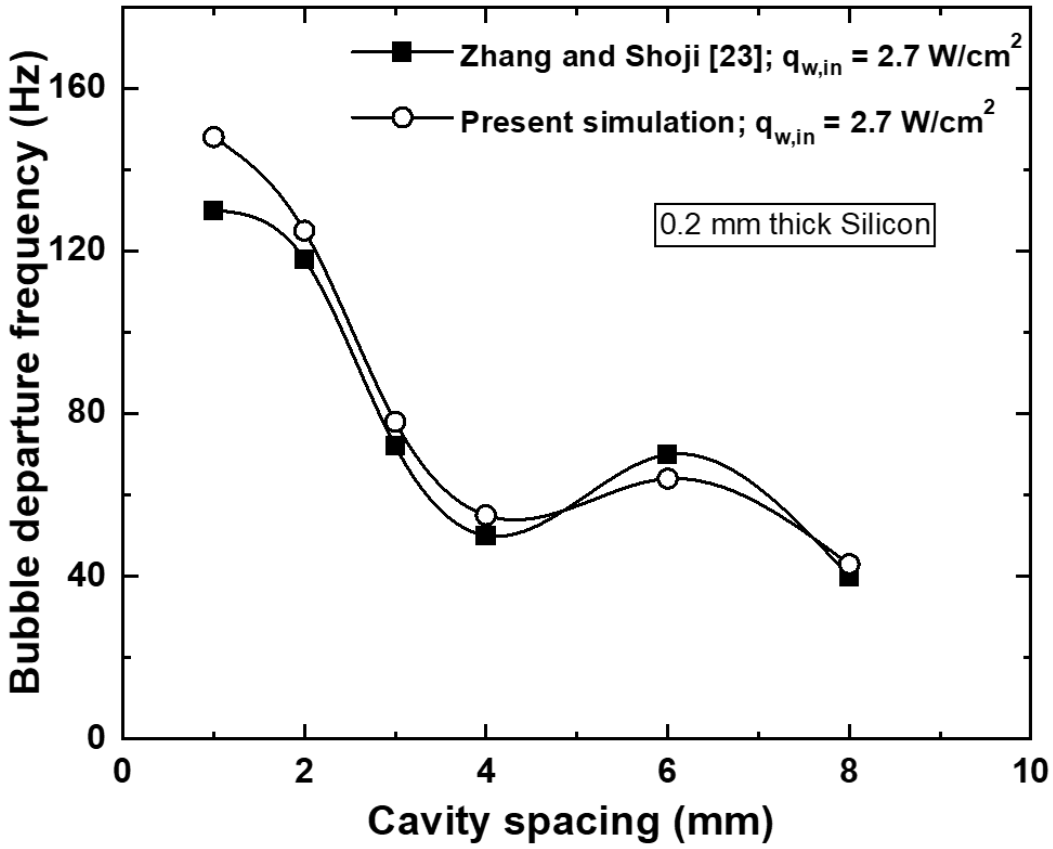

Fig. 2.4: Variation of bubble departure frequency with cavity spacing for a 0.2 mm thick silicon substrate — comparison of results of present model and experiments [23]. In the simulations, φ = 35° and ΔT_{nuc} = 10 °C.

Chapter 3

Effect of Cavity Spacing and Lateral Bubble Merger

This chapter provides useful insights into the influence of cavity spacing and lateral bubble merger on bubble dynamics and heat transfer during nucleate pool boiling on a horizontal substrate with two adjacent active cavity sites, with the spacing between the sites being parametrically varied.

3.1 Study Parameters

Numerical simulations are performed for saturated pool boiling of water on a 7 mm x 7 mm portion of a 1 mm thick horizontal stainless-steel substrate having two adjacent active cavity sites. A constant heat flux of 1.1 W/cm^2 is imposed at the bottom face of the substrate, and a cavity nucleation superheat of 6°C is used for all the cases presented, representing conditions of boiling inception. A static contact angle of 35° is used in all the cases discussed in this chapter. Six different values of the cavity spacing S, namely 3 mm, 2.6 mm, 2.2 mm, 1.8 mm, 1.4 mm and 1 mm, are considered in this study. Under the conditions for which the simulations in this study are performed, there is no vertical bubble merger, and the focus is on lateral merger of bubbles. All the results presented in the subsequent section correspond to the quasi-steady conditions, wherein the simulation shows insignificant changes from one bubble cycle to the next, and the heat flux averaged over the area of boiling surface within the computational domain (3.5 mm × 3.5 mm with symmetry conditions) and over one bubble cycle ($t_g + t_w$), is equal to the imposed heat flux.

3.2 Results and Discussion

3.2.1 Patterns of bubble departure

Of the six different cavity spacings studied, lateral bubble merger occurs for the spacings 2.2 mm, 1.8 mm, 1.4 mm and 1 mm. For the cavity spacings 3 mm and 2.6 mm, bubbles from the two adjacent cavity sites do not merge with each other and depart from the boiling surface as two isolated bubbles, each with an equivalent diameter of about 2.3 mm.

As a representative case of cavity spacings wherein lateral bubble merger does not occur, Fig. 3.1(a) shows the temporal evolution of the bubbles during growth and departure for the cavity spacing S = 3 mm.

For the cases with lateral bubble merger, two distinct patterns of bubble departure are observed as described below:

i. The first pattern of bubble merger and departure is found in the cases S = 2.2 mm and S = 1.8 mm. Figure 3.1(b) shows the bubble merger and departure process for S = 2.2 mm, representing the first pattern of bubble merger and departure. In this case, the merged vapor mass, just after lateral bubble merger, is already larger than that of a single isolated bubble at departure in the case without lateral bubble merger (S = 3 mm), and this merged vapor mass detaches from the boiling surface soon after merger. During the detachment process the merged vapor mass pinches off from the boiling surface at the two locations corresponding to the bases of the two individual bubbles before merger. When the bubble detaches from the boiling surface it is elongated in the x-direction. The bubble hovers close to the boiling surface,

undergoes oscillations in the x and z directions due to surface tension. Once the bubble attains a near-spherical shape, it rises in the liquid and moves away from the boiling surface.

ii. The second pattern of bubble merger and departure is observed in the cases S = 1.4 mm and S = 1 mm. As a representative case of this pattern, Figure 3.1(c) shows the bubble shapes during the growth period and departure in the case of S = 1 mm. The two bubbles merge and some liquid is found to be trapped underneath the vapor bridge connecting the two bubbles. This trapped liquid layer is commonly referred to as a liquid macrolayer [26]. With continued evaporation at the liquid-vapor interface, the vapor bridge expands and pushes out the trapped liquid. When all the trapped liquid is pushed out there is a merged vapor mass attached to the surface, resembling a single isolated bubble. This merged vapor bubble continues to grow, and during the final stages of the growth period, the base of the bubble starts to shrink until eventually the bubble detaches from the boiling surface. The detached bubble in this case is closer to a spherical shape, similar to that in the case of S = 3 mm. This departed bubble continues to move upwards away from the boiling surface, unlike in the case of S = 2.2 mm where the bubble initially hovers near the boiling surface before eventually rising up in the liquid.

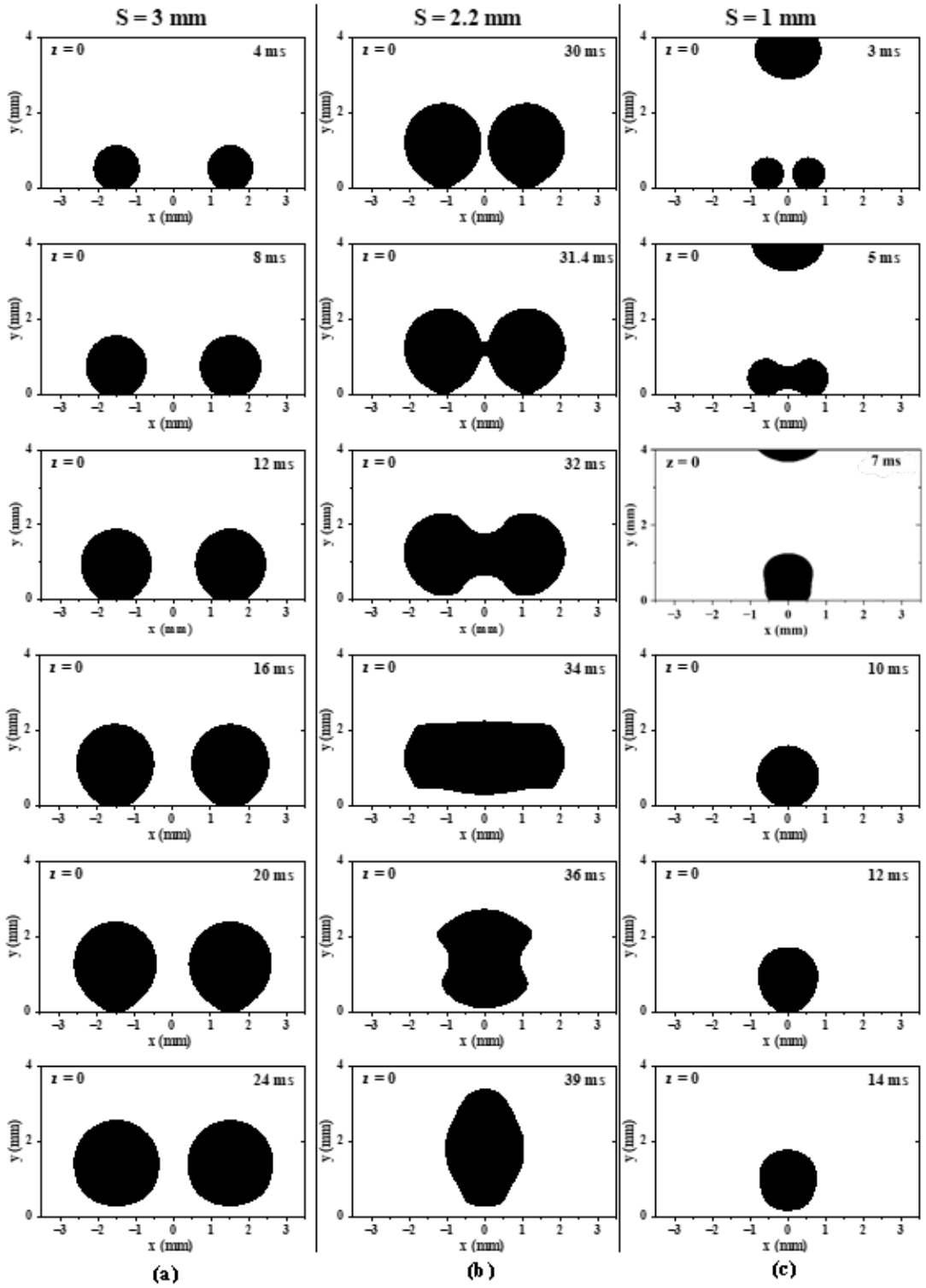

Fig. 3.1: Evolution of bubble shapes during the growth period and bubble departure for a 1 mm thick stainless-steel substrate for (a) S = 3 mm, (b) S = 2.2 mm and (c) S = 1 mm.

($q_{w,in}$ = 1.1 W/cm^2, ΔT_{nuc} = 6 °C, φ = 35°)

2.2.2 Cavity site temperature evolution

Figures 3.2(a) and 3.2(b) illustrate the variation of the cavity site temperature during the growth and waiting periods, for cases without bubble merger (S = 3 mm) and with lateral bubble merger (S = 1 mm), respectively.

For S = 3 mm, as seen in Fig. 3.2(a), the cavity site temperature shows a small drop during the first 5 ms following bubble nucleation, caused by the high local heat flux from microlayer evaporation near the three-phase contact line. As the bubble grows, its base expands, resulting in an enlarged dry region around the cavity site. During this stage, the cavity site temperature continues to decrease but at a slower rate. As the vapor bubble continues to grow, the bubble base also grows until it reaches its maximum size at around 9 ms, after which it begins to shrink. As the three-phase contact line moves inward towards the cavity site, the cavity site temperature decreases at a faster rate. When the bubble base pinches off the cavity site as it detaches from the boiling surface at about 22 ms, the cavity temperature experiences a sharp drop. After bubble departure, there is a waiting period of about 40 ms, during which the cavity site temperature recovers back to the nucleation temperature (106 ℃). At this point, the next bubble nucleates at the cavity site.

For S = 1 mm, as seen in Fig. 3.2(b), the cavity temperature decreases following bubble nucleation, as in the case of S = 3 mm, due to the high heat transfer associated with microlayer evaporation. At around 5 ms the two bubbles merge, soon after which the cavity temperature can be seen to decrease at a faster rate. This is due to an increase in the microlayer area after bubble merger, since two smaller bubble bases before merger now become one relatively larger bubble base. At around 6 ms, the base of the merged bubble starts to shrink. The three-phase contact line crosses the cavity

site, at which point there is a sharp drop in the cavity temperature. The bubble base continues to shrink as the vapor bubble grows, moving towards the midpoint (x = 0) between the two cavity sites. The cavity temperature starts to recover while the bubble has still not departed from the boiling surface. The bubble departs at around 14 ms, after which there is waiting period of about 17 ms before the next bubble nucleates.

The key difference between the variation of the cavity site temperature during the bubble cycle for the two cavity spacings is that for S = 3 mm, the cavity site temperature reaches its minimum value just as the bubble departs from the boiling surface, while for S = 1 mm the cavity site temperature reaches its minimum value, and starts to recover before the vapor bubble departs from the boiling surface.

(a)

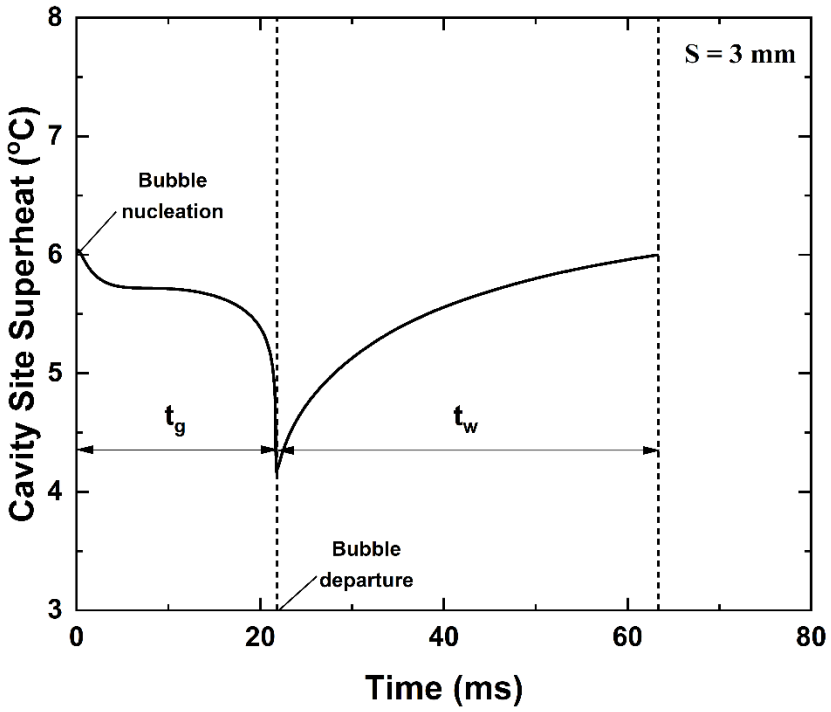

(b)

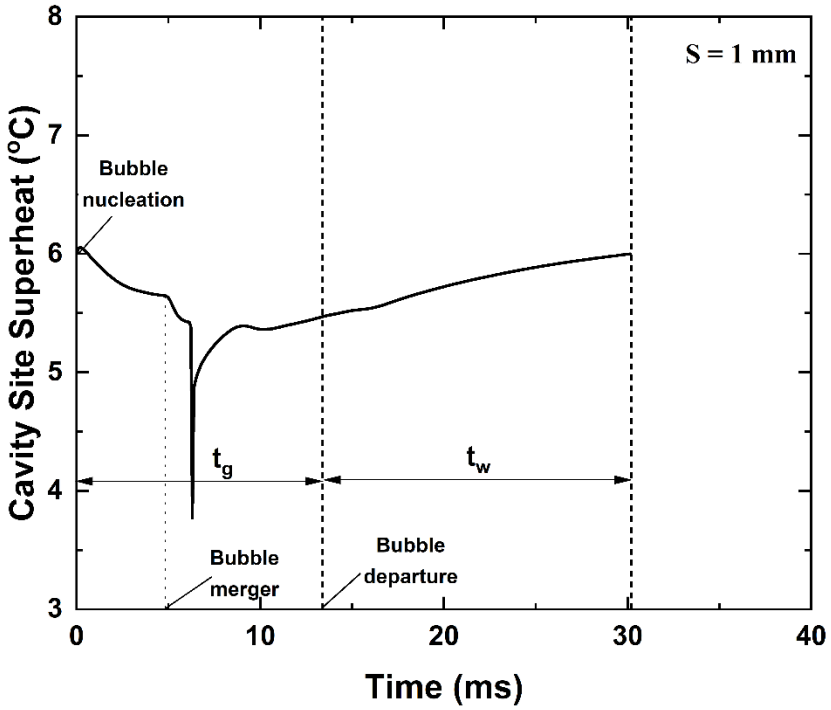

Fig. 3.2: Variation of cavity site temperature with time during one bubble cycle for a 1 mm thick stainless-steel substrate for cavity spacings of (a) S = 3 mm and (b) S = 1 mm.

($q_{w,in}$ = 1.1 W/cm^2, ΔT_{nuc} = 6 °C, φ = 35°)

3.2.3 Waiting Time

Figure 3.3 shows the variation of the equivalent bubble diameter with time for the six different cavity spacings. The solid lines correspond to the equivalent diameter determined from the total vapor volume attached to the boiling surface. The dashed lines correspond to the equivalent diameter of each individual bubble. In the cases with lateral bubble merger, it is observed that the bubbles merge progressively earlier as the distance between the cavity sites decreases, as shown in Fig. 3.3. While some variations are observed in the bubble growth period and bubble departure diameter across the different spacings, the most significant dependence on cavity spacing is seen for the waiting time. The study results clearly indicate that the cavity spacing, and lateral bubble merger if any, have a substantial influence on the waiting time during nucleate pool boiling with two adjacent active cavity sites.

For a given substrate material and thickness, the waiting time is primarily dictated by the extent of the boiling surface that experiences a temperature deficit relative to the nucleation temperature, as a result of bubble growth and departure. Within this region of temperature-deficit, the boiling surface temperature must recover until the cavity site temperature reaches the nucleation temperature, enabling subsequent bubble nucleation. Figure 3.4 shows the spatial temperature distribution on the boiling surface 5 ms after bubble departure for different cavity spacings. The shaded regions represent areas of temperature deficit relative to the nucleation temperature. As the cavity spacing increases from 1 mm to 1.8 mm the area of temperature deficit expands. This increase is attributed to the fact that with greater spacing the bubbles from the adjacent cavities attain larger sizes before merging, leading to a reduction in surface temperature over a larger extent

of the boiling surface. As the cavity spacing further increases from 1.8 mm to 3 mm, the neighboring bubbles either merge just before departure (~ 0.5 ms), as in the case of S = 2.2 mm, or depart from the boiling surface as isolated bubbles without merger, as observed for S = 2.6 mm and S = 3 mm. Consequently, the boiling surface temperature deficit in these scenarios is confined to the region of the boiling surface traversed by the bubble bases around the two cavity sites.

Consistent with the variation of the area of temperature deficit with cavity spacing, the waiting time increases as the spacing increases from 1 mm to 1.8 mm and decreases with further increase in spacing from 1.8 mm to 3 mm, as shown in Fig. 3.5. The largest waiting time in this study, associated with two merging bubbles at S = 1.8 mm, is about 5.5 times that of the smallest waiting time, observed for two merging bubbles at S = 1 mm.

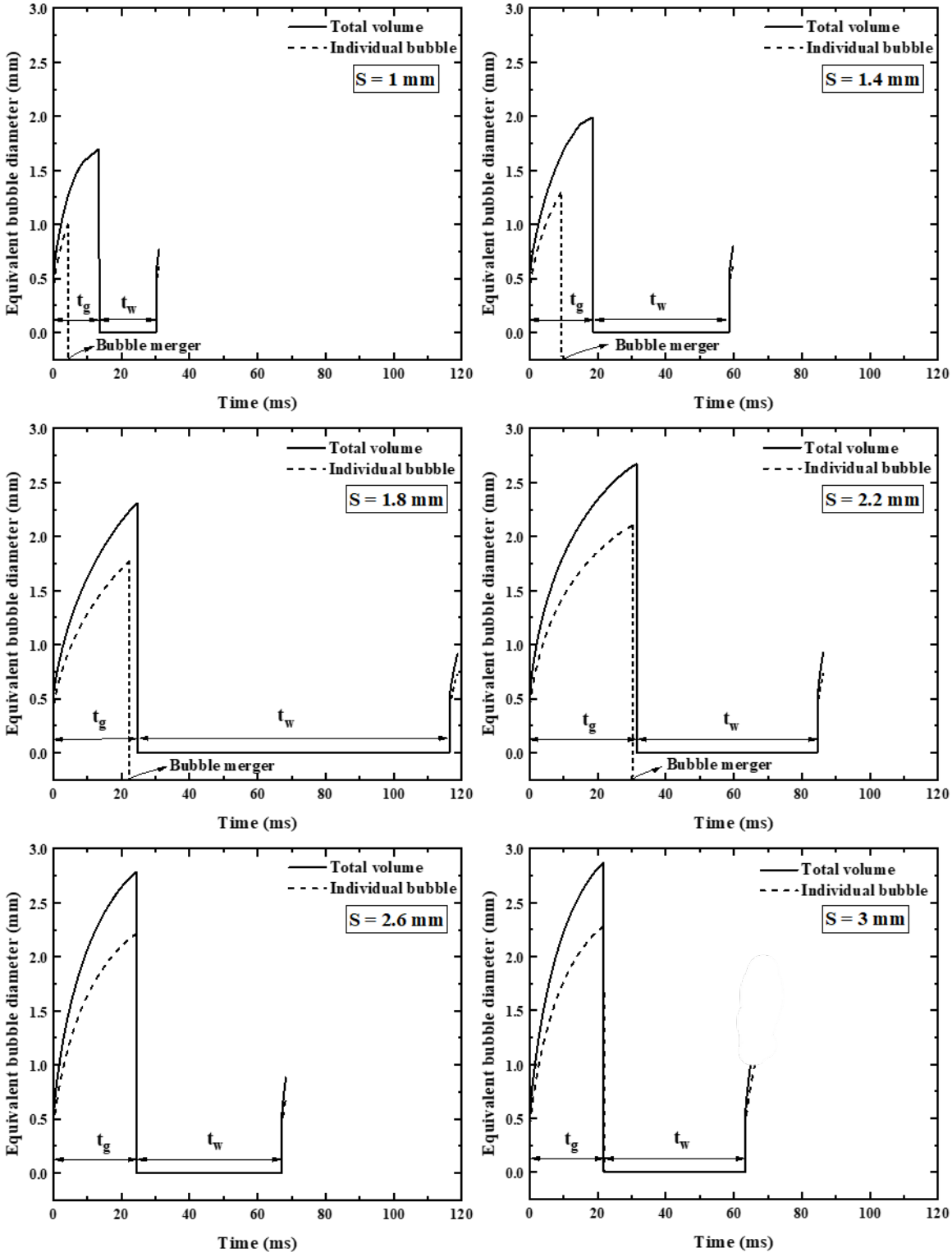

Fig. 3.3: Temporal variation of equivalent bubble diameter for a 1 mm thick stainless-steel substrate for six different cavity spacings. ($q_{w,in}$ = 1.1 W/cm^2, ΔT_{nuc} = 6 °C, φ = 35°)

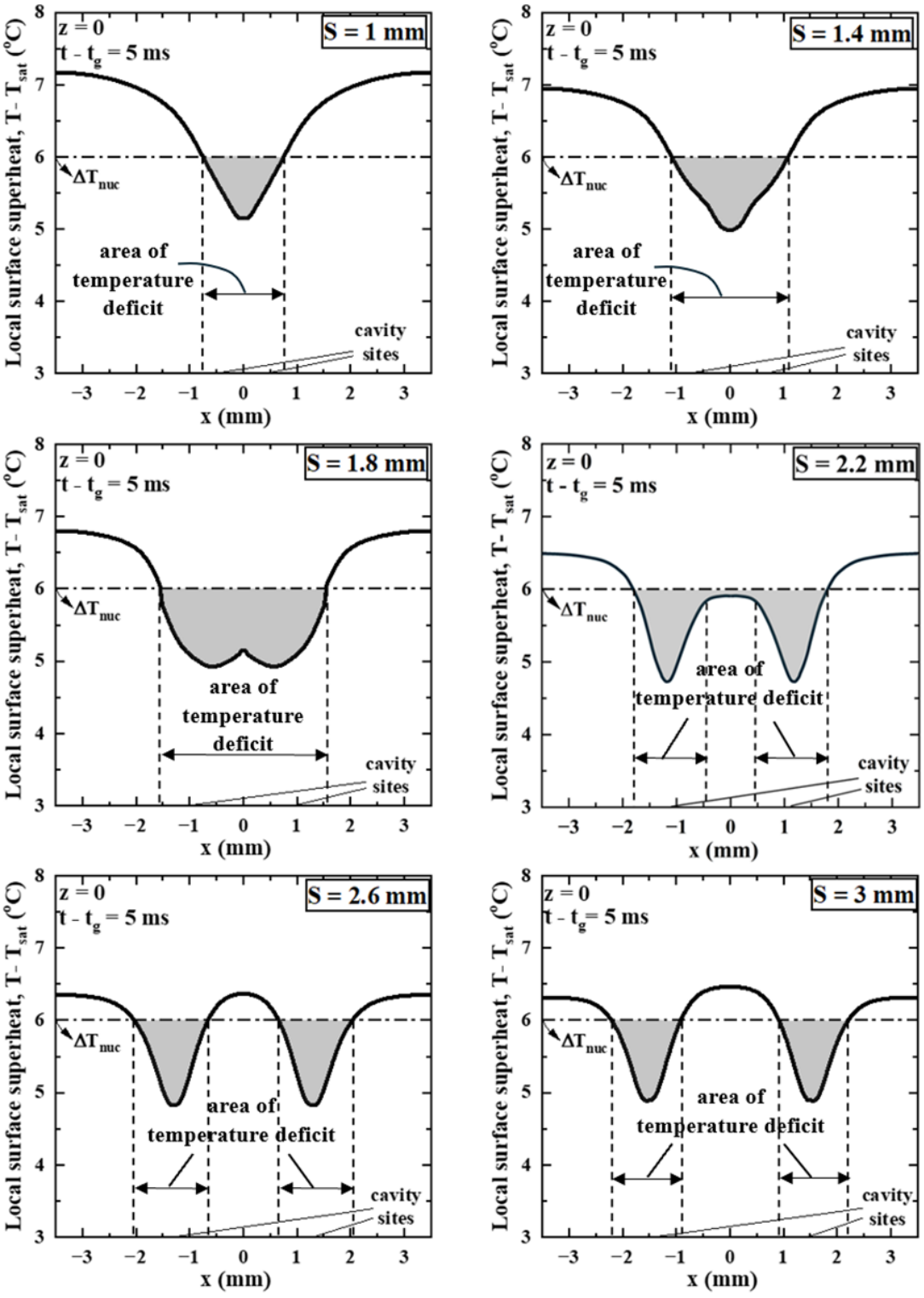

Fig. 3.4: Spatial distribution of boiling surface temperature for a 1 mm thick stainless-steel substrate 5 ms post bubble departure for different cavity spacings. ($q_{w,in}$ = 1.1 W/cm^2, ΔT_{nuc} = 6 °C, φ = 35°)

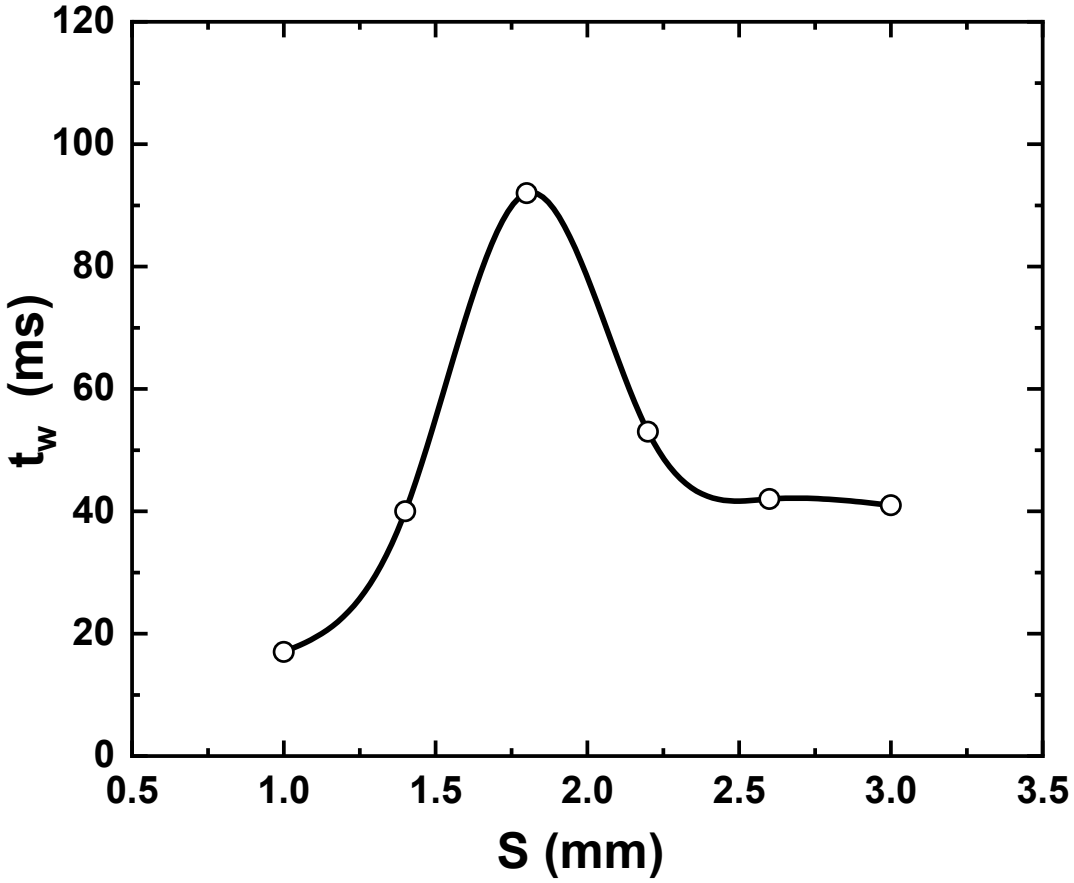

Fig. 3.5: Variation of waiting time with cavity spacing for a 1 mm thick stainless-steel substrate. ($q_{w,in}$ = 1.1 W/cm^2, ΔT_{nuc} = 6 °C, φ = 35°)

3.2.4 Bubble Departure Diameter and Bubble Growth Period

Figure 3.6 shows the relationship between the equivalent bubble departure diameter and cavity spacing. The bubble departure diameter is governed by the relative magnitudes of various vertical forces acting on the bubble. The equivalent departure diameter for two non-merging bubbles at S = 3 mm is 2.85 mm while that for two non-merging bubbles at S = 2.6 mm is nearly identical at 2.82 mm. For cavity spacings less than or equal to 2.2 mm, the flow field induced by the bubble merger generates an additional upward lift force on the bubble. This effect is substantiated by the pressure distribution around the merged bubble, as shown in Fig. 3.7 for S = 1.4 mm, where p_{max} and p_{min} are the maximum and minimum pressures in the region shown. Due to this effect, the bubble departure diameter for S = 2.2 mm is smaller than those for the cases S = 2.6 mm and S = 3 mm. Furthermore, as the cavity spacing decreases from 2.2 mm to 1 mm, the bubbles merge progressively earlier, and the additional lift force resulting from this merger facilitates bubble departure at smaller sizes. Consequently, the bubble departure diameter exhibits a decreasing trend as the cavity spacing decreases from 2.2 mm to 1 mm, as shown in Fig. 3.6.

To summarize, the bubble departure diameter decreases with decrease in cavity spacing. Quantitatively, the smallest bubble departure diameter, corresponding to two merging bubbles at S = 1 mm, is approximately 35 % smaller than that for two non-merging bubbles at S = 3 mm.

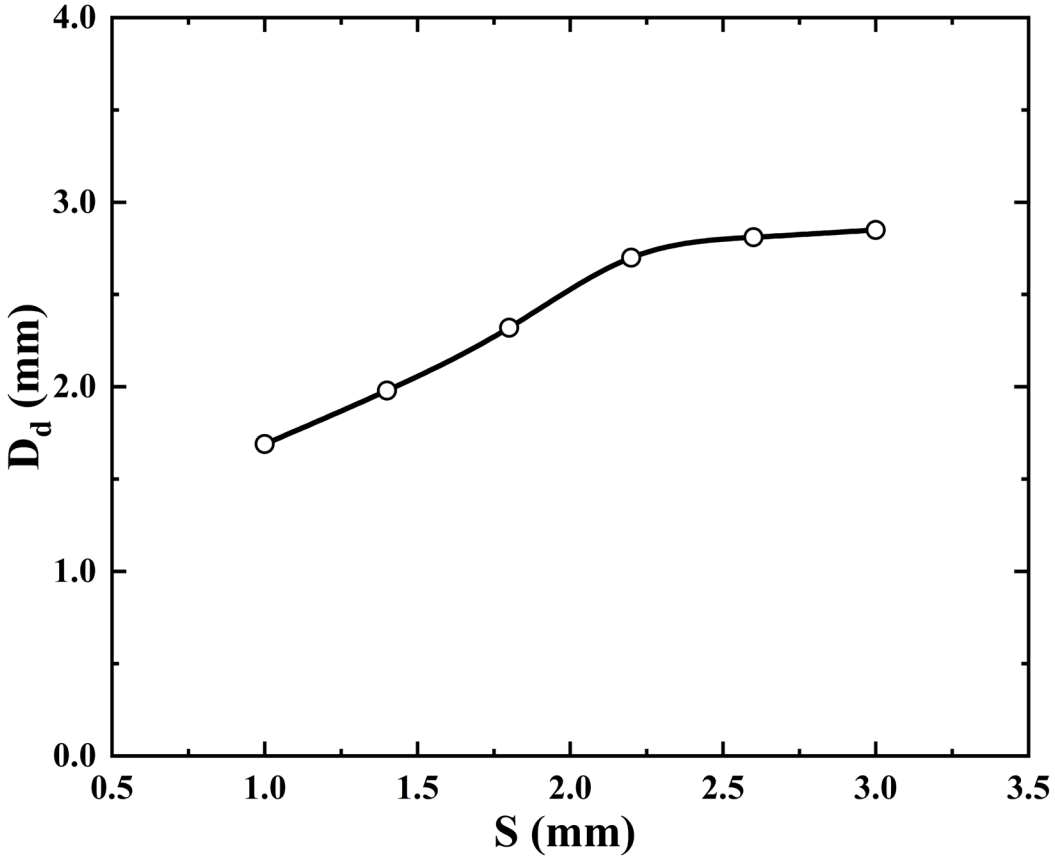

Fig. 3.6: Variation of equivalent bubble departure diameter with cavity spacing for a 1 mm thick stainless-steel substrate. ($q_{w,in}$ = 1.1 W/cm^2, ΔT_{nuc} = 6 °C, φ = 35°)

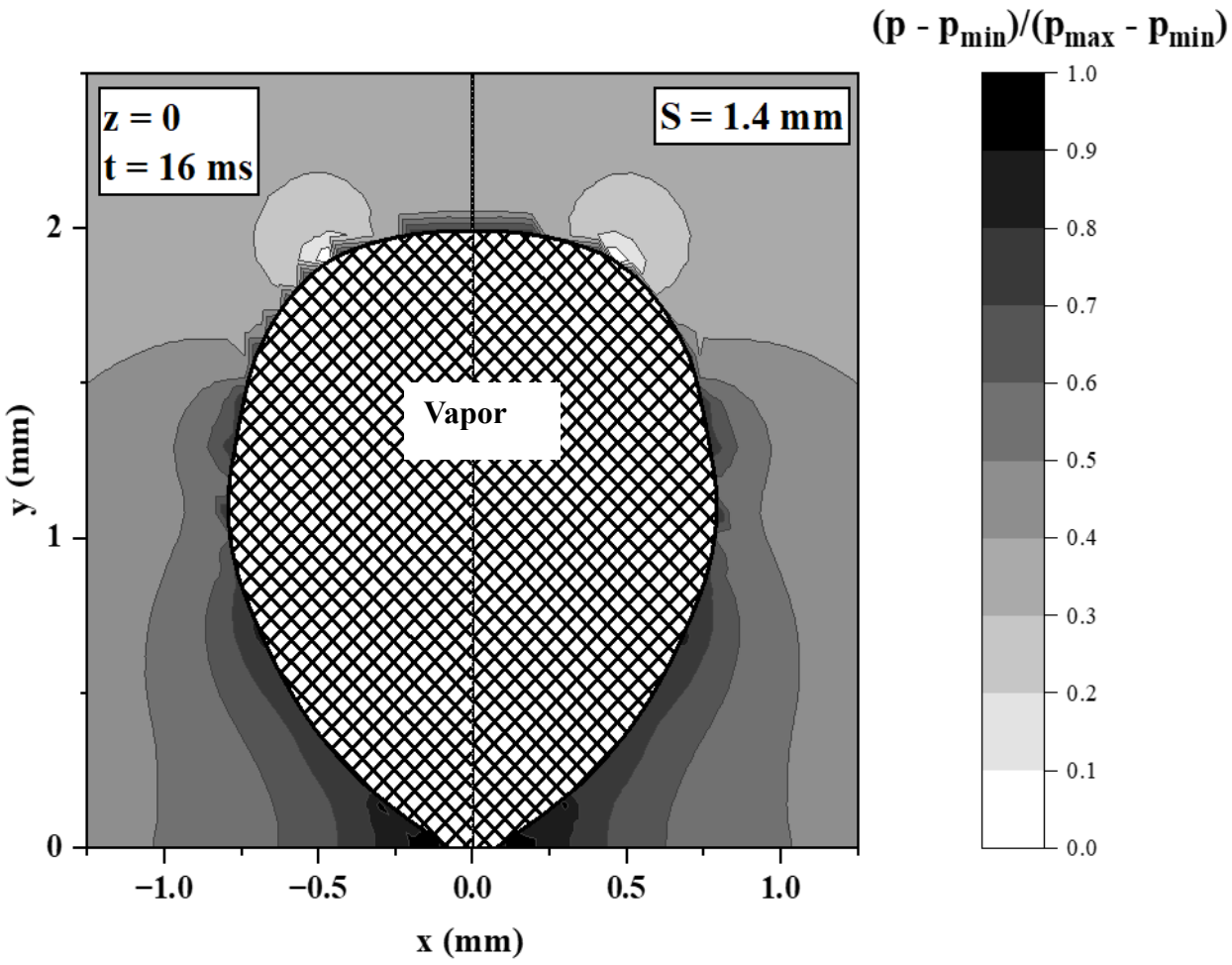

Fig. 3.7: Pressure distribution in the liquid surrounding a merged bubble for a 1 mm thick stainless-steel substrate with a cavity spacing of S = 1.4 mm. ($q_{w,in}$ = 1.1 W/cm^2, ΔT_{nuc} = 6 °C, φ = 35°)

Figure 3.8(a) presents the boiling surface temperature near the left-side cavity immediately prior to bubble nucleation for different cavity spacings. Within the inter-cavity region, the surface temperature decreases progressively with decrease in cavity spacing from 3 mm to 1 mm. Outside this region, the boiling surface temperature near the cavity site initially decreases from S = 3 mm to S = 2.2 mm, followed by an increase with further decrease in spacing to S = 1 mm. This variation of the boiling surface temperature near the cavity site with the cavity spacing dictates the variation in bubble growth rate. As shown in Fig. 3.8(b), the bubble growth rate (based on the slope of the curves) is seen to decrease from S = 3 mm to S = 1.8 mm and remains mostly unchanged from S = 1.8 mm to S = 1 mm.

Figure 3.9 shows the variation of the bubble growth period with cavity spacing for a 1 mm thick stainless-steel substrate. The trends in bubble departure diameter (Fig. 3.6) and bubble growth rate (Fig. 3.8(b)) collectively account for the dependence of the bubble growth period with cavity spacing. The bubble growth period increases as the cavity spacing decreases from S = 3 mm to S = 2.2 mm, as shown in Fig. 3.9, and this is attributed to the decrease in bubble growth rate. However, as the cavity spacing further decreases from S = 2.2 mm to S = 1 mm, the bubble growth period decreases despite a decrease in bubble growth rate, and this is because the bubble departure diameter reduces by about 35 % across this range of cavity spacing. The longest bubble growth period, corresponding to S = 2.2 mm, is about 2.3 times that of the shortest growth period, observed at S = 1 mm.

(a)

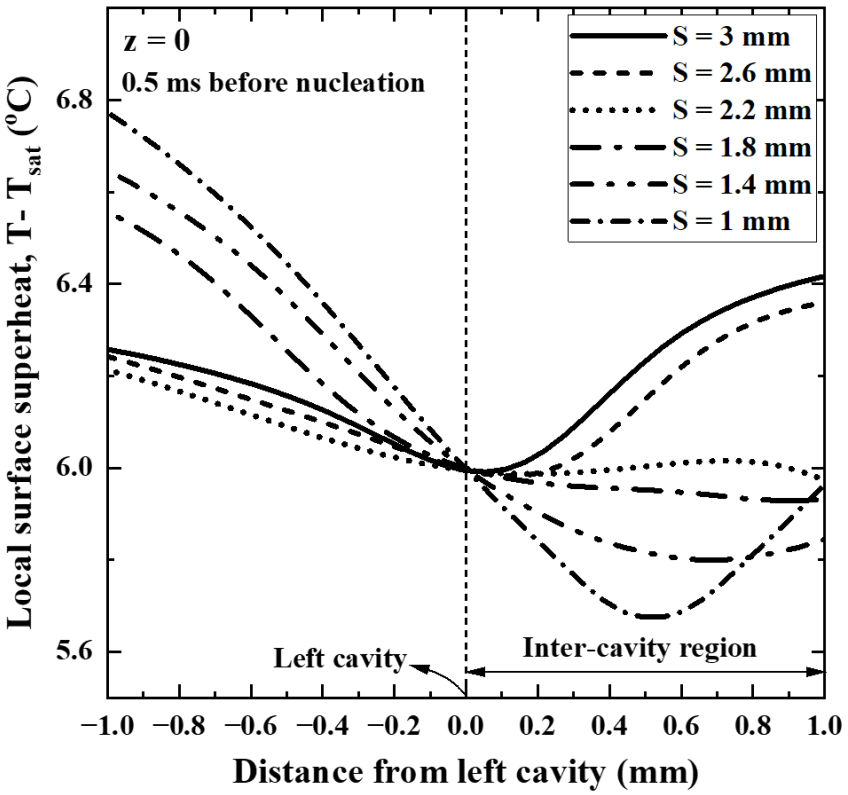

(b)

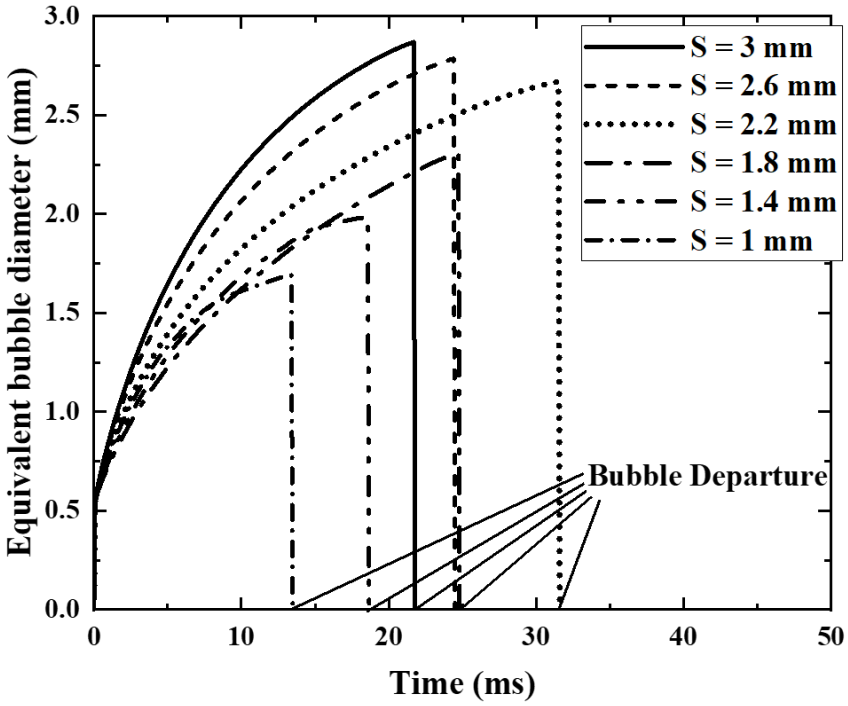

Fig. 3.8: (a) Boiling surface temperature in the vicinity of the left-side cavity just before bubble nucleation and (b) bubble growth histories, for a 1 mm thick stainless-steel substrate with different cavity spacings. ($q_{w,in}$ = 1.1 W/cm^2, ΔT_{nuc} = 6 °C, φ = 35°)

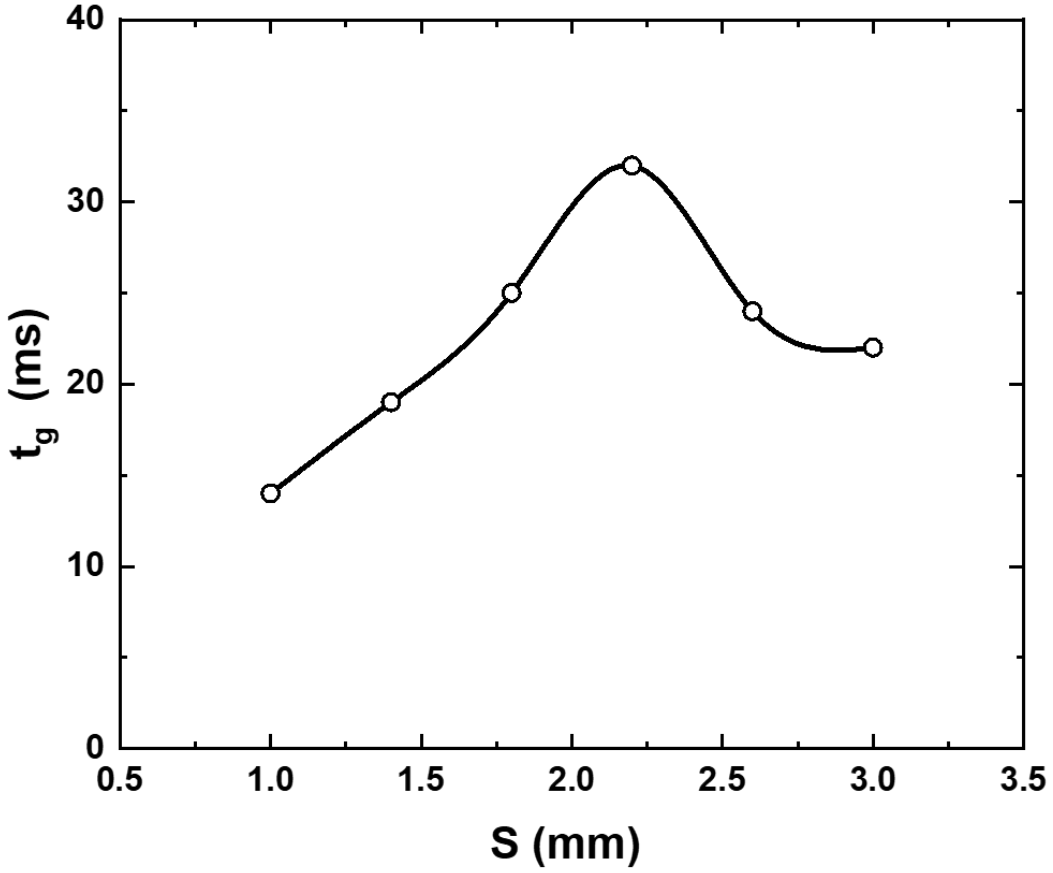

Fig. 3.9: Variation of bubble growth period with cavity spacing for a 1 mm thick stainless-steel substrate. ($q_{w,in}$ = 1.1 W/cm^2, ΔT_{nuc} = 6 °C, φ = 35°)

3.2.5 Bubble Departure Frequency

The bubble departure frequency is defined as the reciprocal of the total cycle duration (t_{cycle}), which is the sum of the growth period and the waiting time. Figure 3.10 shows the dependence of the total cycle time and bubble departure frequency on the cavity spacing, for a 1 mm thick stainless-steel substrate. The bubble departure frequency shows a non-monotonic relationship with cavity spacing. This is due to the non-monotonic variation of both the bubble growth period and the waiting time with cavity spacing. The smallest bubble departure frequency is observed for two

merging bubbles at a cavity spacing of S = 1.8 mm, and this is consistent with the fact that this specific spacing has the largest waiting time across the six spacings studied. Similarly, the bubble departure frequency is the largest for S = 1 mm, which corresponds to the smallest growth period and the smallest waiting time among the cavity spacings investigated in the present study. Thus, the bubble departure frequency decreases with decrease in cavity spacing from 3 mm to 1.8 mm, and increases with further decrease in spacing from 1.8 mm to 1 mm. Quantitatively, the bubble departure frequency observed for S = 1 mm is approximately 4 times that for S = 1.8 mm.

Figure 3.11 shows a comparison of the variation of bubble departure frequency with the cavity spacing predicted from the present simulations with the results reported for the experiments of Zhang and Shoji [23]. The imposed heat flux in the present simulations is 1.1 W/cm^2 while the heat flux in the experiments ranges from 2.2 to 3.7 W/cm^2. A 1 mm thick stainless-steel substrate is considered in the present simulations while a 0.2 mm thick silicon substrate was used in the experiments. To account for differences in the heat flux, substrate material, substrate thickness, and possibly in the cavity nucleation temperature between the present numerical simulations and the experiments of Zhang and Shoji [23], the bubble departure frequency is normalized with its maximum (f_{max}) and minimum (f_{min}) values in each study. The cavity spacing shown in the figure is the non-dimensional spacing S/D_b, where D_b is the departure diameter of a bubble that departs without merging. The difference between the two curves in Fig. 3.11 is primarily attributed to the significant variation in the waiting time with cavity spacing in the present simulations. In the range of heat fluxes for which Zhang and Shoji [23] conducted their experiments, they observed that there was almost no waiting time between the departure of a bubble and the nucleation of a new bubble at the site. As such, the bubble departure frequency in their experiments was governed by the growth period.

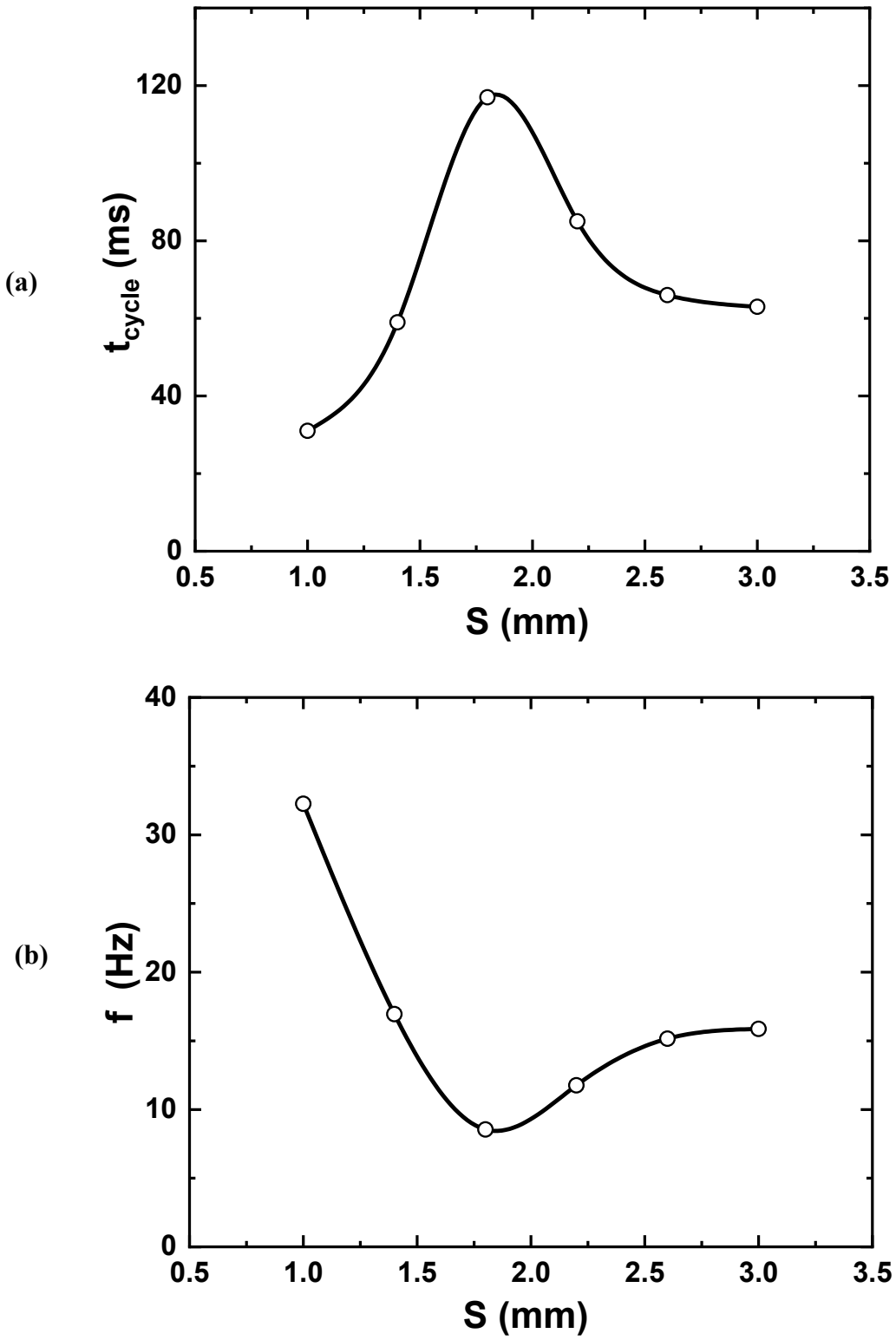

Fig. 3.10: Variation of (a) total cycle duration and (b) bubble departure frequency with cavity spacing for a 1 mm thick stainless-steel substrate. ($q_{w,in}$ = 1.1 W/cm^2, ΔT_{nuc} = 6 °C, φ = 35°)

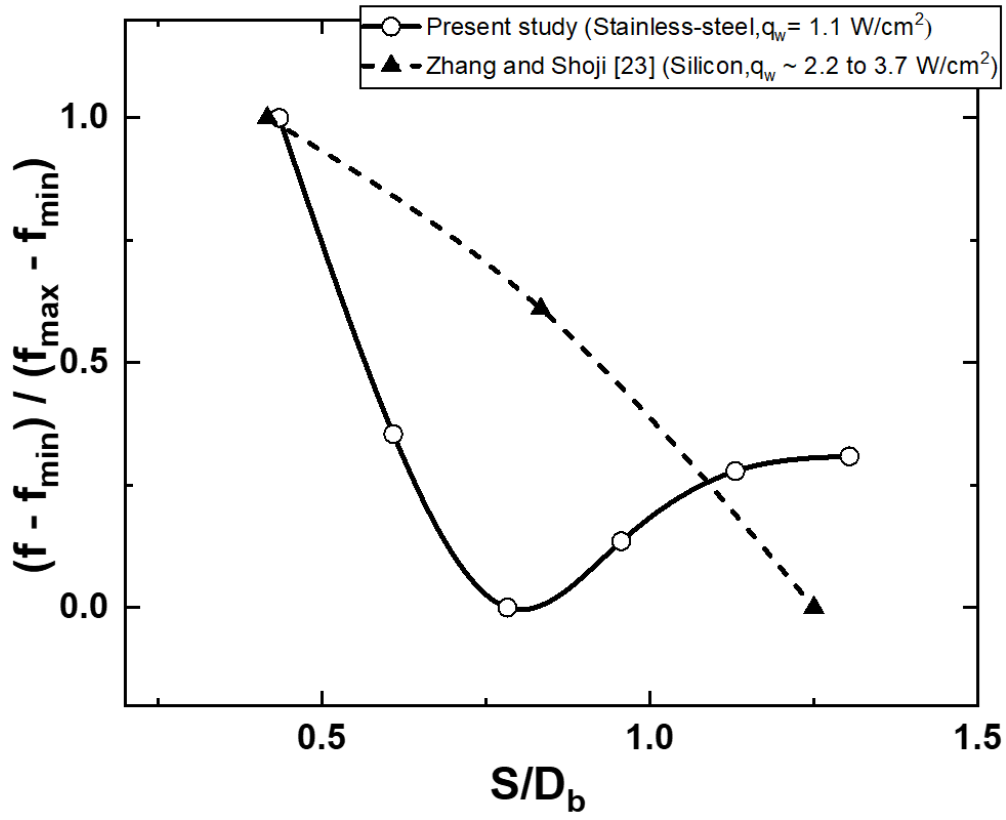

Fig. 3.11: Comparison of the variation of normalized bubble departure frequency with non-dimensional cavity spacing S/D_b obtained from present simulations and that reported in the experiments of Zhang and Shoji [23]. In the simulations, $q_{w,in}$ = 1.1 W/cm^2, ΔT_{nuc} = 6°C, φ = 35°.

3.2.6 Vapor Production Rate

The average vapor production rate over one complete bubble cycle ($\dot{V}_v$) is calculated from the equivalent bubble diameter based on total vapor volume at departure (D_d), the growth period (t_g) and waiting time (t_w) as shown below:

$$\dot{V}_v = \frac{\frac{\pi D_d^3}{6}}{t_g + t_w} \tag{3.1}$$

Figure 3.12 depicts the average vapor production rate over one bubble cycle as a function of cavity spacing. It is observed that the vapor production rates corresponding to cavity spacings without lateral bubble merger are higher compared to spacings at which bubble merger occurs. For cavity spacings of S = 1.4 mm and S = 1 mm, the smaller bubble size at departure leads to a lower vapor production rate compared to cases without bubble merger. The lowest vapor production rate is observed at a cavity spacing of S = 1.8 mm which has the smallest bubble departure frequency. The highest vapor production rate was observed for two non-merging bubbles at a cavity spacing of S = 3 mm, and it is about 4 times greater than the lowest vapor production rate, observed at a spacing of S = 1.8 mm.

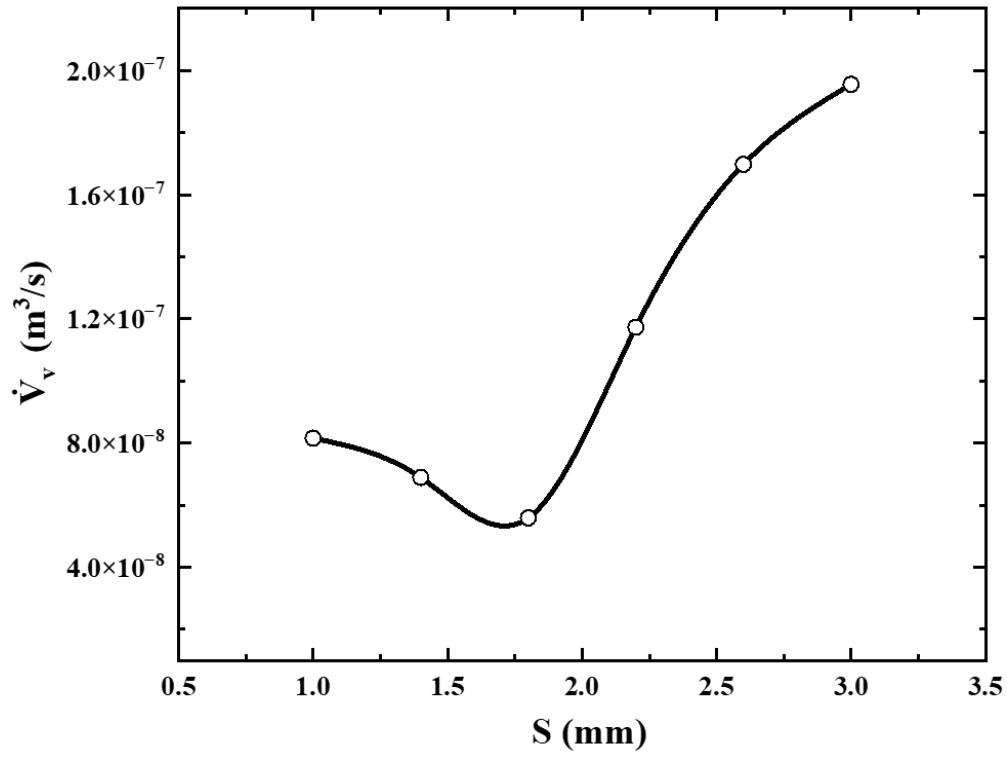

Fig. 3.12: Variation of average vapor production rate over one bubble cycle with cavity spacing for a 1 mm thick stainless-steel substrate. ($q_{w,in}$ = 1.1 W/cm^2, ΔT_{nuc} = 6 °C, φ = 35°)

3.2.7 Heat Transfer Coefficient

The average heat transfer coefficient ($\bar{h}$) over one complete bubble cycle is calculated from the average wall superheat ($\overline{\Delta T_w}$) and the imposed wall heat flux ($q_{w,in}$), as shown below:

$$\bar{h} = \frac{q_{w,in}}{\overline{\Delta T_w}} = \frac{q_{w,in}}{\left(\frac{1}{t_{cycle}\,A}\right)\int_{t=0}^{t=t_{cycle}}\int_{x=0}^{x=X}\int_{z=0}^{z=Z}\left[T_w(x,z,t) - T_{sat}\right]dx\,dz\,dt} \tag{3.2}$$

The average wall superheat ($\overline{\Delta T_w}$) is determined by averaging the wall superheat over the total cycle duration (t_{cycle}) and over the boiling surface area in the computational domain (A), which in the present study is 3.5 mm x 3.5 mm (with symmetry conditions). Since the imposed wall heat flux is the same for all the cavity spacings, the average heat transfer coefficient varies inversely with the average wall superheat.

Figure 3.13 depicts how the fractions of energy from the wall used for vapor production and for superheating of the liquid during one bubble cycle vary with cavity spacing. For the range of cavity spacings S = 1 mm to S = 1.8 mm, only up to 20 % of the total energy from the wall during one bubble cycle is utilized for vapor production. Consequently, the average wall superheat and in turn the average heat transfer coefficient over one bubble cycle, in this range of cavity spacings, are primarily dictated by the heat transfer to the liquid. When the cavity spacing increases from S = 1 mm to S = 1.8 mm, the bubbles grow progressively larger. This results in a corresponding increase in heat transfer to the liquid with increase in cavity spacing, through two mechanisms: (a) increased transient conduction to the liquid in area of bubble influence during the waiting time, and (b) increase in the bubble-induced convection heat transfer to the liquid outside the area of

bubble influence resulting from the increase in bubble size. This increase in heat transfer to the liquid, combined with the fact that the heat transfer to the liquid dictates the heat transfer coefficient for this range of spacings, explains the decrease in average wall superheat and increase in the average heat transfer coefficient as the cavity spacing increases from S = 1 mm to S = 1.8 mm, as shown in Figs. 3.14 and 3.15. As the cavity spacing is increased further from S = 1.8 mm to S = 3 mm, the fraction of energy from the wall that is utilized for vapor production increases up to about 50 %, resulting in a decrease in the average wall superheat, as shown in Fig. 3.14. As such, in the range of cavity spacings from S = 1.8 mm to S = 3 mm, the average heat transfer coefficient increases with an increase in cavity spacing, as observed in Fig. 3.15.

In summary, the average heat transfer coefficient increases with increase in cavity spacing. The higher average heat transfer coefficient in cases without lateral bubble merger compared to the cases with bubble merger is primarily attributed to the increase in average vapor production rate, and in turn the fraction of energy from the wall going towards vapor production in one bubble cycle. The average heat transfer coefficient for two non-merging bubbles at a cavity spacing of S = 3 mm is 15 % higher than that for two merging bubbles at a spacing of S = 1 mm.

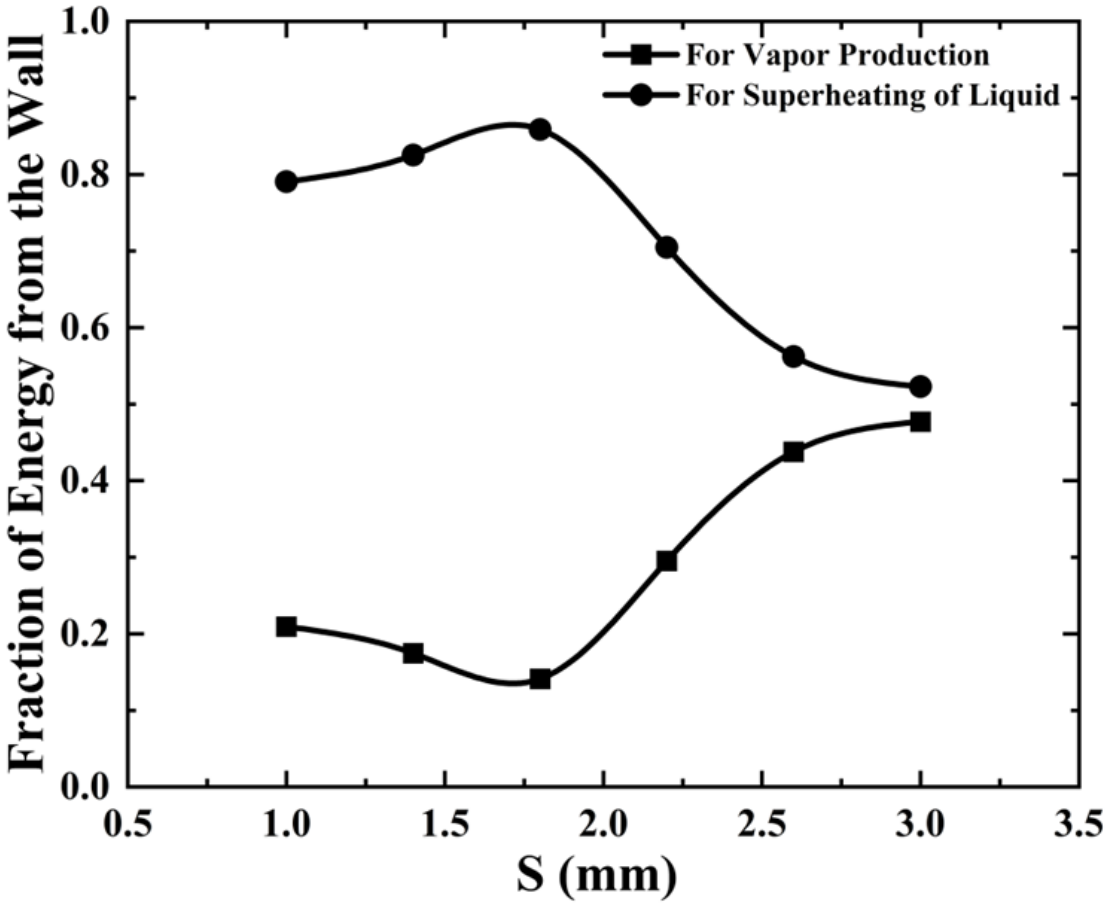

Fig. 3.13: Proportions of energy from the wall utilized for vapor production and for superheating of liquid as a function of cavity spacing for a 1 mm thick stainless-steel substrate. ($q_{w,in}$ = 1.1 W/cm^2, ΔT_{nuc} = 6 °C, φ = 35°)

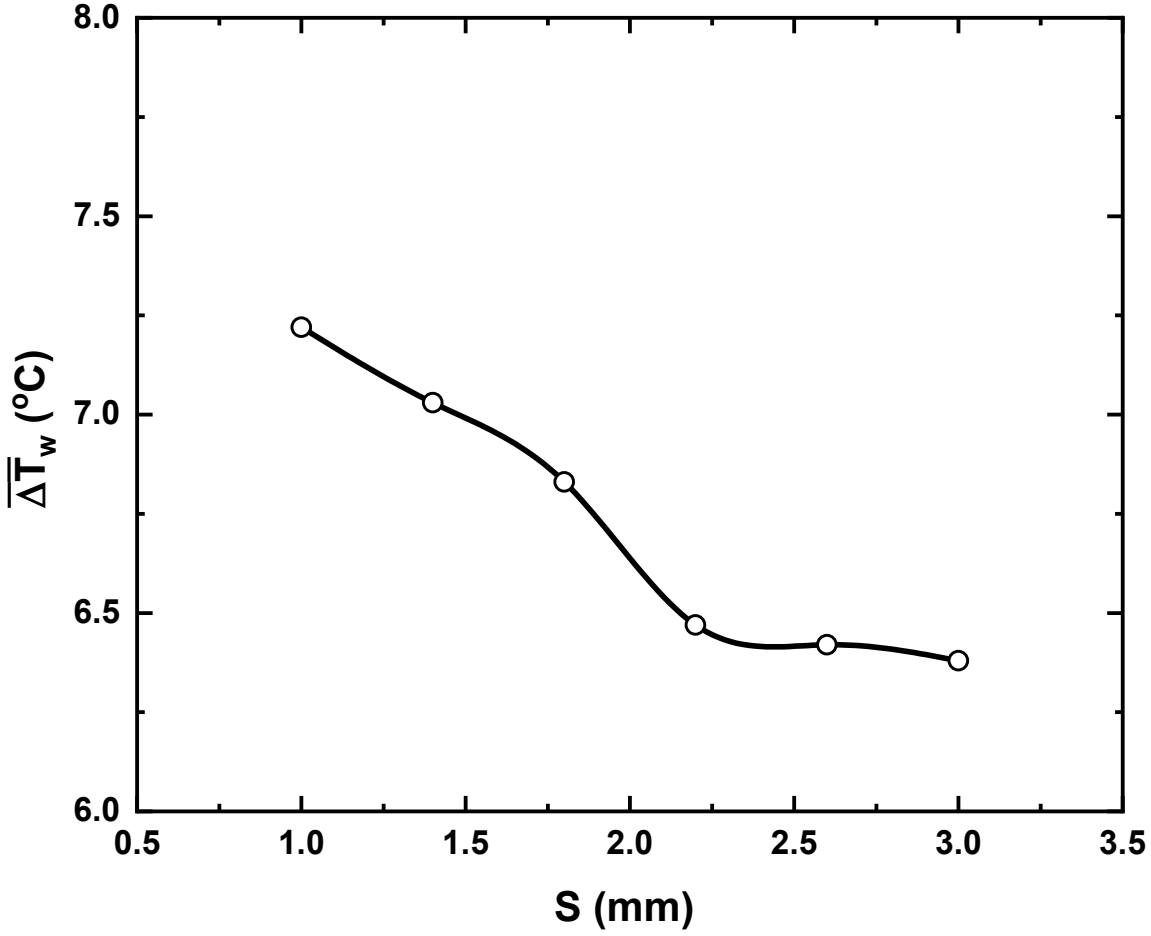

Fig. 3.14: Variation of average wall superheat over one bubble cycle with cavity spacing for a 1 mm thick stainless-steel substrate. ($q_{w,in}$ = 1.1 W/cm^2, ΔT_{nuc} = 6 °C, φ = 35°)

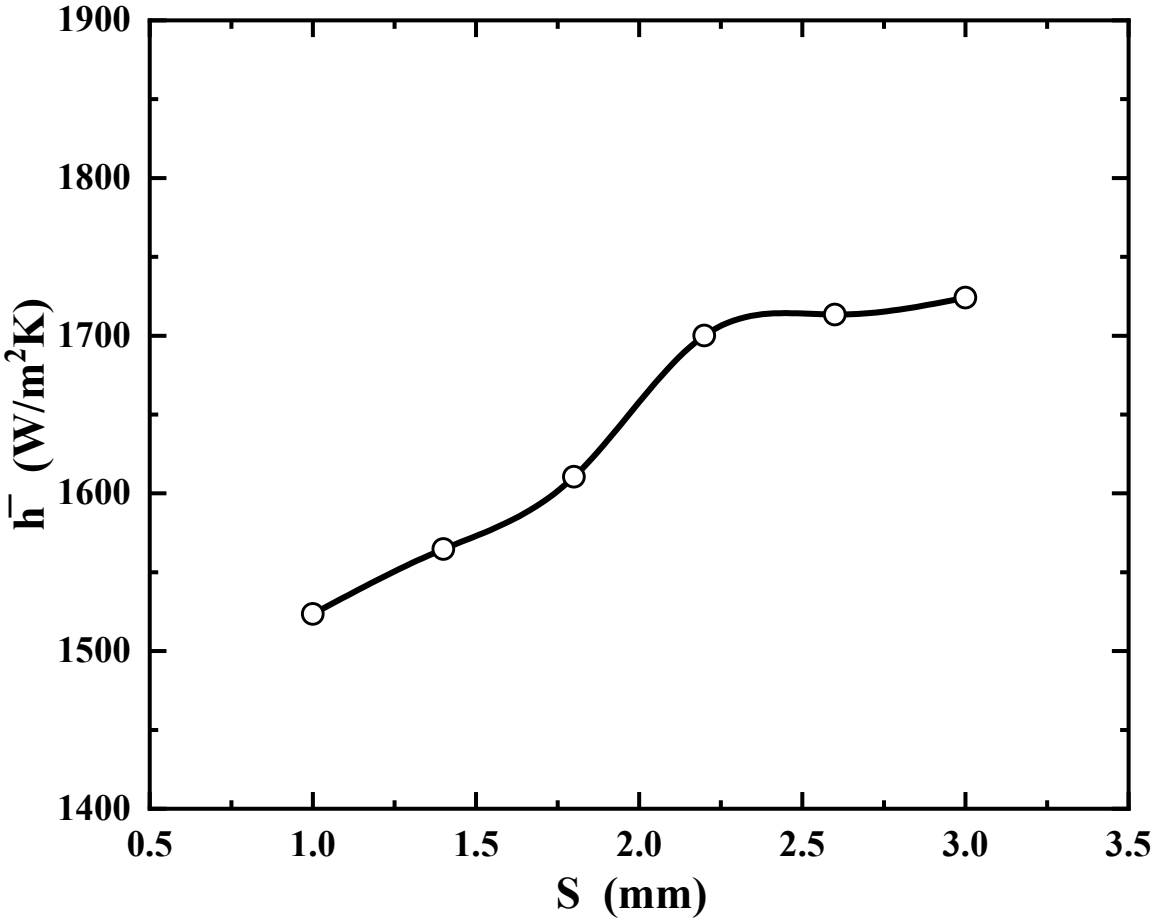

Fig. 3.15: Variation of average heat transfer coefficient over one bubble cycle with cavity spacing for a 1 mm thick stainless-steel substrate. ($q_{w,in}$ = 1.1 W/cm^2, ΔT_{nuc} = 6 ℃, φ = 35°)

The heat transfer coefficient in a conventional boiling curve increases from that in partial nucleate boiling, characterized by low wall heat flux and the departure of predominantly isolated bubbles from discrete nucleation sites without merging, to that in fully developed nucleate boiling, characterized by higher wall heat flux and higher prevalence of bubble merger. At first observation, such a trend may appear inconsistent with the findings of the present investigation, which indicate that lateral bubble merger tends to reduce the heat transfer coefficient. However, when considering

this discrepancy, it should be noted that the active nucleation site density is the same in all the cases in the present study. By contrast, in typical boiling surfaces for which boiling curves are obtained, the number density of active nucleation sites increases with increasing wall heat flux and wall superheat. It becomes challenging to ascertain whether the observed increase in heat transfer coefficient along the boiling curve with increasing heat flux is primarily attributable to the increased occurrence of bubble merger or to the increased density of active nucleation sites.

To examine the effect of increasing the number density of active nucleation sites on the heat transfer coefficient, numerical simulations are performed for nucleate boiling of saturated water on a 7 mm x 7 mm portion of a 1 mm thick stainless-steel substrate, this time with four identical nucleation sites. The four nucleation sites are located at the corners of a 3 mm × 3 mm square, as shown in Fig. 3.16. The imposed heat flux at the bottom face of the substrate and the cavity nucleation superheat are kept the same as those employed in the previous cases with two active nucleation sites. Table 3.1 presents the results, comparing the average heat transfer coefficient over one bubble cycle for two-site and four-site configurations on the same 7 mm × 7 mm area of the boiling surface, for a cavity spacing of S = 3 mm. The results indicate that, for identical cavity spacing, the heat transfer coefficient increases as the number density of active sites increases. This suggests that the observed increase in heat transfer coefficient from partial to fully developed nucleate boiling stems from the increased number density of active nucleation sites rather than from bubble merger itself.

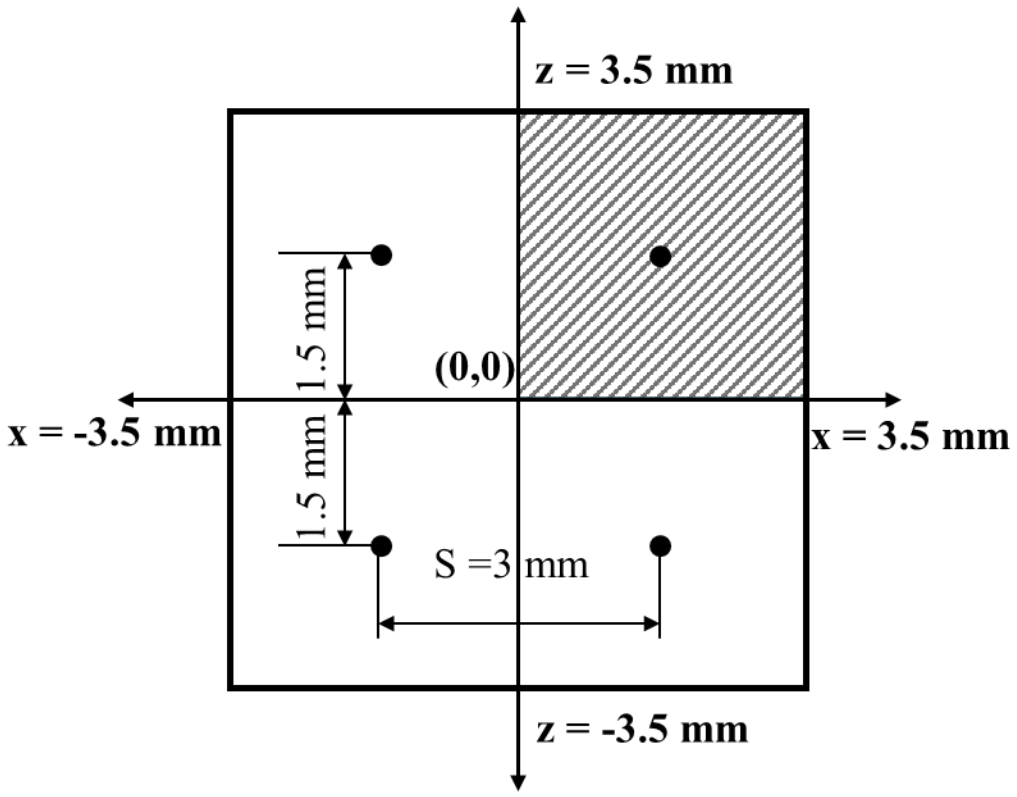

Fig. 3.16: Top view of the boiling surface showing the arrangement of four active nucleation sites on a 7 mm × 7 mm portion of a 1 mm thick stainless-steel substrate.

($q_{w,in}$ = 1.1 W/cm^2, ΔT_{nuc} = 6 °C, φ = 35°)

Cavity Configuration	$\bar{h}$ (W/m^{2}K)
Two cavities, S = 3 mm	1724
Four cavities arranged in a square, S = 3 mm	1850

Table 3.1: Average boiling heat transfer coefficient for two different cavity site configurations on a 1 mm thick stainless-steel substrate. ($q_{w,in}$= 1.1 W/cm^2; ΔT_{nuc} = 6 °C, φ = 35°)

The present investigation is predicated upon the assumption that the two adjacent active nucleation sites are identical and that the bubble nucleation and growth at the two sites are synchronous. It is recognized that on conventional boiling surfaces, nucleation sites of different sizes are generally randomly distributed across the surface, leading to non-synchronous bubble activity at two adjacent sites. This phase difference between the growth of bubbles at the adjacent sites would inherently result in variations in the dynamics of bubble merger and the associated heat transfer compared to those observed in the present work. The findings presented herein should therefore be interpreted as the outcomes of a numerical investigation conducted under a controlled, specific condition, aimed at providing a deeper insight into the influence of lateral bubble merger on key nucleate pool boiling characteristics — namely waiting time, bubble departure frequency and heat transfer coefficient — under a constant imposed heat flux. Nevertheless, the results of the present study can be confidently extended to future research, and provide a framework for practical scenarios, including the design and optimization of engineered heat transfer surfaces with precisely controlled nucleation site configurations.

The results discussed in this chapter focus on the influence of cavity spacing and lateral bubble merger on key nucleate boiling bubble dynamics and heat transfer parameters, as the cavity spacing between two adjacent active nucleation sites is varied, for a 1 mm thick stainless-steel substrate. Due to the coupling between the transient conduction in the solid substrate and the heat transfer on the fluid-side, the thermal properties and thickness of the substrate are also expected to influence the bubble dynamics and heat transfer during the boiling process considered in this study. A detailed discussion of this influence is presented in the next chapter.

Chapter 4

Effect of Substrate Thermal Properties and Thickness

The present chapter provides a detailed discussion on the dependence of nucleate pool boiling bubble dynamics and heat transfer on substrate thermal properties and thickness, for a horizontal substrate with two adjacent active cavity sites, along with insights on whether lateral bubble merger changes this dependence in any way.

4.1 Study Parameters

Numerical simulations are performed for saturated pool boiling of water at atmospheric pressure on a $7\ \text{mm} \times 7\ \text{mm}$ portion of copper, stainless-steel and glass substrates with two adjacent active nucleation sites. The substrate thickness (L) is parametrically varied from 0.25 mm to 2.5 mm. For each combination of substrate material and thickness, two different cavity spacings of 1.4 mm and 3 mm are considered. A cavity nucleation superheat of 6 ºC is considered, and a constant heat flux of 1.1 W/cm^2 is imposed at the bottom face of the substrate for all the simulations in this study, representing conditions during boiling inception. A static contact angle of 35° was chosen for all the simulations in the present study.

Table 4.1 shows the relevant thermophysical properties of copper, steel and glass. The thermal diffusivity (α) of copper is about two orders of magnitude greater than that of glass.

Thermal property	Copper	Steel	Glass
$\boldsymbol{k}$ (W/m^{2}K)	401	15	1.09
$\boldsymbol{\rho c}$ (J/m^{3}K)	3.44 x 10^6	3.77 x 10^6	2.14 x 10^6
$\boldsymbol{\alpha}$ (m^2/s)	117 x 10^{-6}	3.9 x 10^{-6}	0.51 x 10^{-6}

Table 4.1: Thermal conductivity (k), volumetric heat capacity (ρc) and thermal diffusivity (α) of copper, stainless-steel and glass.

4.2 Results and Discussion

4.2.1 Waiting Time

Figure 4.1 shows the variation of waiting time with substrate material properties and thickness for cavity spacings of S = 1.4 mm and S = 3 mm. For both cavity spacings, the waiting time shows a similar dependence on substrate material properties and thickness. The difference observed in the particular values of waiting time at these two cavity spacings, for a given substrate material and thickness, is due to the corresponding difference in the extent of the boiling surface experiencing a temperature deficit relative to the nucleation temperature, caused by the heat transfer during bubble growth, as explained in the previous chapter.

The waiting time is found to decrease with an increase in the thermal diffusivity of the substrate, for both cavity spacings. This follows from the fact that the boiling surface temperature recovers at a faster rate with higher thermal diffusivity of the substrate material. For a given substrate material, the waiting time decreases with increase in substrate thickness from 0.25 mm to 1.25 mm, beyond which the waiting time shows negligible change. This is attributed to an increase in the thermal mass of the substrate with increasing thickness. The temperature contours in steel substrate

of thicknesses L = 0.25 mm and L = 1 mm just after bubble departure are shown in Fig. 4.2. In this figure, the presence of larger thermal mass is seen in the thicker substrate, below the region of bubble influence characterized by higher temperature gradients. This larger thermal mass results in a smaller drop in the substrate temperature in the region of bubble influence and a higher local heat flux in this region post bubble departure. This is inferred from Fig. 4.3, which presents the spatial distribution of local substrate temperature and heat flux at a depth of 0.2 mm from the boiling surface for L = 0.25 mm and L = 1 mm thick steel substrates. For substrate thickness greater than 1.25 mm, the decrease in waiting time with increase in thickness is insignificant. This is because of the reason that beyond this thickness any further increase in the substrate thermal mass does not result in a significant improvement in the recovery rate of substrate temperature in the region of bubble influence.

For both cavity spacings, the thermal properties of the substrate have a stronger influence on the waiting time as compared to that of the substrate thickness. The waiting time for copper substrate is up to 90 % smaller than that for glass whereas the reduction in waiting time with increasing substrate thickness is less than 23 % for the three substrate materials, for both the cavity spacings.

(a)

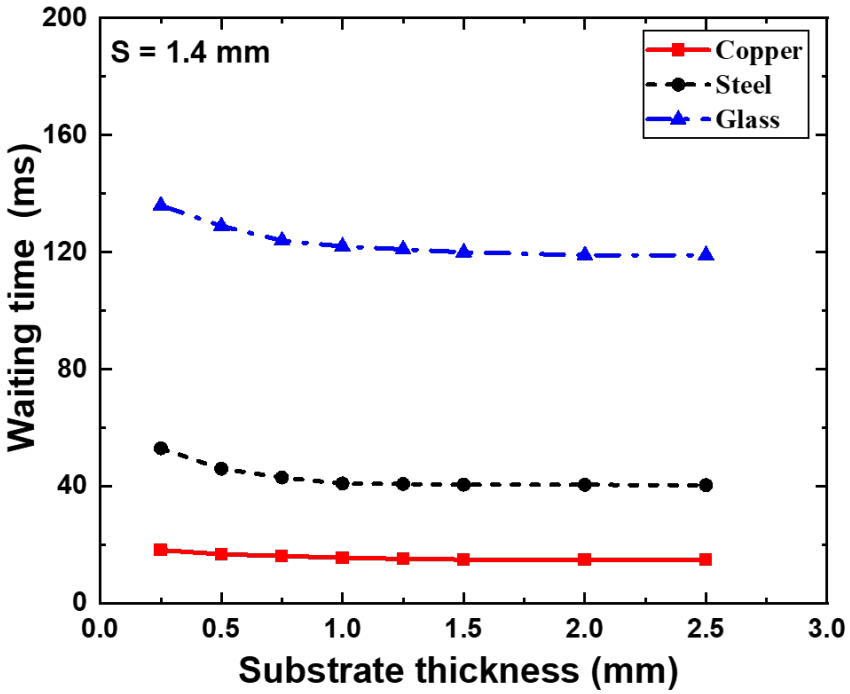

(b)

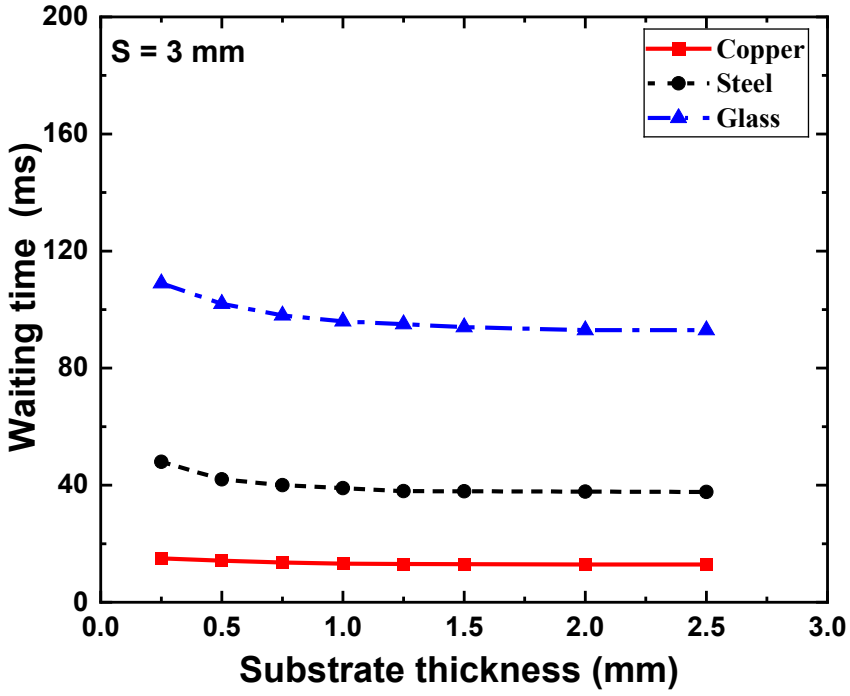

Fig. 4.1: Variation of waiting time with substrate material and thickness for cavity spacings of (a) S = 1.4 mm and (b) S = 3 mm. $q_{w,in}$ = 1.1 W/cm^2, ΔT_{nuc} = 6 °C, φ = 35°.

(a)

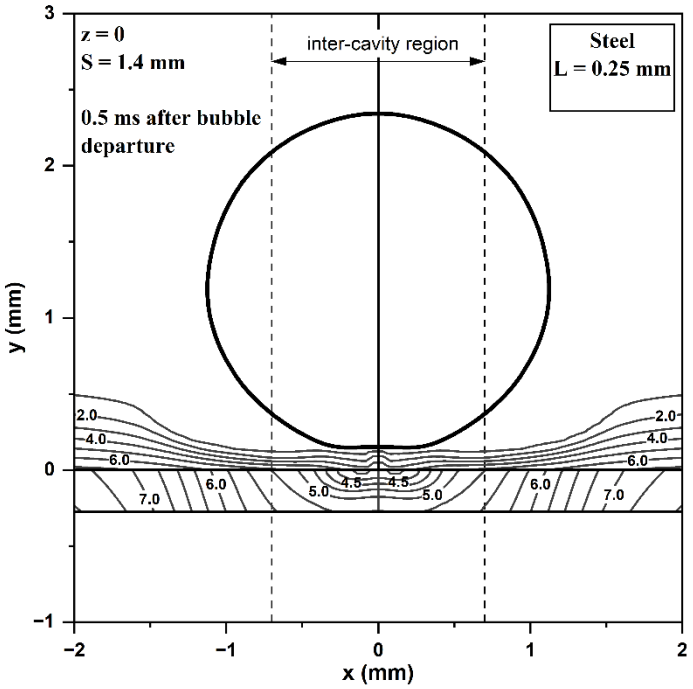

(b)

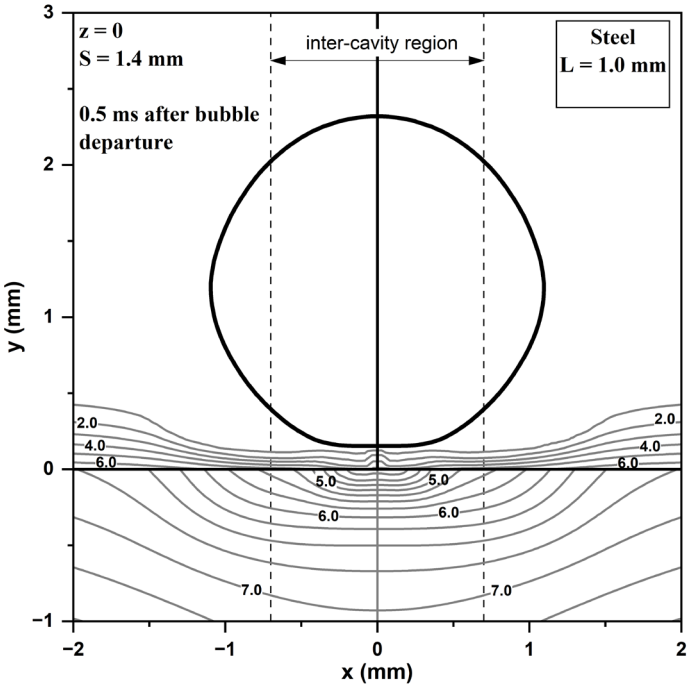

Fig. 4.2: Temperature contours ($T - T_{sat}$) in solid substrate and liquid 0.5 ms after bubble departure at z = 0 for (a) 0.25 mm and (b) 1.0 mm thick steel substrates with cavity spacing S = 1.4 mm. Temperature increments are 1.0 ℃ in the liquid and 0.25 ℃ in the solid. $q_{w,in}$ = 1.1 W/cm^2, ΔT_{nuc} = 6 ℃, φ = 35°.

(a)

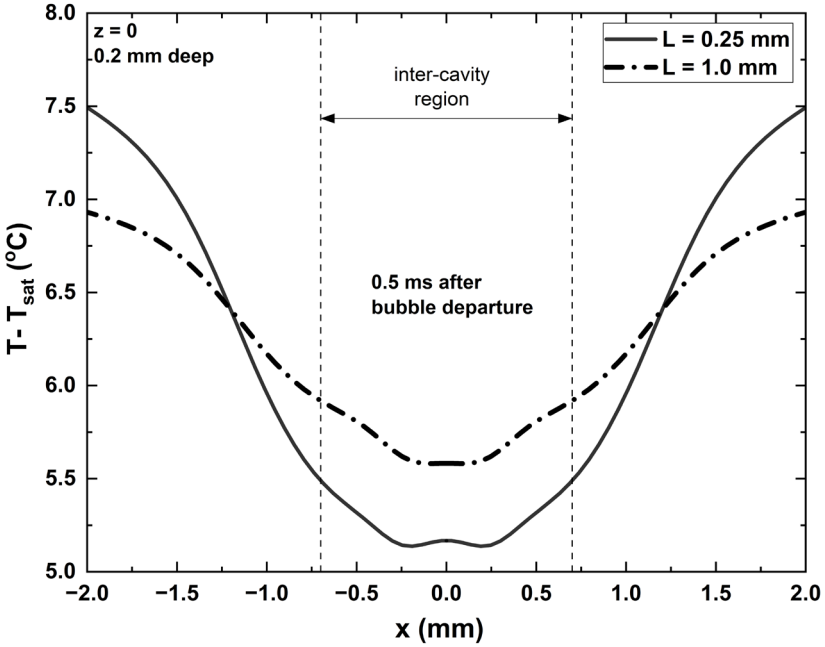

(b)

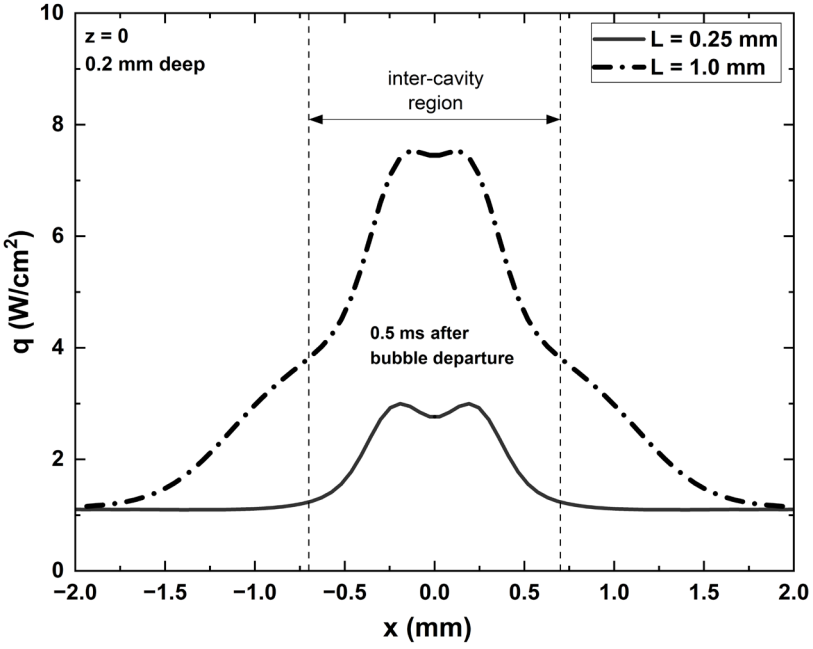

Fig. 4.3: Spatial distribution of (a) temperature and (b) vertical heat flux at z = 0 at a depth of 0.2 mm for 0.25 mm and 1.0 mm thick stainless-steel substrates with cavity spacing S = 1.4 mm about 0.5 ms after bubble departure. $q_{w,in}$ = 1.1 W/cm^2, ΔT_{nuc} = 6 °C, φ = 35°.

4.2.2 Bubble Growth Rate

The bubble growth rate (dD/dt) for different substrate materials of thickness 0.25 mm, for cavity spacings S = 1.4 mm and S = 3 mm, is shown in Fig. 4.4(a). The diameter D is based on the total volume of the two bubbles. A zoomed portion of the figure during the first 2 ms of bubble growth is shown for better clarity (Fig. 4.4(b)). For both cavity spacings, the bubble growth rate is seen to decrease with an increase in the thermal diffusivity of the substrate.

Figure 4.5(a) shows the bubble growth rate for glass substrates of two different thicknesses, for cavity spacings S = 1.4 mm and S = 3 mm, with a zoomed-in version for the first 2 ms shown in Fig. 4.5 (b). The diameter D is based on the total vapor volume attached to the wall. From Fig. 4.5(b), the bubble growth rate in the initial stage is found to decrease with increasing thickness of the glass substrate, for both cavity spacings. Overall, it is seen that the thermal material properties and thickness of the substrate have a minor effect on the bubble growth rate. The explanations for the variations in the growth rates with substrate thermal properties and thickness, as observed in Figs. 4.4(b) and 4.5(b), are given below.

Figure 4.6 shows the spatial distribution of the boiling surface temperature 0.5 ms before bubble nucleation for 0.25 mm thick copper, steel and glass substrates, for cavity spacings S = 1.4 mm and S = 3 mm. For cavity spacing of S = 1.4 mm, as observed in Fig. 4.6(a), the boiling surface temperature in the inter-cavity region just before bubble nucleation increases with increasing substrate thermal diffusivity while the opposite is true outside the inter-cavity region. The combined effect of these variations in boiling surface temperature is a decrease in the initial bubble growth rate with increasing thermal diffusivity for S = 1.4 mm, as seen in Fig. 4.4(b). In Fig. 4.6(b),

for cavity spacing of S = 3 mm, the temperature of the boiling surface in the vicinity of the cavity sites decreases with increase in the thermal diffusivity of the substrate, leading to a corresponding decrease in bubble growth rate.

Figure 4.7 shows the boiling surface temperature distribution 0.5 ms before bubble nucleation for 0.25 mm and 1 mm thick glass substrates, with cavity spacings S = 1.4 mm and S = 3 mm. Again, due to the variation in the temperature distribution of the boiling surface in the vicinity of the cavity sites with substrate thickness, the initial bubble growth decreases with increasing substrate thickness, for both cavity spacings (Fig. 4.5(b)).

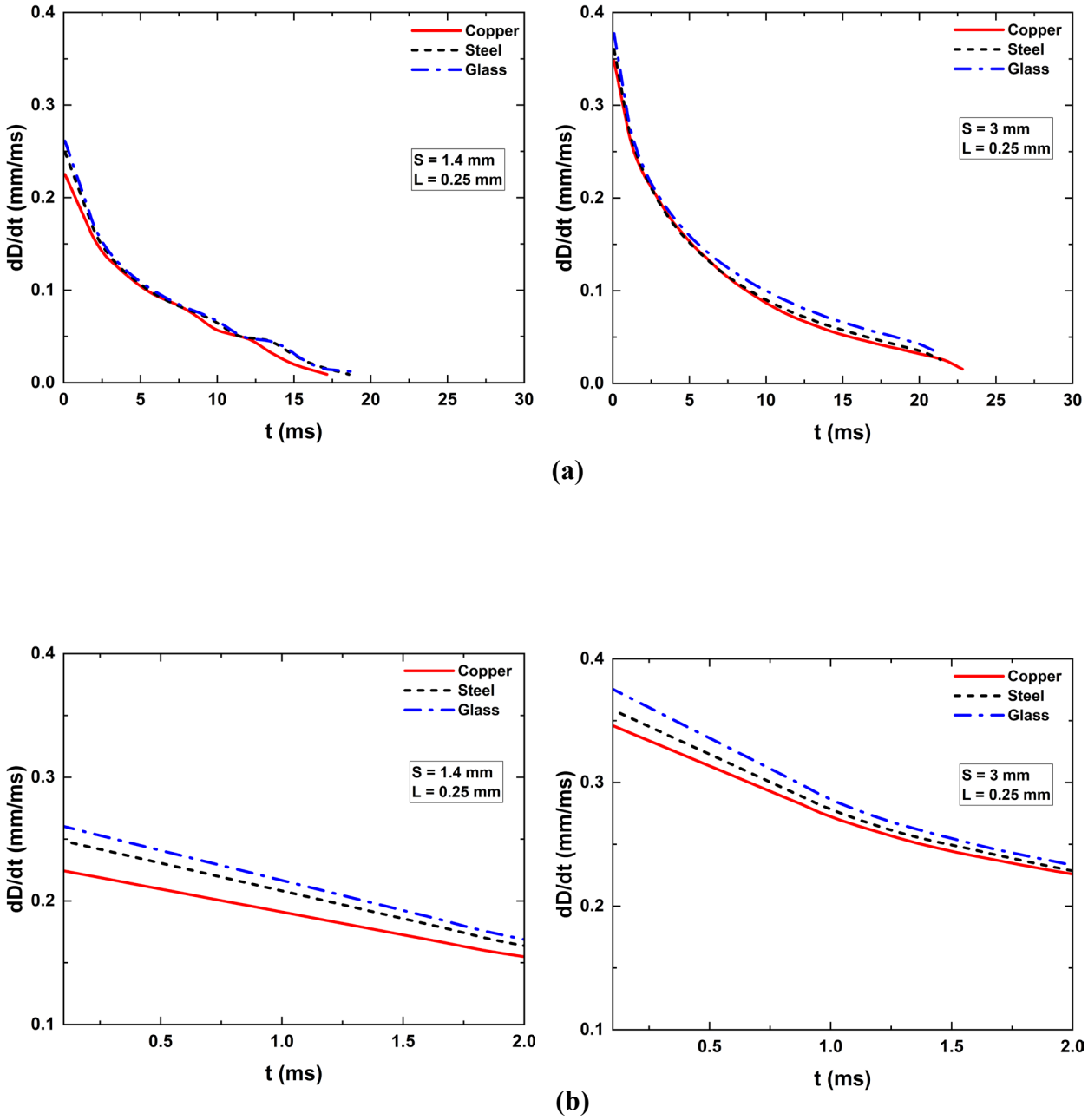

Fig. 4.4: (a) Bubble growth rate (dD/dt) during the growth period and (b) a zoomed-in version for the first 2 ms, for three different substrate materials of thickness L = 0.25 mm with cavity spacings S = 1.4 mm and S = 3 mm. $q_{w,in}$ = 1.1 W/cm^2, ΔT_{nuc} = 6 °C, φ = 35°.

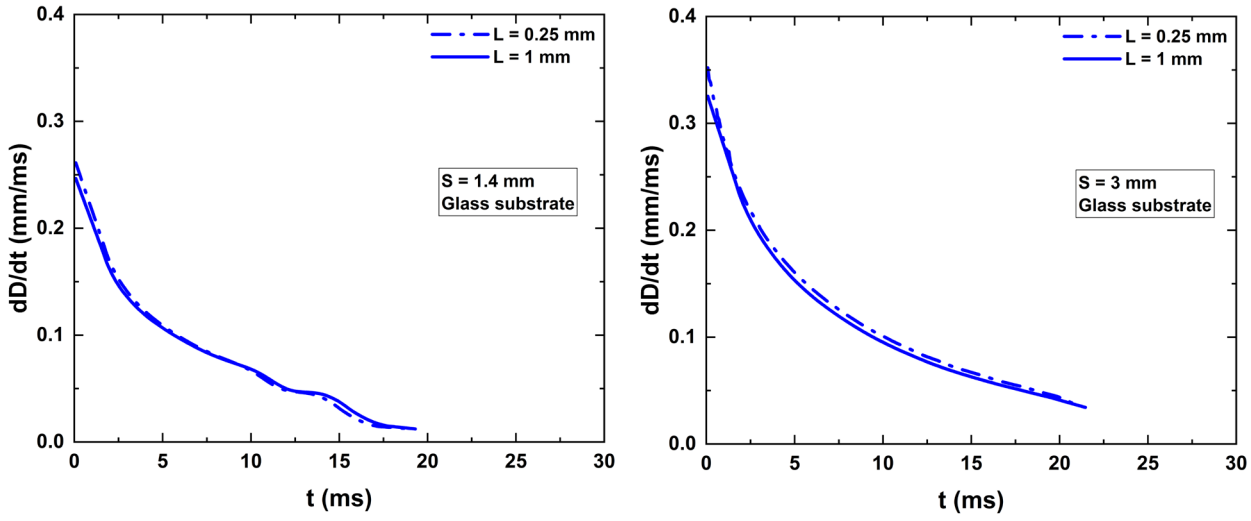

(a)

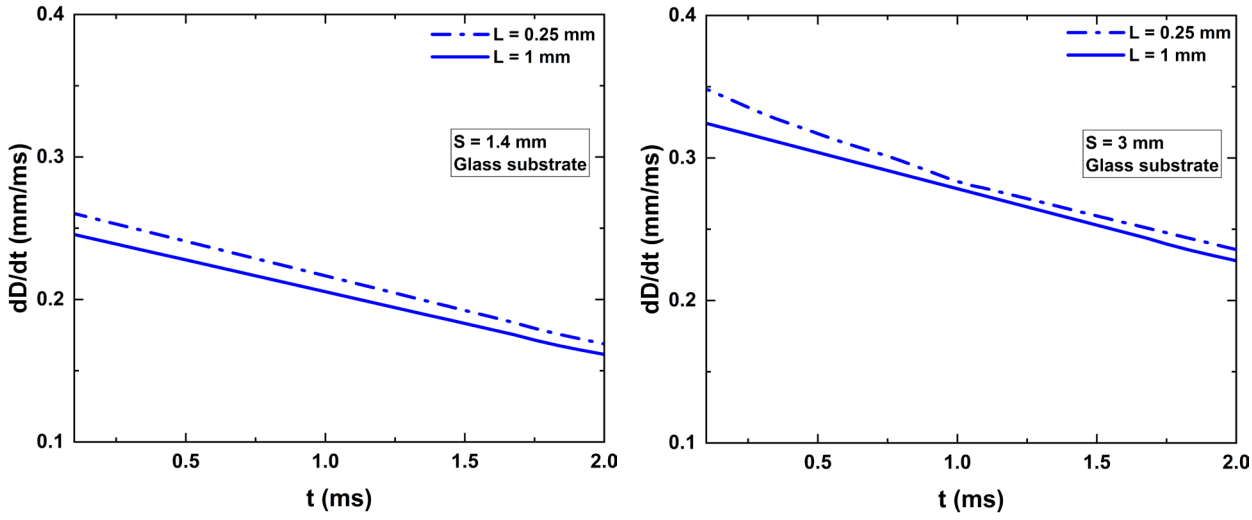

(b)

Fig. 4.5: (a) Bubble growth rate (dD/dt) during the growth period and (b) a zoomed-in version for the first 2 ms, for glass substrates of thicknesses L = 0.25 mm and L = 1 mm, with cavity spacings S = 1.4 mm and S = 3 mm.$q_{w,in}$ = 1.1 W/cm^2, ΔT_{nuc} = 6 ℃, φ = 35°.

(a)

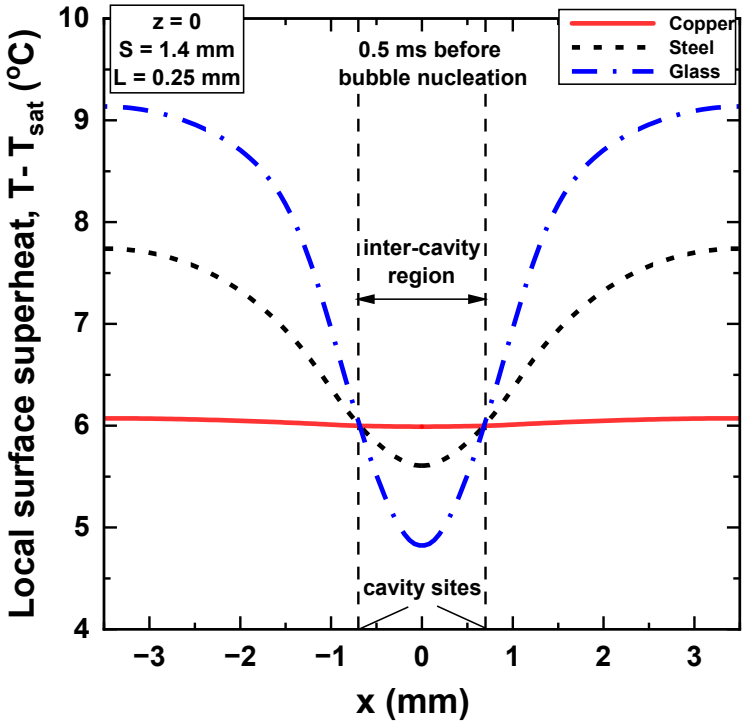

(b)

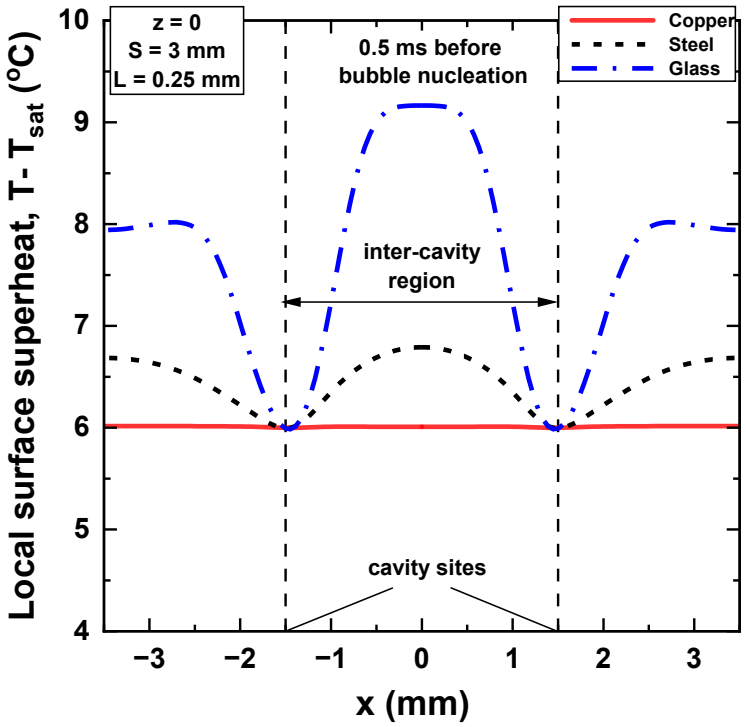

Fig. 4.6: Spatial distribution of boiling surface temperature 0.5 ms before bubble nucleation for different substrate materials of thickness L = 0.25 mm with cavity spacings of (a) S = 1.4 mm and (b) S = 3 mm. $q_{w,in}$ = 1.1 W/cm^2, ΔT_{nuc} = 6 °C, φ = 35°.

(a)

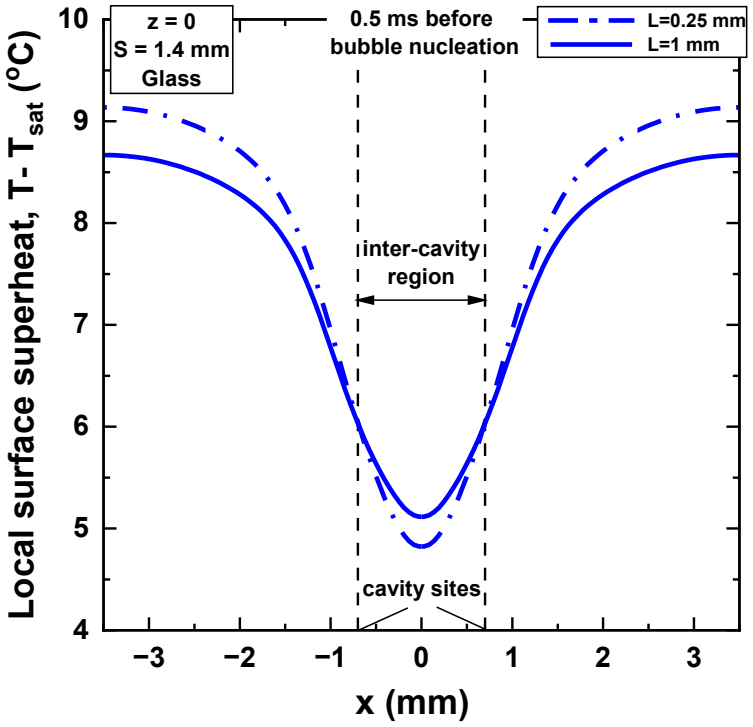

(b)

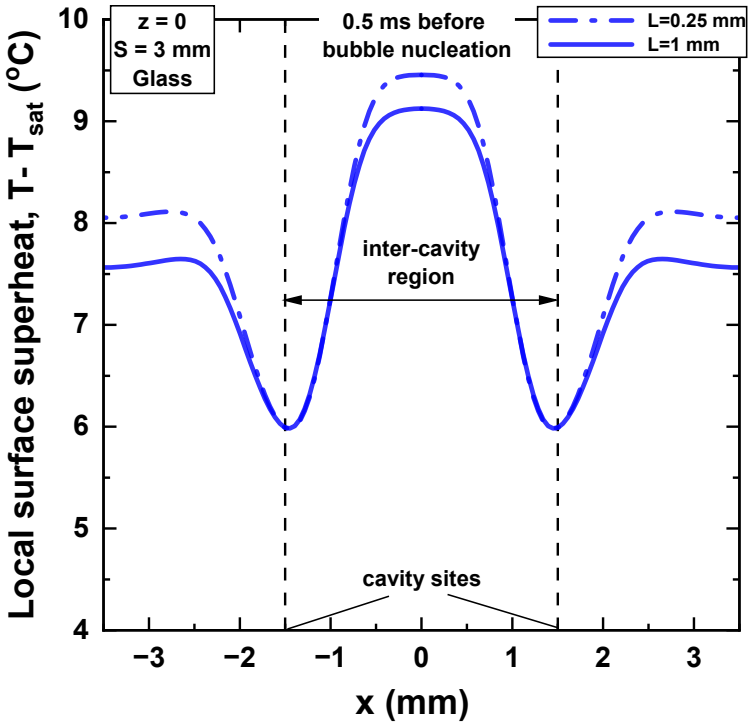

Fig. 4.7: Spatial distribution of boiling surface temperature 0.5 ms before bubble nucleation for glass substrates of thicknesses L = 0.25 mm and L = 1 mm with cavity spacings of (a) S = 1.4 mm and (b) S = 3 mm. $q_{w,in}$ = 1.1 W/cm^2, ΔT_{nuc} = 6 °C, φ = 35°.

4.2.3 Bubble Departure Diameter and Bubble Growth Period

The variation of bubble departure diameter with substrate material and thickness, for cavity spacings of S = 1.4 mm and S = 3 mm, is shown in Fig. 4.8. For both cavity spacings, the bubble departure diameter decreases with increasing substrate thermal diffusivity and with increasing substrate thickness for a given substrate material. This is attributed to the decrease in the initial bubble growth rate with increasing thermal diffusivity, and with increasing substrate thickness, as discussed in Section 4.2.2. This is consistent with the findings of Son et al. [27] in their numerical and experimental investigation of single bubble pool boiling. They found that a slower bubble growth rate (caused by a lower wall superheat) led to a smaller bubble departure diameter because of reduced inertia.

In the present study, the bubble departure diameter for copper is up to 8 % smaller than that for glass, for both cavity spacings, while it decreases by less than 1 % with increasing substrate thickness for all substrate materials in this study. This shows that the substrate material properties have a relatively stronger influence on the bubble departure diameter compared to the substrate thickness for a given material.

(a)

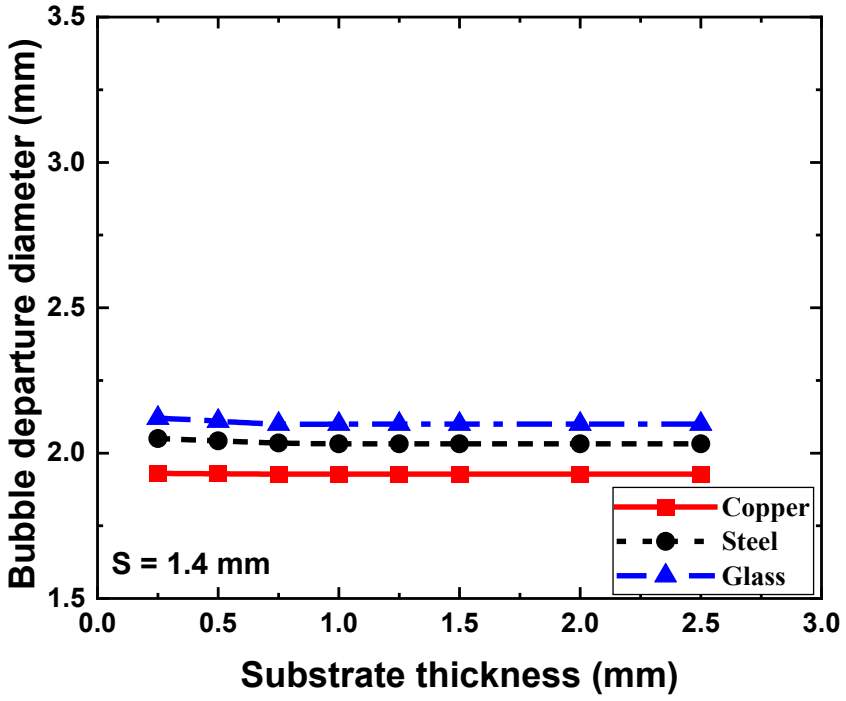

(b)

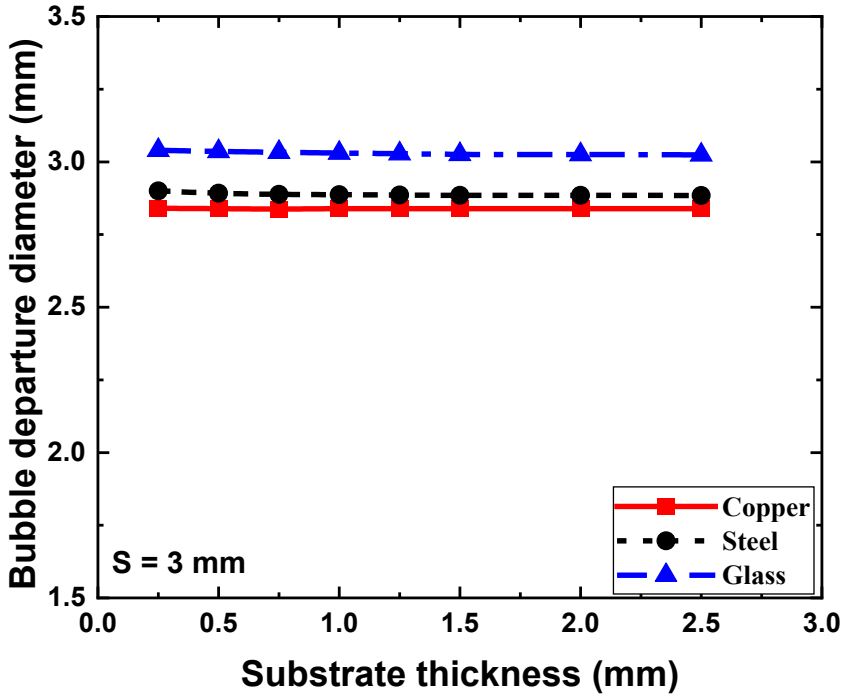

Fig. 4.8: Variation of bubble departure diameter based on total vapor volume with substrate material and thickness for cavity spacings (a) S = 1.4 mm and (b) S = 3 mm. $q_{w,in}$ = 1.1 W/cm^2, ΔT_{nuc} = 6 °C, φ = 35°.

Figure 4.9 presents the variation of bubble growth period for different substrate materials and thicknesses, corresponding to cavity spacings S = 1.4 mm and S = 3 mm. For the case without lateral bubble merger (S = 3 mm), it is seen in Fig. 4.9(b) that the bubble growth period increases with increasing substrate thermal diffusivity, and this is due to the decrease in bubble growth rate (Fig. 4.4(b)). On the other hand, for the case with lateral bubble merger (S = 1.4 mm), the bubble growth period decreases with increase in substrate thermal diffusivity, as seen in Fig. 4.9(a), despite the decrease in initial bubble growth rate shown in Fig. 4.4(b). This is because the bubbles from the two adjacent cavity sites merge earlier as the thermal diffusivity of the substrate increases, despite fixed cavity spacing. Earlier merger of bubbles causes the bubble to depart relatively sooner since the additional lift force caused by bubble merger also comes into effect sooner. The reason behind the earlier merger of bubbles from the two cavity sites with increasing substrate thermal diffusivity is described below.

Figure 4.10 shows a comparison of bubble merger process for 0.25 mm thick copper and glass substrates with cavity spacing S = 1.4 mm. The bubbles on the copper substrate are seen to merge earlier and at smaller size as compared to the bubbles on the glass substrate. This earlier bubble merger for copper substrate is due to the faster growth rate of the portion of the bubbles in the inter-cavity region for the copper substrate relative to that for glass substrate, as shown in Fig. 4.10. It is also observed that for the copper substrate, the portions of the bubbles in the inter-cavity region and outside this region grow at almost the same rate, whereas for the glass substrate, the portion of the bubbles in the inter-cavity region grows at a slower rate than that outside this region. This difference in bubble growth rates in the inter-cavity region between the two substrate materials as well as the difference in bubble growth rates between the inter-cavity region and outside this region

on the glass substrate are explained by the spatial distribution of the boiling surface temperature on the copper and glass substrates just before bubble nucleation, as shown in Fig. 4.6(a). In the inter-cavity region, the boiling surface temperature for the copper substrate is seen to be higher than that for the glass substrate. It is also observed in Fig. 4.6(a) that the temperature of the boiling surface for the copper substrate is nearly uniform over the entire boiling surface, whereas for the glass substrate, there is a clear difference between the boiling surface temperatures in the inter-cavity region and outside this region.

Quantitatively, the bubble growth period for copper is about 9 % smaller than that for glass, for the cases with lateral bubble merger (S = 1.4 mm) whereas for cases without bubble merger (S = 3 mm), the growth period for copper is about 9 % larger than that for glass.

The bubble growth period increases slightly with increase in substrate thickness, as seen in Fig. 4.9. This is due to the decrease in bubble growth rate with increasing substrate thickness (Fig. 4.5). The bubble growth period increases by less than 2 % with increasing thickness for all the substrate materials considered in this study, indicating that the substrate thickness has a relatively weaker influence on the growth period compared to that of the substrate thermal properties.

For a given substrate material and thickness, the bubble departure diameter and growth period for S = 1.4 mm are smaller than the corresponding values for S = 3 mm, as observed in Fig. 4.8 and Fig. 4.9 respectively. This reduction in both bubble departure diameter and growth period for S = 1.4 mm is attributed to the additional upward force (lift) on the bubble due to the liquid flow created by lateral bubble merger, as discussed in Chapter 3.

(a)

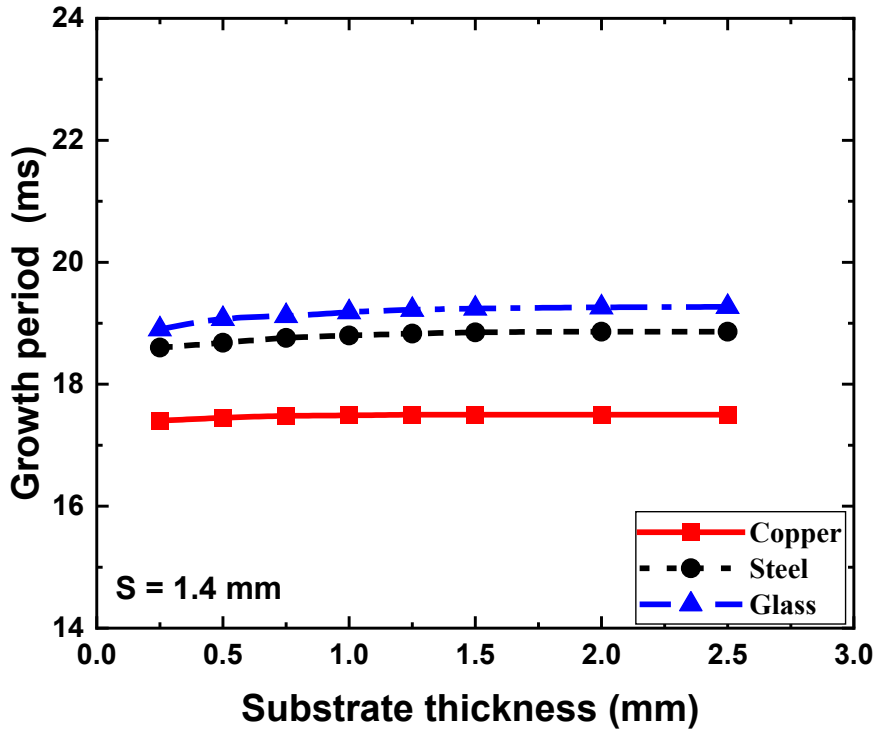

(b)

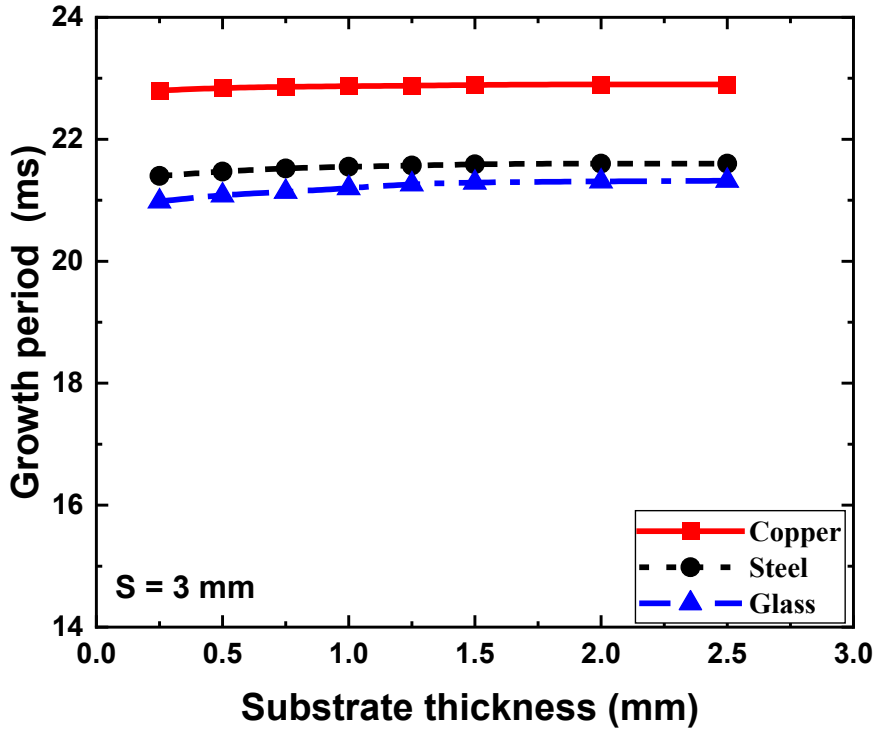

Fig. 4.9: Variation of bubble growth period with substrate material and thickness for cavity spacings of (a) S = 1.4 mm and (b) S = 3 mm. $q_{w,in}$ = 1.1 W/cm^2, ΔT_{nuc} = 6 °C, φ = 35°.

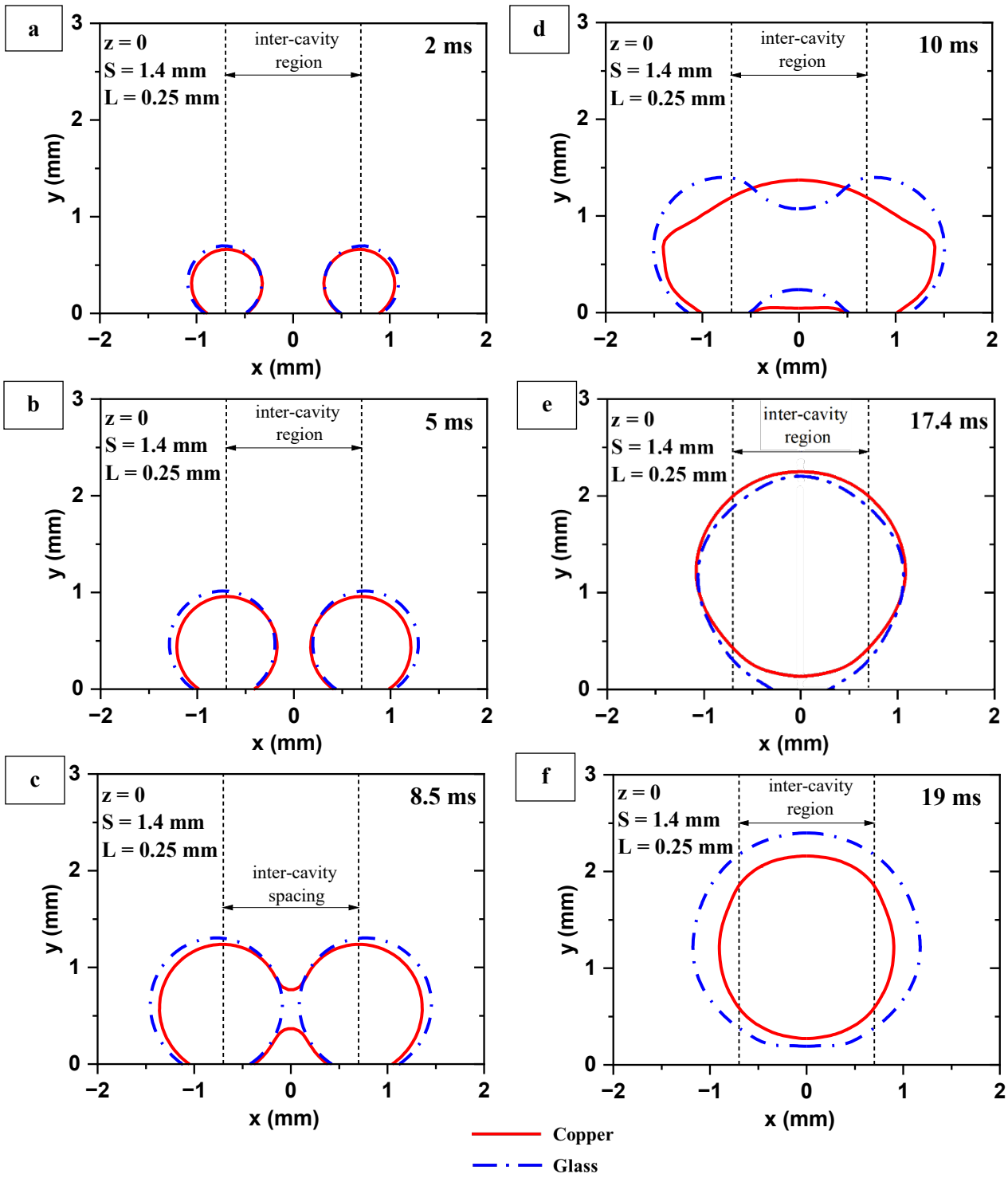

Fig. 4.10: Bubble shapes at z = 0 at different time instances (a) to (f) during bubble growth period for 0.25 mm thick copper and glass substrates with cavity spacing S = 1.4 mm. $q_{w,in}$ = 1.1 W/cm^2, ΔT_{nuc} = 6 °C, φ = 35°.

4.2.4 Bubble Departure Frequency

Figure 4.11 shows the bubble departure frequency as a function of the substrate thickness for three different substrate materials with cavity spacings S = 1.4 mm and S = 3 mm. The bubble departure frequency is the reciprocal of the sum of the bubble growth and waiting periods, $(t_g + t_w)^{-1}$. For the cases with and without bubble merger, the bubble departure frequency is seen to clearly increase with increase in substrate thermal diffusivity. For a given material, the bubble departure frequency increases with increase in substrate thickness but in general the influence of substrate thickness on the departure frequency is much weaker than that of the substrate thermal diffusivity. The main contribution to the variation in the bubble departure frequency with substrate material and thickness is the corresponding variation in waiting time. This follows from the fact that the waiting time shows a stronger dependence on the substrate material properties and thickness as compared to the growth period, as evidenced by the quantitative descriptions of the variation in waiting time and bubble growth period earlier in this chapter.

Quantitatively, the bubble departure frequency for copper is greater than that for glass by up to 420 % for S = 1.4 mm and up to 250 % for S = 3 mm. The increase in the departure frequency with substrate thickness is less than 20 % for the range of thicknesses considered for the three substrate materials.

(a)

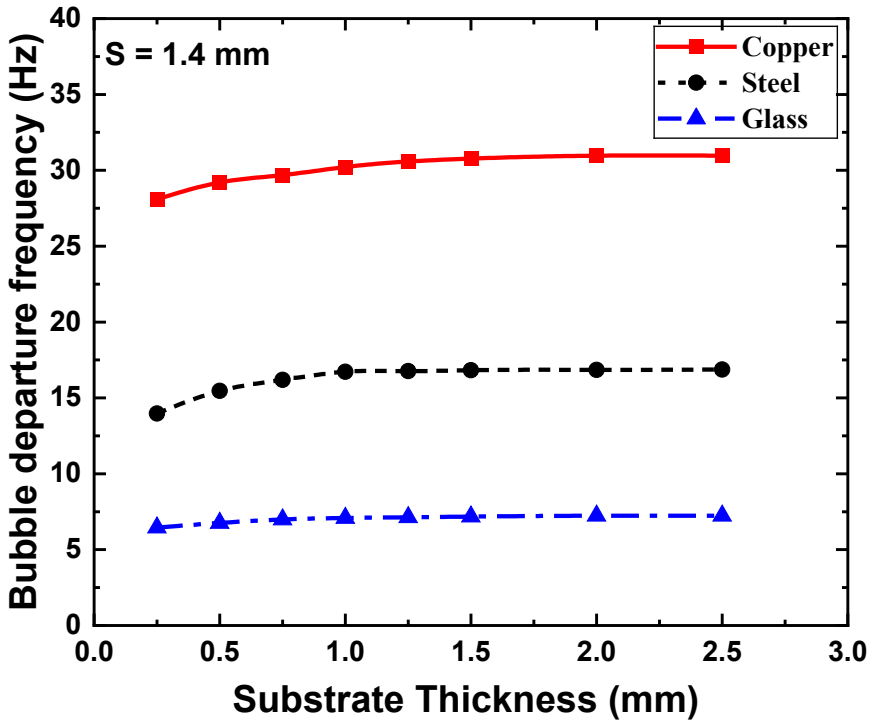

(b)

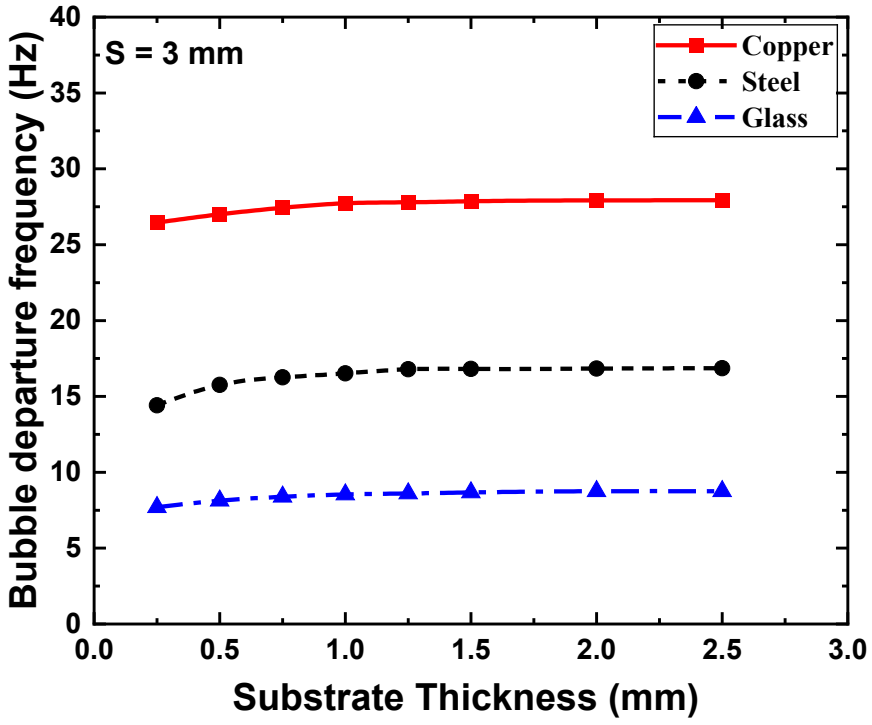

Fig. 4.11: Variation of bubble departure frequency with substrate material and thickness for cavity spacings of (a) S = 1.4 mm and (b) S = 3 mm. $q_{w,in}$ = 1.1 W/cm^2, ΔT_{nuc} = 6 °C, φ = 35°.

4.2.5 Average Vapor Production Rate

The variation of the average vapor production rate over one complete bubble cycle with substrate material and thickness for cavity spacings S = 1.4 mm and S = 3 mm is shown in Fig. 4.12. The average vapor production rate is calculated from the vapor bubble volume at departure and the total cycle time. It is seen in Fig. 4.12 that for all the three substrate materials, the average vapor production rates are higher for cavity spacing S = 3 mm than the corresponding vapor production rates for cavity spacing S = 1.4 mm. This is mainly due to the smaller bubble departure diameter for S = 1.4 mm caused by lateral bubble merger. Further details on the effect of bubble merger on departure diameter and vapor production rate for a given substrate material and thickness is explained in Chapter 3. For a given cavity spacing, the vapor production rate increases with increase in substrate thermal diffusivity mainly due to the associated decrease in waiting time. Additionally, the vapor production rate increases slightly with increase in substrate thickness for a given material and this is again due to the corresponding gradual decrease in waiting time with increasing thickness.

The average vapor production rate for copper is about 260 % greater than that for glass for cases with lateral bubble merger (S = 1.4 mm) and is about 190 % greater than that for glass when there is no bubble merger (S = 3 mm). The average vapor production rate for a given substrate material increases by less than 18 % with increasing substrate thickness over the range of thicknesses investigated in the present study.

(a)

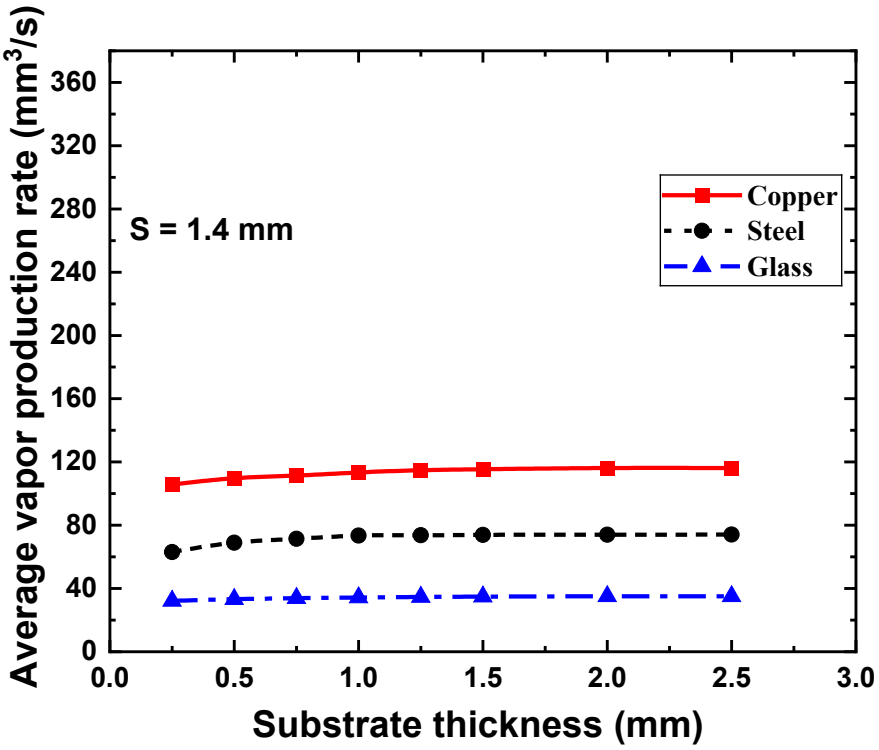

(b)

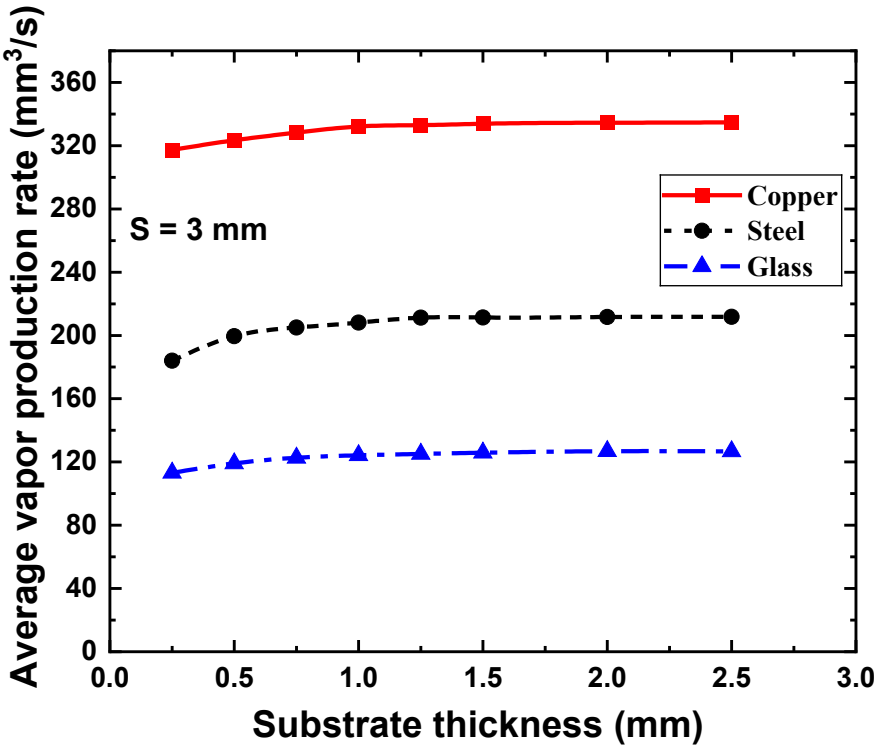

Fig. 4.12 Variation of average vapor production rate over a bubble cycle with substrate material and thickness, for cavity spacings of (a) S = 1.4 mm and (b) S = 3 mm. $q_{w,in}$ = 1.1 W/cm^2, ΔT_{nuc} = 6 °C, φ = 35°.

4.2.6 Heat Transfer Coefficient

The average heat transfer coefficient over one complete bubble cycle is calculated based on the imposed wall heat flux ($q_{w,in}$) and the average wall superheat ($\overline{\Delta T}_w$), as shown below:

$$\bar{h} = \frac{q_{w,in}}{\overline{\Delta T}_w} = \frac{q_{w,in}}{\left(\frac{1}{t_{cycle}\,A}\right)\int_{t=0}^{t=t_{cycle}}\int_{x=0}^{x=X}\int_{z=0}^{z=Z}\left[T_w(x,z,t) - T_{sat}\right]dx\,dz\,dt} \tag{4.1}$$

The cycle duration (t_{cycle}), which is defined as the sum of the growth and waiting periods, represents the repeating unit for each case and it varies from about 32 ms for the copper substrate to about 155 ms for the glass substrate. The area A is 3.5 mm × 3.5 mm, representing the portion of the boiling surface in the computational domain. The average wall superheat ($\overline{\Delta T}_w$) is obtained by averaging the wall superheat over the area of interest (A) of the boiling surface and over one cycle duration (t_{cycle}).

Figure 4.13 shows the variation of the average heat transfer coefficient with substrate material and thickness, for cavity spacings S = 1.4 mm and S = 3 mm. For both cavity spacings, it is observed that the average heat transfer coefficient increases with an increase in substrate thermal diffusivity and with increasing substrate thickness. For the conditions considered in this study, the heat transfer coefficient for the copper substrate is up to 50 % higher than that for the glass substrate. For a given material, the increase in heat transfer coefficient with increasing substrate thickness is less than 8 % for the range of thicknesses considered. As with all the other key parameters discussed in this section, the influence of substrate thermal properties on the average heat transfer coefficient is clearly more significant than that of substrate thickness.

(a)

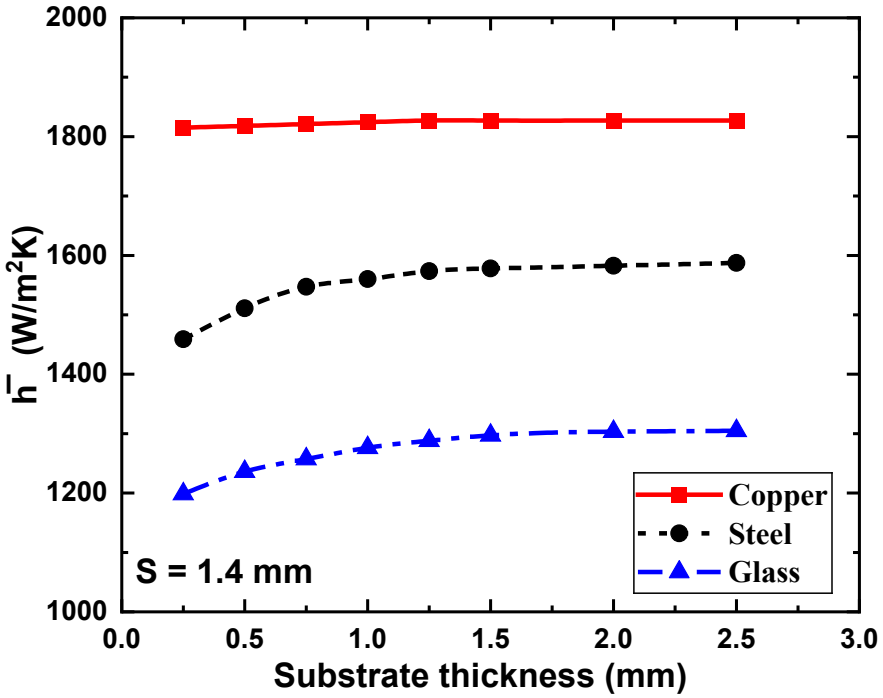

(b)

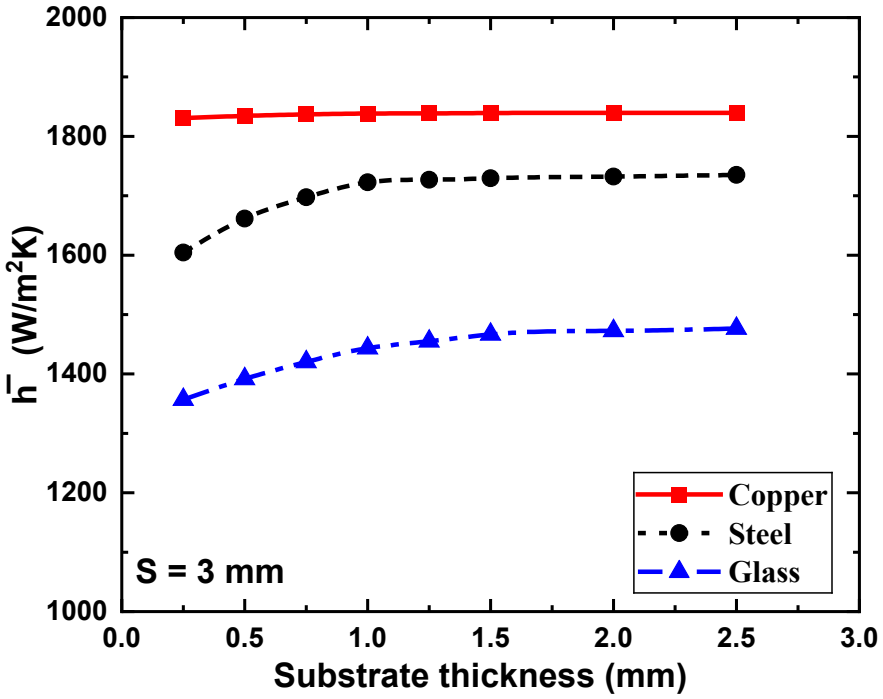

Fig. 4.13: Variation of average heat transfer coefficient over one bubble cycle with substrate material and thickness for cavity spacings (a) S = 1.4 mm and (b) S = 3 mm.

($q_{w,in}$ = 1.1 W/cm^2, ΔT_{nuc} = 6 °C, φ = 35°)

Since the heat flux imposed at the bottom face of the substrate is the same in all the cases in the present study, the average heat transfer coefficient is inversely related to the average wall superheat. Figure 4.14 presents the variation of the average wall superheat ($\overline{\Delta T_w}$) with substrate material and thickness, for the two cavity spacings considered in this study. The average wall superheat decreases with increasing substrate thermal diffusivity and with increasing substrate thickness.

The observed variation in the average wall superheat with substrate material and thickness is in turn explained by the variation in the fraction of total wall energy during one bubble cycle that is utilized for vapor production, shown in Fig. 4.15 for different substrate materials and for cavity spacings S = 1.4 mm and S = 3 mm. It is clearly seen in Fig. 4.15 that the fraction of total wall energy that is used for vapor production in one complete bubble cycle increases as the thermal diffusivity of the substrate increases. It ranges from about 0.08 for a glass substrate to about 0.3 for a copper substrate, with lateral bubble merger (S = 1.4 mm), and from about 0.3 for a glass substrate to about 0.8 for a copper substrate, without lateral bubble merger (S = 3 mm). The difference in the fraction of wall energy utilized for vapor production between the two cavity spacings also explains the smaller average heat transfer coefficient for S = 1.4 mm, for a given substrate material. For both cavity spacings, the fraction of wall energy utilized for vapor production in one bubble cycle decreases by less than 15 % with increasing substrate thickness, for all the substrate materials being compared.

(a)

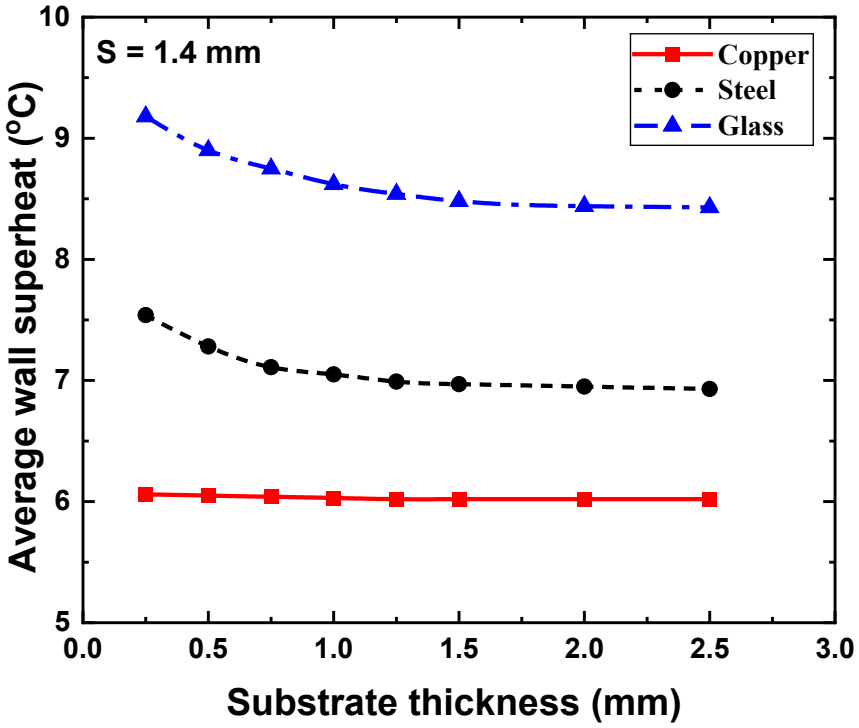

(b)

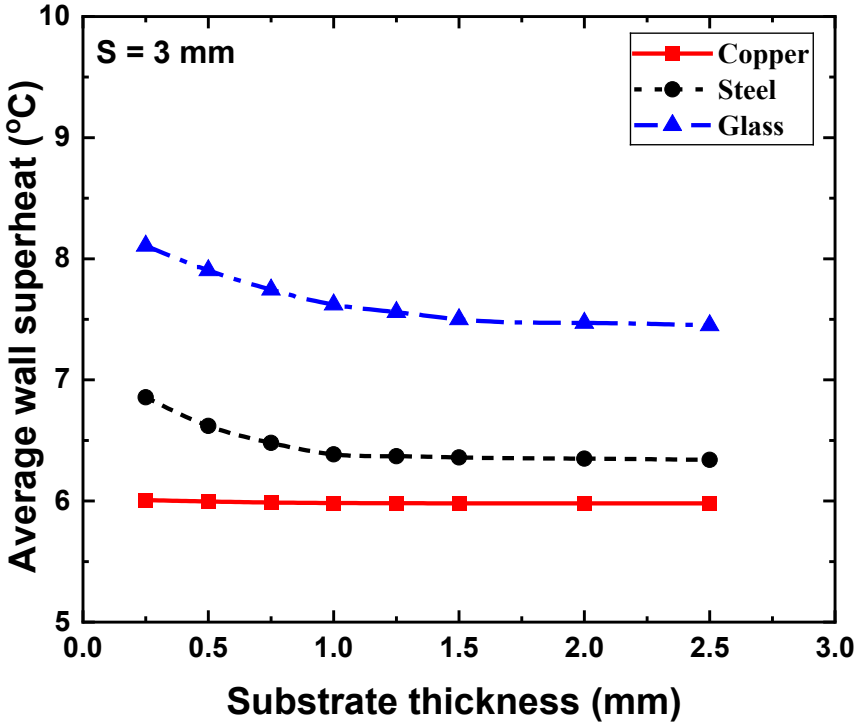

Fig. 4.14: Variation of average wall superheat with substrate material and thickness for cavity spacings (a) S = 1.4 mm and (b) S = 3 mm. ($q_{w,in}$ = 1.1 W/cm^2, ΔT_{nuc} = 6 °C, φ = 35°)

(a)

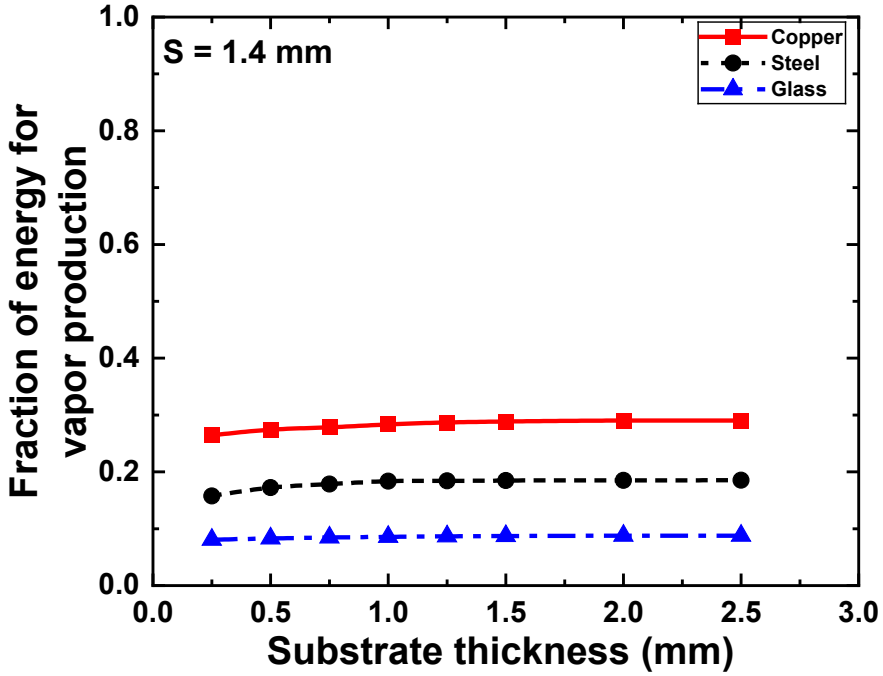

(b)

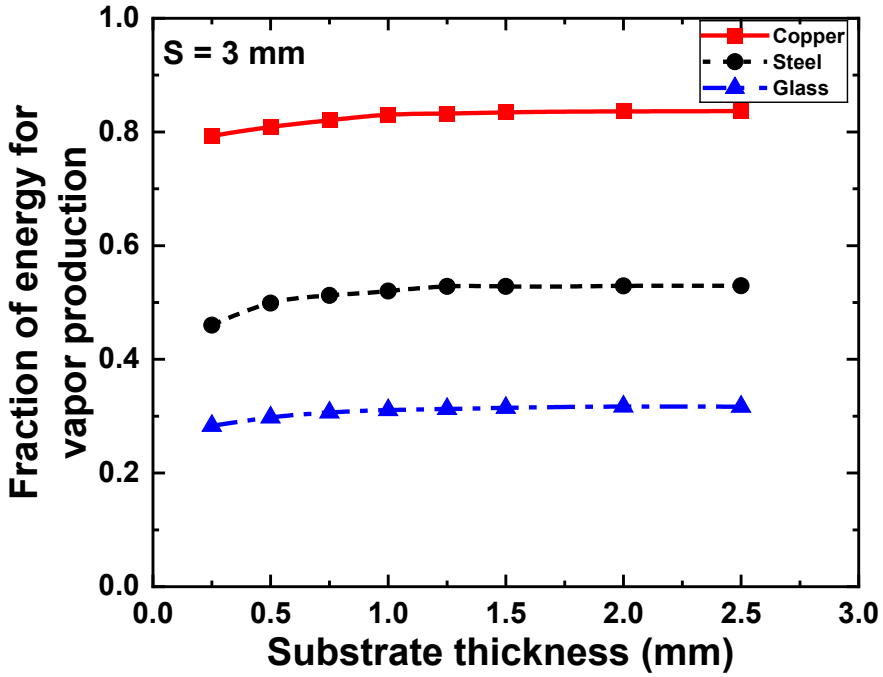

Fig. 4.15: Variation of fraction of total wall energy utilized for vapor production during bubble cycle with substrate material and thickness, for cavity spacings (a) S = 1.4 mm and (b) S = 3 mm.
($q_{w,in}$ = 1.1 W/cm^2, ΔT_{nuc} = 6 °C, φ = 35°)

The numerically predicted trend of increasing heat transfer coefficient with increasing thermal diffusivity obtained in the present study is in line with the overall trends reported in experimental studies that compared pool boiling heat transfer on different materials [31-36]. These experiments, however, involve other surface parameters such as boiling surface structure and wettability, that vary in addition to the substrate material from one test surface to another. In the experiments of Voglar et al. [35], the pool boiling heat transfer coefficient for water on a copper foil coated with a nanostructured copper oxide layer was up to 200 % higher than that on a bare stainless-steel foil. The superhydrophilicity (very small contact angle) of the copper surface may also contribute to the difference in its heat transfer coefficient compared to those for the bare titanium foil and bare stainless-steel foil. Godinez et al. [36] on the other hand found that the boiling curves for saturated pool boiling of water on copper, aluminum and steel substrates were very similar. They noted that at higher heat fluxes the heat transfer coefficient for copper was higher than that for aluminum, which in turn was higher than that for steel, but the differences were still small (~10%) to be of physical significance. The measured static contact angles for the copper, aluminum and steel surfaces were 65°, 12° and 49° respectively.

For a given imposed heat flux and substrate material, such differences in the surface structure and wettability can result in different bubble departure diameters, bubble departure frequencies and density of active nucleation sites, which in turn will have an effect on the heat transfer coefficient. In the present study, all the important boiling surface parameters including the static contact angle, nucleation site density, cavity nucleation superheat were kept unchanged across all the simulations with different substrate materials. The findings of the present study confirm that higher thermal diffusivity of the substrate material tends to increase the heat transfer coefficient, especially at low heat fluxes close to boiling inception.

Chapter 5

Conclusions

Three-dimensional numerical simulations are performed for nucleate pool boiling of saturated water at atmospheric pressure, under a constant imposed heat flux, on a 7 mm × 7 mm portion of a horizontal solid substrate with two adjacent active cavity sites, during boiling inception.

Two parametric simulation studies are done in this work. In the first parametric study, the influence of cavity spacing and lateral bubble merger on bubble dynamics and heat transfer during pool boiling on a 1 mm thick horizontal stainless-steel substrate having two adjacent active nucleation sites with parametrically varied cavity spacing ranging from 1 mm to 3 mm, is investigated.

In the second parametric study, the effects of substrate material thermal properties and substrate thickness on bubble dynamics and heat transfer during pool boiling on copper, stainless-steel and glass substrates, each with 8 different thicknesses ranging from 0.25 mm to 2.5 mm, are analyzed. Two different cavity spacings, 1.4 mm and 3 mm, which represent cases with and without lateral bubble merger respectively, are considered for each substrate.

The transient conduction in the solid substrate is coupled with the fluid-side heat transfer in the simulations. A uniform time-invariant heat flux of 1.1 W/cm^2 imposed at the bottom surface of the substrate, a static contact angle of 35° and a cavity nucleation superheat of 6°C are considered for the entire study. Level set method is used to track the liquid-vapor interface, and finite-difference schemes are used to discretize the governing equations.

5.1 Effect of Cavity Spacing and Lateral Bubble Merger

The main conclusions of the study on the effect of cavity spacing and lateral bubble merger are

- The cavity spacing, and the lateral bubble merger have a marked influence on the waiting time. The waiting time increases as the cavity spacing decreases from 3 mm to 1.8 mm, and decreases with further decrease in spacing from 1.8 mm to 1 mm. The largest value of waiting time, observed for two merging bubbles with a cavity spacing of 1.8 mm, is 450 % greater than the smallest value, for two merging bubbles with 1 mm spacing.
- The bubble departure diameter decreases with decrease in cavity spacing. The bubble departure diameter for 1 mm cavity spacing is 35 % smaller than that for a spacing of 3 mm.
- The bubble growth period increases as the cavity spacing decreases from 3 mm to 2.2 mm. As the cavity spacing decreases further, the bubble growth period decreases. The largest bubble growth period, corresponding to a cavity spacing of 2.2 mm, is 130 % greater than the smallest growth period, observed at 1 mm spacing.
- The bubble departure frequency decreases with decrease in cavity spacing from 3 mm to 1.8 mm, and increases with further decrease in spacing from 1.8 mm to 1 mm. The largest value of bubble departure frequency, for two merging bubbles with a cavity spacing of 1 mm, is 300 % greater than the smallest value, for two merging bubbles with 1.8 mm spacing.
- The average heat transfer coefficient, based on the wall superheat averaged over the boiling surface area in the computational domain (3.5 mm × 3.5 mm with symmetry conditions) and over one bubble cycle, increases with increase in cavity spacing. The average heat transfer coefficient for two non-merging bubbles with cavity spacing 3 mm is 15 % higher than that for two laterally merging bubbles with cavity spacing 1 mm.

5.2 Effect of Substrate Thermal Properties and Thickness

The main conclusions of the study on the effect of substrate thermal properties and thickness are

- The substrate thermal properties are found to have a stronger influence on bubble dynamics and heat transfer during nucleate pool boiling as compared to the substrate thickness.
- Lateral bubble merger does not alter the dependence of bubble dynamics and heat transfer on substrate thermal properties and thickness, except for the bubble growth period.
- The waiting time decreases with increasing substrate thermal diffusivity, and with increasing substrate thickness for a given substrate material.
- The bubble departure diameter decreases with increasing thermal diffusivity, and with increasing substrate thickness for a given material.
- The bubble growth period, for cases without lateral bubble merger, increases with increase in substrate thermal diffusivity. For cases with lateral bubble merger, however, the bubble growth period decreases with increase in substrate thermal diffusivity. For a given substrate material, the bubble growth period increases with increasing substrate thickness, with and without bubble merger.
- The bubble departure frequency increases with increase in substrate thermal diffusivity, and with increase in substrate thickness for a given substrate material.
- The average heat transfer coefficient, based on the wall superheat averaged over the boiling surface area in the computational domain (3.5 mm × 3.5 mm with symmetry conditions) and over one bubble cycle, increases with increase in substrate thermal diffusivity, and with increase in substrate thickness. The average heat transfer coefficient for the copper substrate is up to 50 % higher than that for the glass substrate. The heat transfer coefficient increases by less than 8 % with increasing substrate thickness for a given material.

Bibliography

[1] Wang, C. H., & Dhir, V. K. (1993). On the Gas Entrapment and Nucleation Site Density During Pool Boiling of Saturated Water. *Journal of Heat Transfer*, 115(3), 659-669.

[2] Hsu, Y. Y. (1962). On the Size Range of Active Nucleation Cavities on a Heating Surface. *Journal of Heat Transfer*, 84(3), 207–213.

[3] Basu, N., Warrier, G. R., & Dhir, V. K. (2002). Onset of Nucleate Boiling and Active Nucleation Site Density During Subcooled Flow Boiling. *ASME J. Heat Transfer*, 124(4), 717–728.

[4] Mikic, B. B., Rohsenow, W. M., & Griffith, P. (1970). On bubble growth rates. *International Journal of Heat and Mass Transfer*, 13(4), 657–666.

[5] Moore, F. D. and Mesler, R. B. (1961). The measurement of rapid surface temperature fluctuations during nucleate boiling of water. *AIChE Journal*, 7(4), 620-624.

[6] Cooper, M. G. and Lloyd, A. J. P. (1969). The microlayer in nucleate pool boiling. *International Journal of Heat and Mass Transfer*, 12(8), 895-913.

[7] Golobic, I., Petkovsek, J., Baselj, M., Papez, A., & Kenning, D. B. R. (2009). Experimental determination of transient wall temperature distributions close to growing vapor bubbles. *Heat and Mass Transfer/Waerme-Und Stoffuebertragung*, *45*(7), 857–866.

[8] Wagner, E., & Stephan, P. (2009). High-resolution measurements at nucleate boiling of pure FC-84 and FC-3284 and its binary mixtures. *Journal of Heat Transfer*, *131*(12), 1–12.

[9] Moghaddam, S., and Kiger, K. (2009). Physical Mechanisms of Heat Transfer during Single Bubble Nucleate Boiling of FC-72 under Saturation Conditions-I. Experimental Investigation. *International Journal of Heat and Mass Transfer*, 52(5–6), 1284–94.

[10] Narayan, S. and Srivastava, A. (2021). On the Identification and Mapping of Three Distinct Stages of Single Vapor Bubble Growth with the Corresponding Microlayer Dynamics. *International Journal of Multiphase Flow*, 142 (September).

[11] Cooper, M. G. (1969). The microlayer and bubble growth in nucleate pool boiling. *International Journal of Heat and Mass Transfer*, *12*(8), 915–933.

[12] Cole, R., & Shulman, H. L. (1966). Bubble growth rates at high Jakob numbers. *International Journal of Heat and Mass Transfer*, *9*(12), 1377–1390.

[13] Fritz, W. (1935). Maximum Volume of Vapor Bubbles. *Physic. Zeitschz.*, *36*, 379–384.

[14] Cole, R. (1967). Bubble frequencies and departure volumes at subatmospheric pressures. *AIChE Journal*, *13*(4), 779–783.

[15] Stralen, van, S. J. D., & Zijl, W. (1978). Fundamental developments in bubble dynamics. In: *Proceedings of the 6th International heat transfer conference, Toronto,* 429-447.

[16] Kocamustafaogullari, G. (1983). Pressure dependence of bubble departure diameter for water. *International Communications in Heat and Mass Transfer*, *10*(6), 501–509.

[17] Zuber, N. (1961). The dynamics of vapor bubbles in nonuniform temperature fields. *International Journal of Heat and Mass Transfer*, *2*(1), 83–98.

[18] Chi-Yeh, H., & Griffith, P. (1965). The mechanism of heat transfer in nucleate pool boiling—Part I: Bubble initiaton, growth and departure. *International Journal of Heat and Mass Transfer*, *8*(6), 887–904.

[19] Jakob, M. (1949) Heat Transfer, Chapter 29,1. Wiley, New York.

[20] Zuber, N. (1963). Nucleate boiling. The region of isolated bubbles and the similarity with natural convection. *International Journal of Heat and Mass Transfer*, *6*(1), 53–78.

[21] Peebles, F. N. (1953). Studies on the motion of gas bubbles in liquid. *Chem. Eng. Prog.*, *49*(2), 88-97.

[22] Gaertner, R F, & Westwater, J W (1959). Population of active sites in nucleate boiling heat transfer. *Chem. Eng. Progr*., Vol: 56: Symposium Ser. No. 30.

[23] Zhang, L., & Shoji, M. (2003). Nucleation site interaction in pool boiling on the artificial surface. *International Journal of Heat and Mass Transfer*, *46*(3), 513–522.

[24] Chatpun, S., Watanabe, M., & Shoji, M. (2004). Experimental study on characteristics of nucleate pool boiling by the effects of cavity arrangement. *Experimental Thermal and Fluid Science*, *29*(1), 33–40.

[25] Jiang, YY, Osada, H, Inagaki, M, & Horinouchi, N. (2010) Wall Thermal Conductivity Effects on Nucleation Site Interaction During Boiling: An Experimental Study. *Proceedings of the 2010 14th International Heat Transfer Conference*, *Volume 1*. ASME. Washington, DC, USA. 637-646.

[26] Mukherjee, A., & Dhir, V. K. (2004). Study of lateral merger of vapor bubbles during nucleate pool boiling. *Journal of Heat Transfer*, *126*(6), 1023–1039.

[27] Son, G., Dhir, V. K., and Ramanujapu, N. (1999). Dynamics and Heat Transfer Associated with a Single Bubble During Nucleate Boiling on a Horizontal Surface. *ASME. J. Heat Transfer*. 121(3). 623–631.

[28] Lay, J. H., & Dhir, V. K. (1995). Shape of a vapor stem during nucleate boiling of saturated liquids. *Journal of Heat Transfer*, 117(2), 394-401.

[29] Aparajith, H. S., Dhir, V. K., & Son, G. (2006). Numerical simulation of the dynamics of multiple bubble merger during pool boiling under reduced gravity. *Multiphase Science and Technology*, *18*(3), 277–304.

[30] Magrini, U., & Nannei, E. (1975). On the Influence of the Thickness and Thermal Properties of Heating Walls on the Heat Transfer Coefficients in Nucleate Pool Boiling. *Journal of Heat Transfer*, *97*(2), 173–178.

[31] Jabardo, J. M. S., Ribatski, G., & Stelute, E. (2009). Roughness and surface material effects on nucleate boiling heat transfer from cylindrical surfaces to refrigerants R-134a and R-123. *Experimental Thermal and Fluid Science*, *33*(4), 579–590.

[32] Seo, G. H., Jeun, G., & Kim, S. J. (2015). Pool boiling heat transfer characteristics of zircaloy and SiC claddings in deionized water at low pressure. *Experimental Thermal and Fluid Science*, *64*, 42–53.

[33] Hosseini, R., Gholaminejad, A., & Nabil, M. (2011). Concerning The Effect of Surface Material on Nucleate Boiling Heat Transfer of R-113. *Journal of Electronics Cooling and Thermal Control*, *1*(2), 22–27.

[34] Bombardieri, C., & Manfletti, C. (2016). Influence of wall material on nucleate pool boiling of liquid nitrogen. *International Journal of Heat and Mass Transfer*, *94*, 1–8.

[35] Voglar, J., Zupančič, M., Peperko, A., Birbarah, P., Miljkovic, N., & Golobič, I. (2019). Analysis of heater-wall temperature distributions during the saturated pool boiling of water. *Experimental Thermal and Fluid Science*, *102*, 205–214.

[36] Godinez, J. C., Cho, H., Fadda, D., Lee, J., Park, S. J., & You, S. M. (2021). Effects of materials and microstructures on pool boiling of saturated water from metallic surfaces. *International Journal of Thermal Sciences*, *165*.

[37] Kapitz, M., Becker, A., & Wiesche, S. A. Der. (2014). Influence of thermophysical wall properties during pool boiling on large diamond and SiC heaters. *Heat Transfer Engineering*, *35*(5), 472–481.

[38] Mann, M., Stephan, K., & Stephan, P. (2000). Influence of heat conduction in the wall on nucleate boiling heat transfer. *International Journal of Heat and Mass Transfer*, *43*(12), 2193–2203.

[39] Stephan, P., & Hammer, J. (1994). A new model for nucleate boiling heat transfer. *Heat and Mass Transfer*, *30*(2), 119–125.

[40] Aktinol, E., & Dhir, V. K. (2012). Numerical simulation of nucleate boiling phenomenon coupled with thermal response of the solid. *Microgravity Science and Technology*, *24*(4), 255–265.

[41] Zhang, L., Li, Z. D., Li, K., Li, H. X., & Zhao, J. F. (2015). Influence of heater thermal capacity on bubble dynamics and heat transfer in nucleate pool boiling. *Applied Thermal Engineering*, *88*, 118–126.

[42] Wayner, P. C., Kao, Y. K., & LaCroix, L. V. (1976). The interline heat-transfer coefficient of an evaporating wetting film. *International Journal of Heat and Mass Transfer*, *19*(5), 487–492.

[43] Kays, W. M., and Crawford, M. E. (1980). *Convective Heat and Mass Transfer*, McGraw–Hill, New York, p. 328.

[44] Douglas, J., & Gunn, J. E. (1964). A general formulation of alternating direction methods. Numerische Mathematik, 6(1), 428-453.